UNIVERSITÉ DE SHERBROOKE
Faculté de génie
Département de génie mécanique

Développement d'un tourbillon de bout d'aile sous l'effet de l'intensité de turbulence de l'écoulement libre

Thèse de doctorat
Specialité: génie mécanique

Kamal Ben Miloud

Sherbrooke (Québec) Canada

Juin 2020

JURY MEMBERS

Hachimi FELLOUAH
Supervisor

Mohsen FERCHICHI
Co-supervisor

Ruben PEREZ (RMC)
Examiner

Ali BENMEDDOUR (CNRC)
Examiner

Sébastien LANGLOIS (UdS)
Examiner

RÉSUMÉ

L'étude des tourbillons de bout d'aile est d'une importance majeure comme elle concerne plusieurs secteurs industriels. La génération d'un tourbillon au bout d'aile d'un avion est une conséquence directe de la portance, la présence de cette structure d'écoulement dans les environs d'un aéroport perturbe le traffic aérien comme elle peut interagir avec d'autres avions en vol, ce qui compromettrait la sécurité aérienne. Plusieurs études ont été élaborées sur un plan scientifique afin d'apporter des connaissances approfondies sur la dynamique des tourbillons de bout d'aile. Des investigations numériques et expérimentales ont permis de comprendre la formation et l'évolution d'un tourbillon en aval du bord de fuite d'une aile. Cependant, les connaissances sur ces structures tridimensionnelles restent limitées, surtout concernant l'aspect de leur évolution spatio-temporel. En effet, plusieurs études scientifiques se sont concentrés sur des conditions d'écoulement spécifiques et ayant utilisé des techniques de mesures ponctuelles, comme le fil chaud. Il a été démontré que le tourbillon peut dissiper s'il est immergé dans un écoulement turbulent, sa vitesse circomférentielle décroit et son rayon augmente en aval de l'aile. Dans la présente étude, la vélocimetrie par imagerie de particules stéréoscopique a été utilisée pour comprendre la formation et l'évolution d'un tourbillon de bout d'aile NACA 0012 dans un écoulement de grille. La surface portante est disposée à un angle d'attaque de 5.6° ou l'écoulement est supposé rester attaché, et soumise à un écoulement avec deux nombres de Reynolds, 2×10^5 et 3×10^5, ainsi que trois régimes de turbulence de l'écoulement libre (FST), à savoir 0.5% (soufflerie sans grille), 3% (position GP1) et 6% (position GP2). Des mesures sur le champ de vitesse du sillage sont effectuées en quatre positions en aval de l'aile, à savoir x/c=1.25, 3.25, 6.25 et 7.75 pour les deux nombres de Reynolds et les trois niveaux de turbulence utilisés. Dans une première partie de l'étude, la dynamique du tourbillon est mise en évidence en analysant le champ de vitesse du sillage et les caractéristiques du tourbillon. Les contours de vitesse et de vorticité ont permis de distinguer la structure du coeur du tourbillon qui s'assimile à un type "wake-like", décrivant ainsi un déficit de vitesse qui décroit longitudinalement et qui décroit avec l'augmentation du niveau de turbulence, FST. Une investigation sur le mouvement de l'axe horizontal du tourbillon a également été menée. La détermination du centre instantanée du tourbillon a permis de déterminer les amplitudes de l'érrance du tourbillon qui augmente avec l'augmentation de FST. L'analyse de l'énergie cinétique turbulente a révélé la présence de turbulence artificielle, qui a été réduite en appliquant une correction sur les champs de vitesse. Dans une deuxième partie de l'étude, une analyse détaillée sur l'érrance est menée en se basant sur la technique de décomposition orthogornale propre (POD). Une augmentation du mouvement d'érrance a été caractérisée par l'augmentation de l'énergie associée au modes. Pour le cas GP2, le dipole avait la tendence à se dissiper en un seul mode, correspondant ainsi à un tourbillon trés dissipé. De plus, une évaluation des termes de l'équation de transport de l'enstrophie a été menée en dernière partie dans le plan x/c = 1.25. Il a été constaté que l'aumentation de FST favorise l'amplification des termes de cisaillement et d'enstrophie.

Mots-clés : Tourbillon de bout d'aile, Soufflerie, Turbulence, Mesures, POD

ABSTRACT

The study of wing-tip vortices is of major importance as it concerns several industrial sectors. Wing-tip vortices generation is a pure consequence of lift, the presence of these flow structures in the vicinity of airport runways affect the air traffic as it could interfere with the flight path of other aircraft, which could compromise their safety. Several scientific studies have been performed to provide in-depth knowledge of wing-tip vortices dynamics. Numerical and experimental investigations have brought new key data to understand the formation and evolution of a vortex downstream of the trailing edge of a wing. However, these three-dimensional structures knowledge remains limited, especially under certain flow and boundary conditions. Indeed, several scientific studies have focused on using singe point measurements such as hot wire. It has been shown that the vortex can dissipate if immersed in a turbulent flow, its circumferential velocity decreases and its radius increases downstream of the wing. In the present study, an experimental investigation was used to understand the formation and evolution of a NACA 0012 wing-tip vortex inside a wind tunnel. The wing is disposed at an angle of attack of 5.6° where the flow is supposed to remain attached, and subjected to a flow with two Reynolds numbers,2×10^5 and 3×10^5, and three free stream turbulence (FST) intensities, FST=0.5% (no-grid), FST=3% (GP1 position) and FST=6% (GP2 position). The turbulent flow is generated using a wooden grid, for which the integral length scale was estimated. Wake velocity measurements are made at four positions downstream of the wing, namely at x/c=1.25, 3.25, 6.25 and 7.75 for both Reynolds numbers and the three levels of turbulence used. In a first part of the study, the dynamics of the vortex are highlighted by analyzing the velocity field and the characteristics of the vortex. The contours of velocity and vorticity have made it possible to distinguish the structure of the vortex core and the spiral wake, describing a "wake-like" profile. It demonstrated an axial velocity deficit that decreased with increased downstream distance, and decreased with the FST level. The determination of the instantaneous vortex center allowed to estimate the meandering amplitudes which increased with increased FST. The turbulent kinetic energy analysis revealed the presence of artificial turbulence, which was reduced by applying a correction to the velocity field. In a second part of the study, a detailed analysis on the vortex meandering was conducted using the proper orthogonal decomposition (POD). Coherent structures were determined at the positions x/c = 1.75 and x/c = 5.75 with a Reynolds number of $Re_1 = 2\times10^5$. An increased meandering motion due FST increase showed an increase of the energy content of the dominant helical mode. FST promoted the increase of the shear and enstrophy terms.

Keywords: Wing-tip Vortex, Wind-Tunnel, Turbulence, Measurements, POD

ACKNOWLEDGEMENTS

Je tiens à adresser mes remerciements à mon directeur de thèse, Professeur Hachimi Fellouah, pour sa disponibilité, son engagement et sa patience tout au long de ma formation.

Je tiens à remercier également mon co-directeur de thèse, Professeur Mohsen Ferchichi, pour ses enseignements, sa disponibilité et son encadrement.

Enfin, que tous ceux qui ont contribué de près ou de loin à faciliter cette étude trouvent ici le témoignage de ma sincère gratitude et vive reconnaissance.

Je dédie ce travail à mes chers parents, ma chère soeur, mes chers frères.

A mes vrais amis.

A ma trés chère Tinhinane.

TABLE OF CONTENTS

LIST OF FIGURES

LIST OF TABLES

LIST OF SYMBOLS

Symbole	Définition
AR	Aspect ratio
A	Coefficient
b	Wing span, m
c	Corde, m
C	advection of enstrophy by mean flow
f	Frequency, Hz
Re	Reynolds number
L	Lenght scale
M	Mesh size, m
n	Exponent
(x, y, z)	Streamwise, spanwise and transverse directions, m
u	Instantaneous Streamwise velocity
v	Instantaneous Spanwise velocity
w	Instantaneous Transverse velocity
U	Average Streamwise velocity
V	Average Spanwise velocity
W	Average Transverse velocity
T	Transport of enstrophy by turbulent vorticity-velocity interactions
P	Turbulence production term
$\bar{v}_\theta$	Average circumferential velocity rad/s
k, TKE	Turbulent Kinetic Energy, m^2/s^2
θ	Angular polar coordinate
r	radius
R	Reynolds Stress
ξ	Streamwise Vorticity, m/s^2
Γ_1	Circulation
ν	Viscous diffusion of enstrophy
ϵ	Viscous dissipation of enstrophy
η	Normalized radius
σ	Meandering amplitude, m
λ	Energy contribution for mode, m^2/s^2
ϕ	Scalar mode

LIST OF ACRONYMS

Acronyme	**Definition**
AoA	Angle of Attack
FST	Free Stream Turbulence
ICAO	International Civil Aviation Organization
MTOW	Minimum Take-Off Weight

CHAPTER 1

INTRODUCTION

1.1 Background and motivation

The aerospace industry is continuously being challenged with new technologies and limits, to provide an optimized and more safe transport mean. The Research in this field is unquestionably one of the most advanced in the world. Airlines and aircraft manufacturers are investing billions of dollars to push this industry to its limits. One of the major challenges is to find solutions which improve flight performance and reduce fuel consumption, directly related to the aerodynamics of the aircraft. A body with optimized aerodynamics minimizes drag forces and therefore reduces the amount of fuel consumed.

Research and development in aerodynamics has moved to an advanced level in almost a century. After the first wind tunnel experiments carried out by Reissnet & Junkers in 1909, the use of subsonic flows was developed in the early 1930ś by Weiselsberger, who made the first analysis of the distribution of the lift as a function of the wingspan [1]. Subsequent improvements led to more accurate measurements of the pressure distribution and forces applied to the subsonic flow profile. The introduction of numerical tool made it possible to fill the gaps encountered during the experimental tests, notably the understanding of the effects of a wake and the characteristics of a vortex for example [2–9]. The continuous improvement of these experimental investigation techniques such as the introduction of Laser Anemometry techniques : Particle Image Velicimetry (PIV) or the Laser Doppler Velocimetry (LDV) has enlightened many questions related to flows dynamic instabilities [10]. However, the use of these usual techniques is not always affordable because of financial constraints and congestion in particular.

The presence of a vortex is a sign of one or more disturbances in the flow. The latter can manifest itself according to several parameters, and in different regions of the aircraft fuselage. The types of vortices are very different, not only in their size, but also in the phenomenon they describe. Wing-tip vorticies are generated as a consequence of lift generation, these 3D structures are known as induced drag holds as high as 40% of the aircraft total drag in cruise [11]. The presence of these structures in the vicinity of runways can impose loss of altitude to nearby flying aircraft due to the upwash and downwash streams (Figure 1.1), additionally, structural damage could also occure which

consist a serious hazard. Few options were provided by the aviation authorities such as the International Civil Aviation Organization (ICAO) which imposed a separation distance between aircraft with similar flight paths or 2 minutes delay, to facilitate the dissipation of the trailing vortices and decrease the aircraft encounters [12, 13]. For instance, a medium category aircraft (Boeing 737/Airbus A320) landing behind a super heavy aircraft (Airbus A380) would require 7 Miles longitudinal separation distance [11].

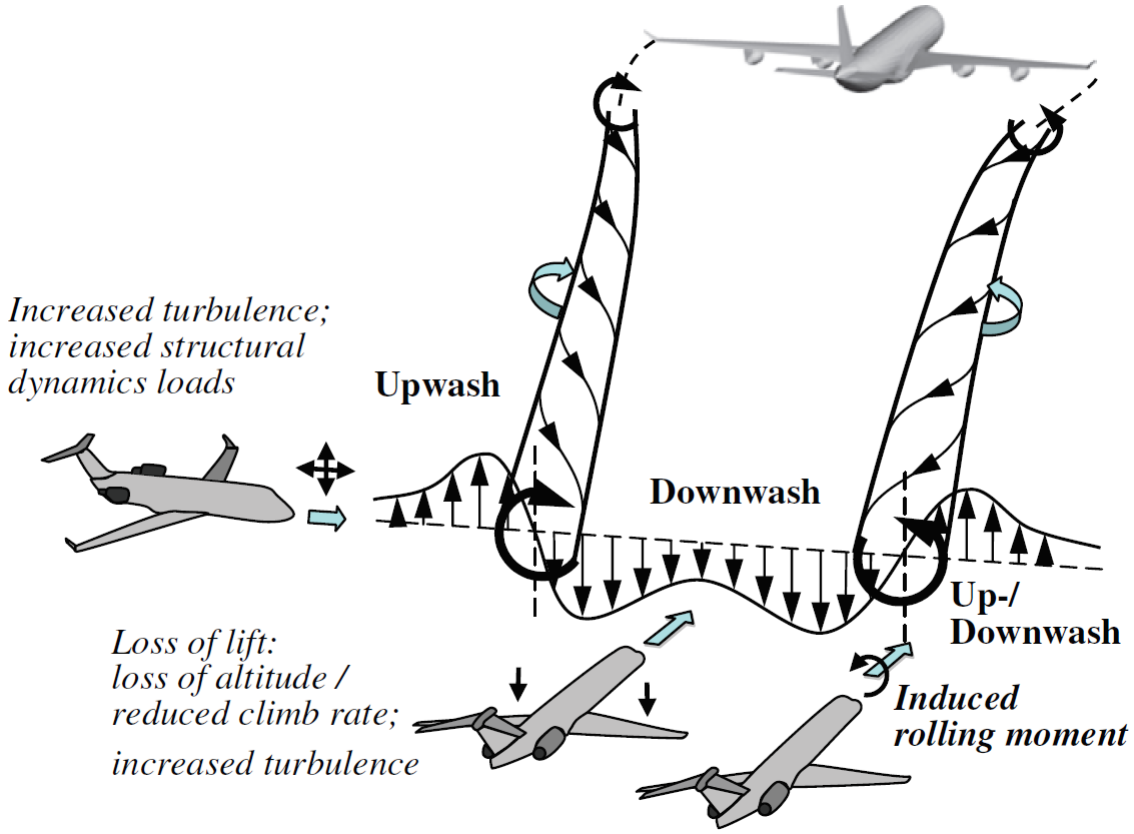

Figure 1.1 Vortex encounters [14]

Depending on the flight conditions, these trailing vortices may dissipate or increase in size if they are subject to air velocity variation. Some of the controlling parameters for wing-tip vortices are AOA (Angle of Attack), Reynolds number (Re) or also the free stream turbulence (FST). A single or a combination of these parameters is a detrimental factor which affects the aerodynamic efficiency during flight. While lift is generated, the air leaks and rolls from the pressure side of the wing-tip toward the suction side setting up a helical flow downstream the wing as the aircraft is flying forward. Being continuously fed by vorticity injection from the boundary layer near the wing-tip, the vortex decays as it evolves downstream and increases in size [15]. Viscous and turbulent diffusion forces bring a considerable contribution on the decay mechanism with increased downstream distances.

Furthermore, the inner vortex core is a viscous body in rotation where the viscous forces are dominant. In the outer region of the vortex core, the circumferential velocity reaches a peak while the shear stresses are important. Extensive studies have reproduced wing-tip vortices in wind tunnel experiments, velocity field data could be explored from the vortex in the wake region. In fact, observation on the vortex behavior inside a wind tunnel suggested that it is subject to some instantaneous variation of its axis, which is commonly known as vortex meandering.

1.2 Objectives and approach

The effect of free stream turbulence (FST) on the formation and development of a wing-tip vortex has been studied in only few papers, where single point of measurements such as hot-wire were mainly used. Few other studies treated the aspect of turbulence interaction with the vortex velocity field using optical flow measurements which brought new evidences on the vortex meandering mechanisms. The evolution of wing-tip vortices in a flow remains a subject of interesting research due to its sensitivity to geometric and flow initial/boundary conditions. There seem to be little effect of Reynolds number on the vortex while it evolves under the effect of FST. This will be addressed in this thesis. The key ideas are to bring additional answers through this experimental work. The main objectives of this study can be summarized into the following:

- Perform velocity field measurements in downstream of the wing-tip with Stereoscopic Particle Image Velocimetry (SPIV)
- Document the effect of Free Stream Turbulence and Reynolds number on the early formation of a wing-tip vortex in the near and mid wake regions.
- Quantify the contributions of Free Stream Turbulence and Reynolds number on the vorticity equation terms and analyze the meandering motion on the diffusion and decay of the vortex.
- Provide further insight into the phenomenon of vortex meandering using POD decomposition

1.3 Contribution of the study

As the vortex is generated behind the trailing edge of the wing, it decays after a certain time and distance. It was shown in previous studies that FST greatly affects a wing-tip vortex formation and development, and increasing Re strengthens the vortex. While current solutions do not prevent the vortex formation, there are several technologies that could benefit from this study. Since we are presenting two competing effects of FST

and Re on the vortex, the behavior of the vortex under these two parameters is poorly understood and was never discussed by the scientific community. This provides a high scientific value of the presented results as valuable data could be explored from our study if future technologies use turbulence to reduce the vortex strength. As a matter of fact, a recent experimental study performed by DLR in Germany used runway "dissipators" where vertical plates are placed at the edge of runways to accelerate the dissipation rate of the vortex.

1.4 Thesis Outline

The structure of this thesis, Wing-tip Vortex Development under the Effect of Free Stream Turbulence, is displayed in five main chapters, detailed as follows:

- Chapter 1 : Introduction

  In this chapter, a background overview is presented followed by an introduction to the subject with key citations of the objectives, the motivation and the concept of the study.

- Chapter 2 : State of the art - Literature review

  The objective of this chapter is to show the contribution of different studies to the field of vortex development with particular interest in formation, roll up and development processes and the characterization of these structures.

- Chapter 3 : Interaction between Free stream Turbulence and a Wing-tip vortex

  The chapter 3 includes the submitted paper in a scientific journal, where vortex velocity field and characteristics were determined to evaluate the formation, roll up and development of the vortex downstream the wing. The linearity due to the coupled effect of FST and Re is also discussed.

- Chapter 4 : POD Analysis of a Wing-tip Vortex meandering in a Grid Generated Turbulent Flow

  The chapter 4 includes a second scientific paper which discusses the vortex meandering under a grid generated turbulence. Proper Orthogonal Decomposition is used to assess the coherent structures, with an estimation of the mean flow vorticity equation terms.

- Chapter 5 : Conclusions

  This chapter summarizes the thesis and provides recommendations for future works.

CHAPTER 2

STATE OF THE ART

The literature review of wing-tip vortices is being very diverse, the current chapter has been divided into three sections:

- Wing-Tip Vortices
- Wing-Tip Vortex formation, roll up and development
- Vortex characterization

2.1 Wing-Tip Vortices

Wing-tip vortices are a common phenomenon which are generated behind lifting surfaces. Because of their predominance and negative effects, they present a very important topic in numerous engineering applications. Wing-tip vortices are formed behind aircraft wings as they generate lift, due to the pressure difference between the suction and pressure surfaces. These 3D structucres evolves in space where they can last for few minutes and can even reach a length of 30 km for large aircraft [15](Figure 2.1). They become dominant and complex in the close distance behind the wing, especially during high-lift configurations such as take-off or landing. The presence of strong vortices behind the wing trailing edge can in fact encounter nearby flying aircraft and compromise a safe airspace management. Loss of control could occur to the encountered aircraft which is dangerous at low altitude [16]. A common practice used in air traffic management is to restrict a separation distance between two aircraft in the same flight path close to runways, which depends on the Maximum Take-Off Weight (MTOW). This is obviously a huge inconvenience for some airports that accommodate aircraft of different sizes. Experimental and theoretical models were also developed, various patents related to wing-tip vortices reduction were presented in the paper of [17]. Other options which decrease the vortices strength consist on implementing added-on devices on the aircraft body, or the wings which modifies the wing geometry, decreasing then the wrapping motion between the wing two surfaces. Winglets are commmonly used for that purpose for instance, which were refered in several studies [15, 18, 19]. Furthermore, recent applications went to decrease the harazrd of wing-tip vortices by applying advanced navigation technologies, in order to decrease the approach phase flight pattern, and bring the aircraft from cruise altitude to the runway for landing [20, 21]. Other researchers favored the use of synthetic jets on the wing-tip

to decrease the vortex strength, like Dghim et al. [22–25]. An actuation diaphragm was used at the rectangular wing-tip through a cavity embedded inside the wing. The authors observed that high momentum coefficient, $C_\mu = 0.04$, and the frequency actuation contributed on the vortex decay. More particularly, they observed a vortex stretching into an ellipsoidal shape causing a decrease in the in the axial velocity deficit and a decrease in the peak circumferential velocity. A noticeable reduction of the normal axial vorticity was also reported by the authors. Under such configuration, it appeared that the synthetic jet contributed on the diffusion of the vortex core, this was reported by the authors as they concluded a vortex radius increase downstream the wing-tip, translated by a turbulent mixing which was triggered by the turbulence injection of the synthetic jet actuation. Over a flying commercial aircraft wing in cruise, several dominant vorticies could appear : wing-tip vortex (WTP), outboard flap vortex (OFV), outer and inner engine nacelle vorticies (ONV and INV), the wing-fuselage vortex (WFV) and the horizontal tailplane vortex (HTV) as per Figure 2.2 [15]. Despite the fact that these vortices depict different behaviors, they commonly describe high velocity fluctuations. In the near field (Figure 2.3), which extends from the wing trailing edge to few chords behind the aircraft, vortex complete roll-up occurs where secondary structures merge with other trailing vorticies [15, 26–28]. An extended near wake is possible if the roll up phase is not completed. In the mid field/far field, the voritices pair induces a descent motion [28] which interacts with the ground surface at a certain velocity. At last, the vortex decays in a region where effect of viscous forces are dominant [29, 30].

2.2 Wing-Tip Vortex formation, roll up and Development

At the aircraft wing-tip, the vortex formation occurs as a results of the vorticity formed by velocity shear [31], whereas the initial lift generation is strongly dependent on the wing effective incident angle [32]. Many parameters could affect the vortex formation, namely geometric or flow conditions parameters. The geometric parameters concern the tip geometry, wing profile, angle of attack or chord length. Flow conditions, which play a major role compared to the geometric parameters, are mainly associated with the environement where the vortex is formed. They are associated with Reynolds number, turbulence intensity or buoyancy. Typically, during the first moments of vortex formation, pressure on the axis of the vortex core gradually decreases with increasing circumferential velocity [33]. In a turbulent environement such as flight [34], a shear layer is generated from the spanwise flow.

Figure 2.1 Wake behind aircraft [35]

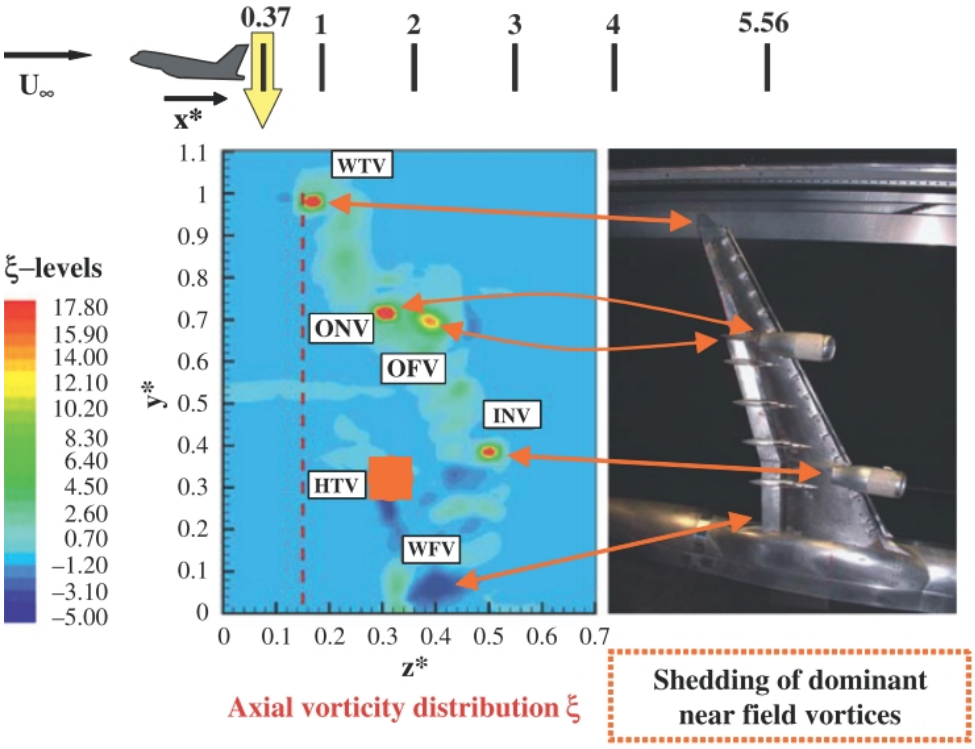

Figure 2.2 Wing Vortices [15]

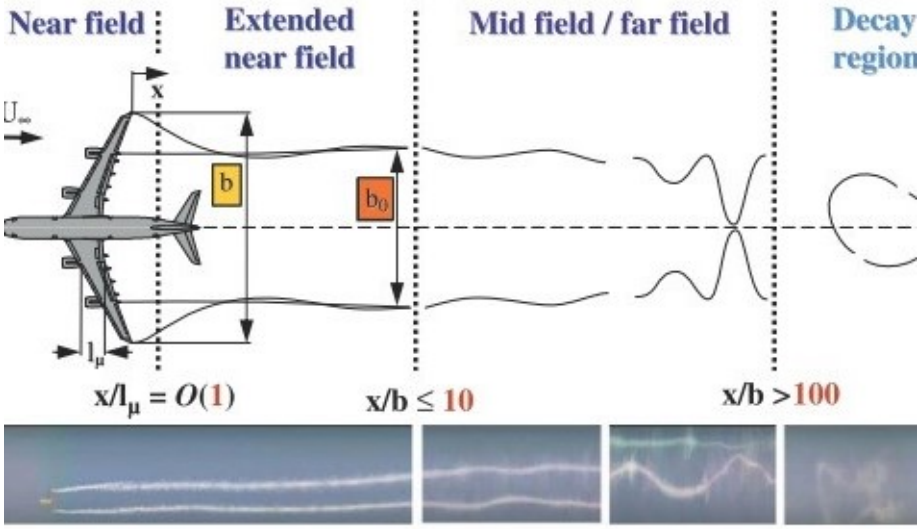

(a)

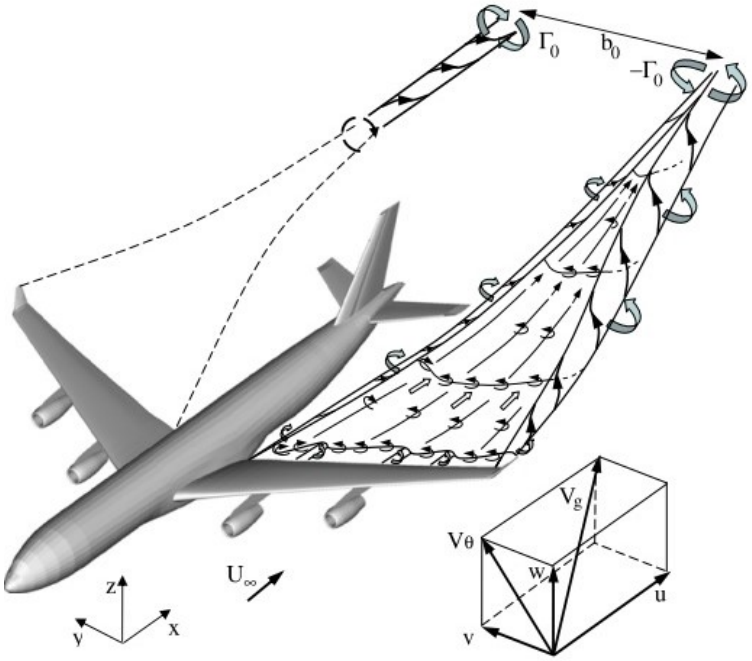

(b)

Figure 2.3 (a) Wake regions downstream the wing (b) Aircraft wake [15]

The merging flow between the two surfaces becomes unsteady due to the boundary layer turbulence on the wing, where the vortex core axial velocity gradient induced turbulence is contributing as well [31, 36]. Several studies showed that the vortex axial flow could be affected by the wing-tip geometry. Lee and Pereira [37] used a NACA0015 wing under a Reynolds number of $Re_c = 3 \times 10^5$. They showed that the vortex core depicted a velocity deficit relative to the free-stream velocity when the axial flow is a "wake-like". In contrast, a "jet-like" is characterized with a core axial flow velocity greater than the free-stream velocity. Anderson and Lawton [38] performed measurements with a Reynolds number varying between 7.5 and 12.5 $\times 10^5$. They found that the vortex assimilated a jet-like with a rounded wing-tip when increasing the angle of attack. They showed that with a lower angle of attack, a square tip produced a wake-like axial flow. Giuni et al. [27] considered a rounded and square tips, they showed that small and strong vortices are more generated with a square tip than a rounded tip. Another wake-like axial flow was also reported by Ramaprian and Zheng [39] and Dghim et al. [22–25]. Several authors reported that the vortex is formed from the merging process of smaller vortices, which is strongly dependent on the tip geometry [27, 36, 40–44]. These vortices merge with the main vortex several chord lenghts downstream the wing-tip [33, 45].

The molecular diffusion and turbulent diffusion play a major role in the vortex roll up process [46]. It contributes on injecting vorticity from the shear layer into the vortex [33]. The roll up completion was subject to different conclusions, Shekarriz et al. [47] considered that the roll up phase is complete when the vortex maximum circulation is reached in agreement with [33, 48]. Birch et al. [49] suggested that the roll up was almost complete at the trailing edge. In another study, they suggested that the completion of the vortex roll up phase occurred when the vortex core strength is unchanged [43]. Similarly, Dghim et al. [25] performed Stereoscopic Particle Image velocimetry on a NACA0012, they suggested that the vortex is fully developed when the circulation is unchanged, namely approximately at three chord lengths downstream. Ramaprian and Zheng [39] suggested that completion of the roll up was within two chord lenghts, considering the fact that the vortex core is axi-symmetric. Green and Acosta [42] found that the vortex roll up was achieved in a very close distance behind the trailing edge. Philips [50] suggested that, as long as the spiral wake is distinct from the vortex core, then the roll-up process continues. Once the vortex is fully formed, the fluid near the vortex core rotates as a solid body with high viscosity. In this region, the circumferential velocity profile is nearly linear which reaches a peak at a radial location, $r_{\theta_{max}}$. [33, 51]. A typical profile of the circumferential velocity is shown in Figure (Figure 2.4).

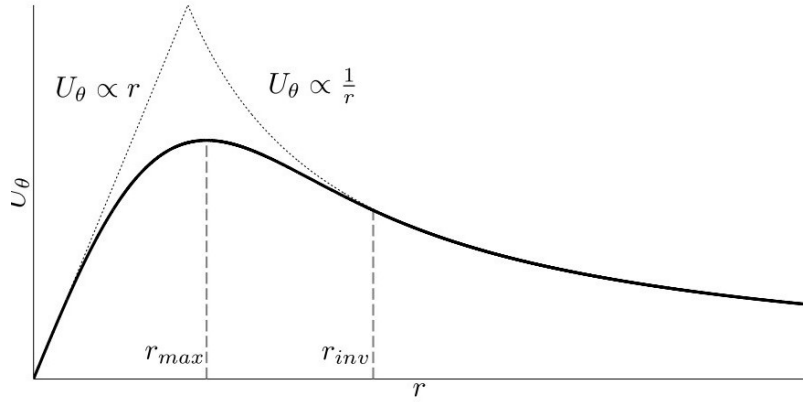

Figure 2.4 Typical radial profile of the circumferential velocity [33, 51]

According to Phillips [50], the vortex reaches a self similar state depicted by the presence of three distinct regions (Figure 2.5):

- Region I: Solid body in rotation (high viscous forces dominance)
- Region II: Weaker viscous effects, circulation grows approximately as a logarithmic function [52]

- Region III: Turbulent diffusion and viscous diffusion have merged the spiraling shear layer

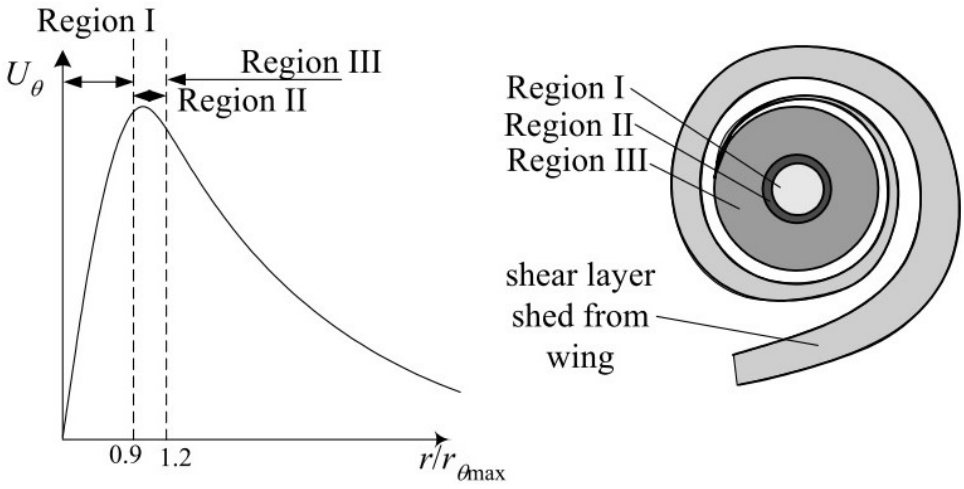

Figure 2.5 Vortex regions [33, 50, 51]

The vortex interacts continuously with the flow, as well as the induced turbulence. Many of the reported studies above used a range of Reynolds numbers : Anderson et al. [38] used a Reynolds number varying between 7.5 and 12.5×10^5, McAlister et al. [53] used

two Reynolds numbers : $Re_c = 1.5 \times 10^6$ and $Re_c = 2.5 \times 10^6$, Garcia et al. [54] used a low Reynolds number ranging from $Re_c = 2 \times 10^2$ to $Re_c = 3 \times 10^2$ for their numerical simulation. A detailed literature review on the interaction of free stream turbulence with a trailing vortex and the meandering phenomena is presented in Chapters 3 and 4 respectively. Additionally, recent papers were presented on vortex coupling [55] and vortex meandering [56–59].

2.3 Vortex characterization

Regardless of the flight phase (take-off, cruise or landing), the presence of wing-tip vortices interact continuously with the external environment. A variety of structures length scales and intensities have a direct impact on the decay of the vortex [51, 60]. To identify the properties of the vortex in space and time, it is commonly generated in wind or water tunnels using fixed surfaces (airfoil, plate...etc.) or vortex generators [61]. The vortex as a fluid body evolving in a helical motion, might be subject to instabilities [62, 63]. If turbulent fluctuations appear, its characterization requires a certain resolution accuracy in order to evaluate the instantaneous properties of the vortex, from which the average data would be obtained. Furthermore, the vortex characterization is based on the identification of the main dynamic properties related to its motion in space such as velocity and vorticity fields. In the recent studies, with the introduction of optical velocity measurement techniques, particle image velocimetry has shown to be a great tool which offers the possibility to map a vortex as it evolves in different plans [51, 64–66]. Flow visualization is another important technique which contributed to evaluate vortex properties. For instance, Pentelow [51] used fluorescent dyeing with illuminating laser sheet for his study performed at three free stream turbulence levels on a vortex generated by a NACA0012 square wing-tip. The vortex structures were visualized and showed how turbulence modified the vortex behavior in Figure 2.6. The author showed the complexity of evaluating the velocity field of the wing-tip vortex using optical velocimetry. In fact, providing the flow with visual particles allowed the laser sheet to illuminate and distinguish the vortex structure. Under turbulent conditions, this process might not be easy as shearing, twisting and deformation of the vortex structure occurred. To optimize the process, the author required a certain smoothing level which was applied on the velocity frames to remove any spatial distortions on the vortex field (Figure 2.7).

Interestingly, additionnal complexity was observed for fully turbulent vortices particularly under controlled conditions as the reproduction in wind tunnel seemed to be difficult [67]. As such, the implication of the numerical simulations provided the vortex

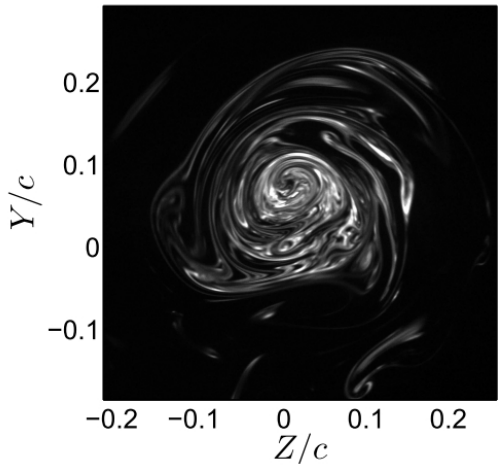

(a)

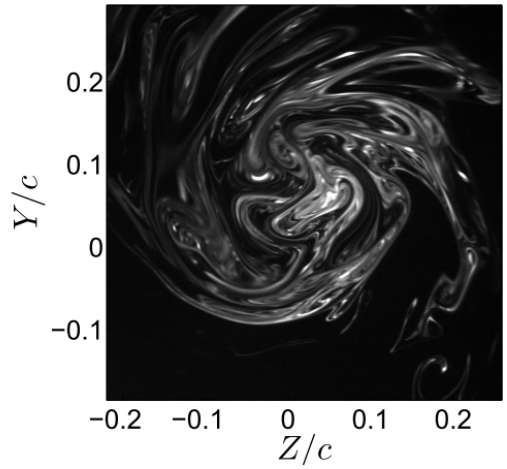

(b)

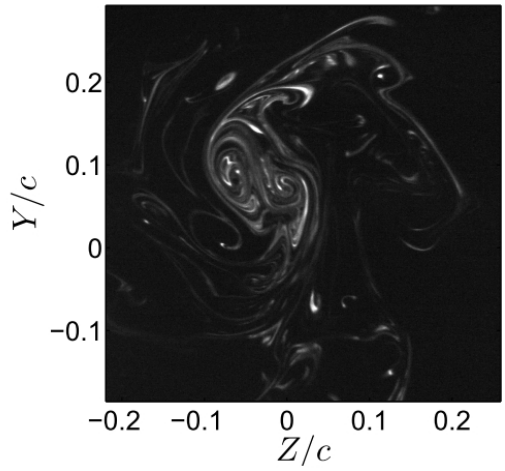

(c)

Figure 2.6 Fluorescent dyeing of the vortex by Pentelow [51] (a) no-grid (b) small grid (c) large grid

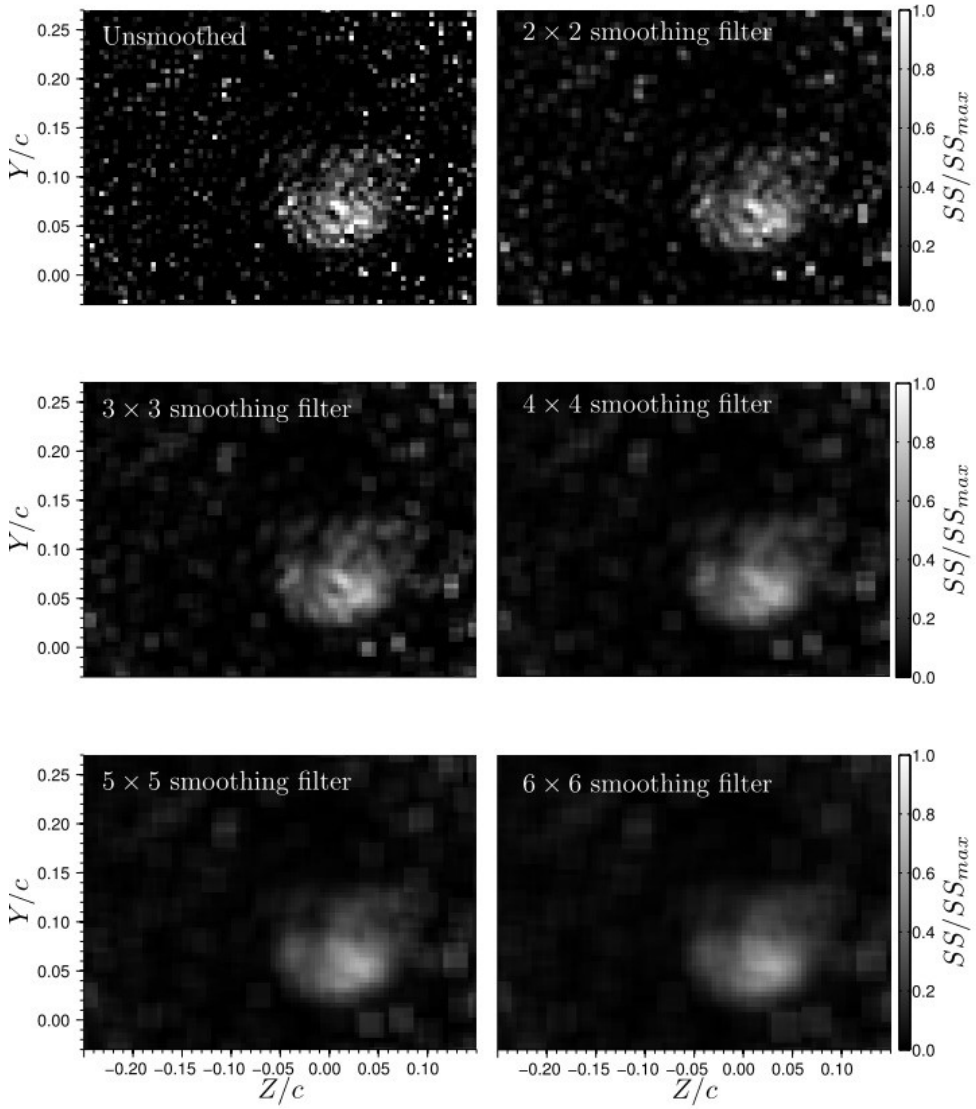

Figure 2.7 Smoothing filters applied by Pentelow [51]

dynamics knowledge with valuable information. The vortex motion is depicted by its horizontal axis fluctuation, known as meandering. This low frequency vortex core movement affects the velocity field and generates undesirable bias on the measurements. Boude et al. [68] showed that by using zonal RANS (Reynolds Averaged Navier Stockes Simulation) /LES (Large Eddy Simulation) approach for tip region which allowed to identify the vortex meandering. The authors reported that it could be the result of upstream turbulence excitation from the boundary layer, and also contributes to noise emission. Hoang et al. [69] used a singularity method applied to viscous and potential flows differential equations, they showed that the wing-tip vortex strength increased with increased angle of attack. The authors also showed that the wing-tip vortex affected the downwash flow on the horizontal tail. Srinivasan et al. [5] used a numerical scheme developed with the Euler and thin-layer Navier-Stokes equations in a curvilinear coordinate system. They reported that their numerical model fairly demonstrated a good estimation of the roll up and formation of the vortex. Churchfield et al. [9] suggested a numerical scheme based on the Navier-Stokes with the Spalart-Allmaras turbulence model (standard and corrected for rotation and curvature) combined with an algebric stress model (Rumsey-Gatski) and a shear stress model. They observed that turbulent quantities within the core region were not accurately computed despite the fact that averaged flow results were in good agreement with the experimental results. Such indication of complexity near the wing-tip comes from the high velocity fluctuations which affect the Reynolds stress component estimation. Ashworth et al. [70] suggested that vortex meandering could be caused by the vortex shedding from the leading edge, particularly at high angle of attack. Furthermore, the authors showed that the vortex center position did not match with the position of high core velocity. Mao et al. [71] used a spectral element method for a wind turbine simulation, based on the Navier-Stokes governing equations with an adjoint. They showed that the vortex meandering could be constant depending on the frequency of the most energetic perturbation in the flow. A vortex, as any other fluid mechanics phenomena, was also characterized using theoretical models. Some models were developped which allow to characterize the vortex properties, such as circumferential velocity or radius using governing equations. A summary of these models was reported by Djojodihardjo [17, 72] and is summarized in the appendices.

2.3.1 Vortex identification

Under wind tunnel flow conditions, it is not easy to visualize the vortex flow without optical solutions (flow viz, dyeing, optical velocimetry). It is commonly assumed that the vortex axis is parallel to the streamwise direction [33, 51]. Due to vortex meandering, the

horizontal axis inclines with an angle Θ (Figure 2.8 Figure 2.9) which could be estimated as [51]:

$$\Theta = tan^{-1}\sqrt{\left(\frac{dp_1}{dX}\right)^2 + \left(\frac{dp_2}{dX}\right)^2} \tag{2.1}$$

This estimation is performed using series of coordinates of each image which are fitted with k order polynomials :

p_1 and p_2 are given as:

$$p_1 = \sum_{n=0}^{k} a_n X^n \tag{2.2}$$

$$p_2 = \sum_{n=0}^{k} b_n X^n \tag{2.3}$$

a_n and b_n are fitted coefficients for a k order polynomial.

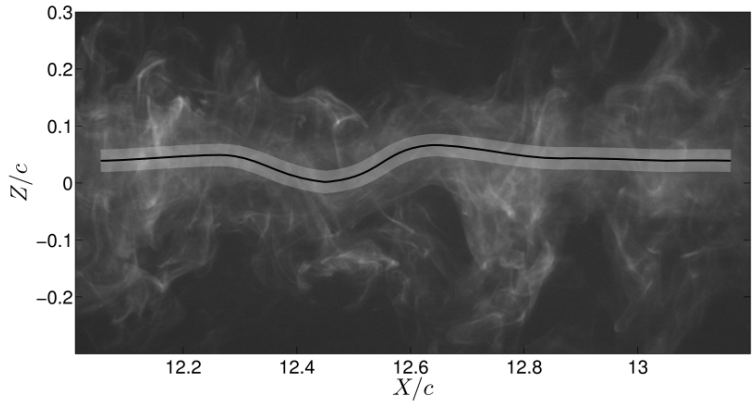

Figure 2.8 Vortex axis identification [51]

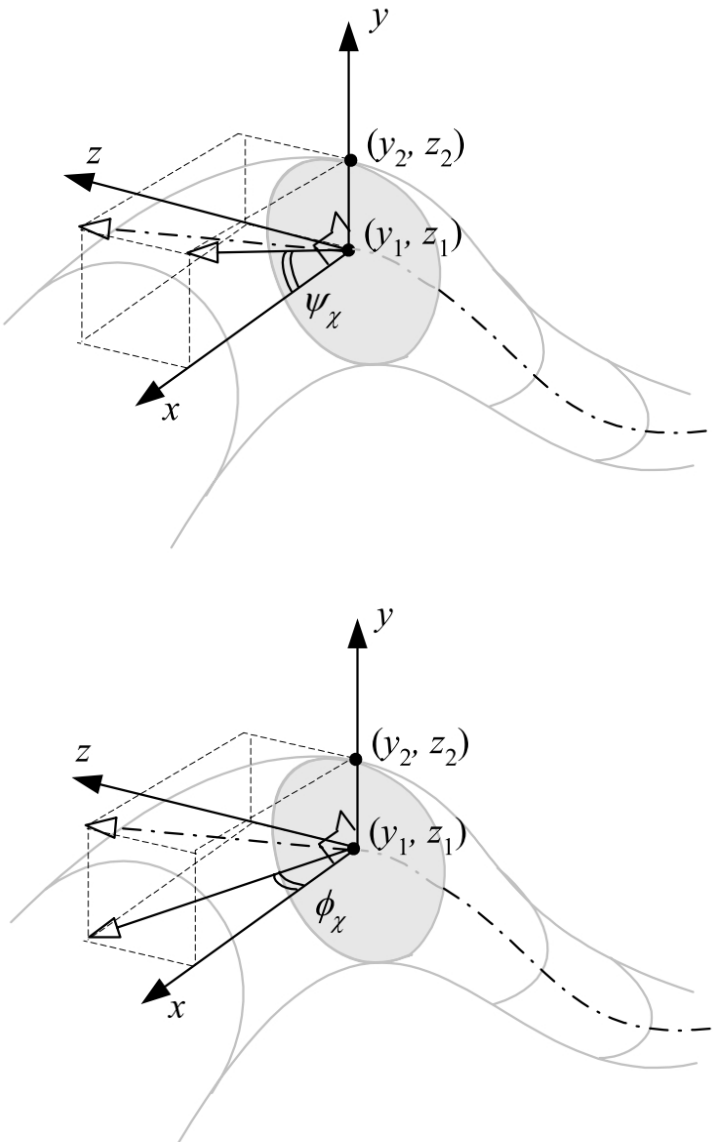

Figure 2.9 (a) Vortex pitch (b) Vortex yaw [33]

Determining the position of the vortex core position is very important as it allows to perform several operations to better assess the vortex properties. Due to the distorted nature of the flow, vortex identification process might become challenging. Several techniques were proposed in the literature which are more or less applied depending on the experimental configuration. The vortex identification techniques could be classified as [73]:

- Techniques using velocity field gradients
- Techniques using Lagrangian structures
- Techniques using vorticity field
- Other techniques

Techniques using velocity field gradients

This technique focuses on identifying the vortex core position using derivatives of the velocity field. Under this technique, several methods could be used such as:

- Axial velocity deficit : Estimates the axial velocity deficit $\Delta U_x = U_x - U_\infty$
- λ_2 criterion : Estimates the pressure minimum across the vortex
- Δ criterion : Using the vorticity and velocity gradient tensors, the sign of the discriminant allows to determine the eigenvalues of the tensors
- Q criterion : Uses the velocity gradient tensor from which the second invariant is determined. The Q criterion stipulates that the vortex region is defined where $Q > 0$, and [51]:

$$Q = \frac{1}{2}\{\|\Omega\|^2 - \|S\|^2\} \tag{2.4}$$

  S : Strain tensor and Ω : Rate of rotation tensor

- Swirling-Strength criterion : Evaluates the swirling motion
  The swirling strenght was given by Pentelow [51] :

$$SS = max\left(0, -\left(\frac{\partial U_y}{\partial Z}\frac{\partial U_z}{\partial Y} - \frac{1}{2}\frac{\partial U_y}{\partial Y}\frac{\partial U_z}{\partial Z} + \frac{1}{4}\left(\frac{\partial U_y^2}{\partial Y} + \frac{\partial U_z^2}{\partial Z}\right)\right)\right) \tag{2.5}$$

- Enhanced Swirling-Strength criterion : Evaluates the inverse spiraling compactness parameter
- Triple Decomposition : Estimates the residual vorticity by extracting the shearing motion

Techniques using Lagrangian structures

These techniques focus on particle trajectories [73].

- Direct Lyapunov exponents : Lagrangian coherent structures are determined using the Direct Lyapunov exponents (DLE), which evaluates the material structures using particle trajectories.
- M_z criterion : Evaluates the fluid trajectories where strain acceleration tensor is defined

Techniques using vorticity field

According to Holmen [73], the challenge in identifying the vortex position relies on the fact that shear and swirling motions are non-distinguishable. Therefore, the vorticity based techniques use a common method.

- Vorticity magnitude $|\omega|$
- Vorticity lines
- Kinematic vorticity number N_k

Other less common techniques were reported in the literature [73] :

- Grey scale levels
- Closed / Spiraling streamlines
- Pressure minima
- R-definition
- Sectional Swirl and pressure minimum scheme
- Γ_1 technique [74]

The algorithm used for the above methods could affect the heaviness of the calculations. In some experimental procedures, such as Particle Image Velocimetry (PIV), the resolution and the size of the velocity might not fit well with the chosen technique and the results could be biased.

In our study, the quantification of meandering is required, and this is done through the identification of the vortex center position. Some techniques might not be accurate for our case where it is required to separate the velocity fluctuations caused by large scale vorticies from those related to small scale turbulence. Furthermore, our objective is to provide a quantitative analysis on the meandering amplitudes, details of these techniques was previously reported in the literature. This thesis outlines only the technique Γ_1, which is described in details in Chapter 3, as it was found to be very robust for our data.

CHAPTER 3

Free Stream Turbulence Interaction with a Wing-Tip Vortex

3.1 Avant-propos

Auteurs et affiliations:

1. Kamal BEN MILOUD: étudiant au doctorat*
2. Marouen DGHIM: Chercheur post-doctorant*
3. Mohsen FERCHICHI: Professeur*
4. Hachimi FELLOUAH: Professeur agrégé†

†Université de Sherbrooke, Faculté de génie, Département de génie mécanique.
*Collège Militaire Royal du Canada, Département de génie mécanique et aérospatial.

Date de soumission: 24 Juillet 2019

État de l'acceptation: article accepté, en presse.

Revue: Journal of Wind Engineering and Industrial Aerodynamics (Elsevier)

Titre en français:

Interaction entre la turbulence libre et un tourbillon de bout d'aile

Contribution au document:

Cet article contribue à la thèse en évaluant l'effet d'une intensité de turbulence sur la dissipation d'un tourbillon de bout d'aile dans les régions proche et intermédiaire du sillage, en tenant compte du phénomène d'errance des tourbillons.

Résumé en français:

Le développement d'un tourbillon de bout d'aile sous l'effet d'une intensité de turbulence a été analysé dans cette étude. Une aile d'un profil rectangulaire NACA0012 a été utilisée. Le champ de vitesse du vortex a été examiné avec la vélocimétrie par imagerie de particules stéréoscopique pour deux nombres de Reynolds $Re_c = 2 \times 10^5$ et $Re_c = 3 \times 10^5$. Trois

configurations avec des niveaux de turbulence ont été considérés pour effectuer une étude comparative, à savoir 0.5% (vortex libre), 3% et 6%. Il s'est avéré que la turbulence favorise la diffusion du vortex. Son rayon s'est élargit ce qui suggère que la turbulence réduit la vitesse circonférentielle et la circulation du vortex alors qu'il s'écoule en aval de l'aile. Les contours de vorticité ont montré que l'axe du vortex subit une agitation lorsqu'il est immergé dans un écoulement turbulent. Des corrections ont été apportées sur les champs de vitesse pour réduire la turbulence apparente causée par l'érrance du vortex.

3.2 Free Stream Turbulence Interaction with a Wing-Tip Vortex

The interaction of a wing-tip vortex of a rectangular, square-tipped wing having a NACA 0012 airfoil section with a grid-generated turbulent flow was investigated in this paper. The experiments were conducted in the near and mid-wake regions at three free stream turbulence (FST) intensities of 0.5%, 3% and 6%, and at two Reynolds numbers based on the wing chord length, c_w, of 2×10^5 and 3×10^5. Stereoscopic Particle Image Velocimetry (SPIV) and hot-wire measurements were carried out at four downstream positions, namely $x/c_w = 1.25, 3.25, 6.25$ and 7.75. Streamwise velocity contours showed that the wing-tip vortex decayed with increased FST and downstream distance. In the vortex core region, the streamwise velocity decelerated while the vortex adopted a wake-like profile. FST was found to decrease the vortex circulation and to increase the vortex radius and vortex meandering amplitude. When increasing Reynolds number, the grid cases showed little variation of the vortex radius and peak vorticity levels, particularly at larger downstream positions, suggesting that the effects of FST and Re number on the vortex development are independent. The measured total turbulent kinetic energy (TKE) was found to be mostly due to vortex meandering. In that, total TKE levels devoid of meandering showed a virtually turbulence-free vortex core.

Keywords :

Wing-tip vortex, free stream turbulence, Reynolds number, wind tunnel measurements

3.3 Introduction

When a 3D lifiting surface is placed in a flow field, it generates 3D structures at its tips, that persist in the wake, known as wing-tip vortices. These vortices, when produced by a large aircraft, can persist for up to 30 km behind the aircraft [11]. Because of their predominance in airport runways, wing-tip vortices can directly interfere with the flight path of other aircraft and may compromise their safety. Thus, stringent restrictions have been imposed by the International Civil Aviation Organization (ICAO) on the distance separating two aircraft during landing and take-off [75]. The formation and development of wing-tip vortices have been shown to be affected by several parameters such as Reynolds number, $Re = \bar{u}_0 c_w/\nu$, where $\bar{u}_0$ is the local free stream velocity and c_w is the wing chord length, angle of attack (AOA), ground proximity, atmospheric free stream turbulence (FST), buoyancy, wind shear, etc. These are a few reasons for which wing-tip vortices have been studied extensively in the literature and an account of which is detailed in [15, 75]. There

have been several earlier experimental studies that focused on the effect of Re and AOA on the wing-tip vortex dynamics in the wake [37, 38, 43, 53, 62, 76–79]. The main findings were that the mean axial velocity of the wing-tip vortex adopted either a jet-like or wake-like profile, depending on Re and AOA. Other researches focused on the interaction of a wing-tip vortex with FST, measured as $\sqrt{\overline{u^2}}/\bar{u}_0$. Heyes et al. [80] investigated the effect of FST ranging between 1% and 5%. Their PIV measurements at $Re = 10^5$ showed that the radial location of peak circumferential velocity remained unchanged with streamwise position, but its magnitude decreased with increased FST. They concluded that FST had a minor influence on the fully formed vortex, but much of the effect occurred during its roll-up and formation process.

Bailey and Tavoularis [33] performed hot-wire measurements to quantify wing-tip vortex development generated by a NACA 0012 wing at an AOA of 5.6° as it evolved in a grid-generated turbulent flow at Re of 2.4×10^5. They placed the wing at positions such that FST was 2.5% and 5% at the leading edge. The authors showed that the decay rate of the peak of the circumferential velocity increased with increased FST, in agreement with previously reported results [[62][80][60]]. They also reported that vortex meandering, defined as the vortex center random motion, increased with increased FST, which affected the circumferential velocity profiles. Ahmadi-Baloutaki et al. [81] investigated FST effect on a wing-tip vortex at Re of 1.6×10^5 in the near field (x/c up to 1.03), and FST ranging between 0.5% and 4.5%. They reported that increasing FST delayed static stall, enhanced lift, but increased drag. Additionally, they showed that FST decreased the vortex peak circumferential velocity and increased vortex diffusion. Van-Jaarsveld et al. [82] studied the decay of a single and a vortex pair in a grid turbulent flow using particle image velocimetry. For the single vortex case, meandering amplitude was evaluated using the standard deviation of the motion of the vortex. It was found that FST increased the meandering amplitude leading to enhanced vortex decay.

Ghimire and Bailey [83] performed Stereoscopic particle image velocimetry (SPIV) measurements to investigate the vortex decay in a grid-generated turbulent flow at $Re_c = 1.2 \times 10^4$ and two FST values of 2.5% and 5%. The authors observed that increasing FST increased the rate of decay of the peak tangential velocity of the vortex, whereas the rate of increase of core radius remained unchanged. They also performed high speed time resolved PIV on a NACA0012 wing in a water tunnel under FST conditions at $Re = 1.7 \times 10^4$ and they observed that the vortex decayed with increased FST [84]. Additionally, a vorticity stripping was observed when the vortex was subjected to FST, which suggested an ejection of the core fluid into the free stream.

More recently, Bailey et al. [48] revisited their earlier wind tunnel measurements data combined with the experimental results of Ghimire and Bailey [83] and [84] and reported that the meandering amplitude, vortex core radius and vortex turnover time scaled with FST, in agreement with Van-Jaarsveld et al. [82]. However, the authors reported that the meandering amplitude was insensitive to the changes in the integral length and time scales of turbulence.

The effect of turbulence injected by control devices on the structure of a wing-tip vortex was addressed in a few recent studies. In the context of mitigating and weakening the effect of wake vortices, turbulent structures were ingested locally using control devices placed at, or near the wing-tip. Heyes et al. [80] used pulsed span-wise air jets at the wing-tip to perturb a vortex evolving in the near field. They demonstrated that with actuation, a remarkable increase in core radius accompanied with a decrease in peak circumferential velocity and an increase in the core axial velocity deficit were directly related to the added mass of fluid ejected from the wing-tip slot. Greenblatt [80] used a different technique to control the wing-tip vortex consisting of deflecting an outboard flap mounted on a wing semi-span and then, modifying the shear layer above the flap by means of turbulence generated by synthetic jet (SJ) perturbations. He showed that a relatively small control momentum coefficient can produce large changes in the shear layer deflection and the flap pressure distribution with relatively small changes in the local aerodynamic loads. In a more recent study, Dghim et al. [23, 24] used a curved nozzle SJ along the wing-tip. The authors showed that, with the a proper selection of optimal actuation frequencies, the SJ slot led to a more diffuse vortex with a reduced circumferential velocity.

The evolution of wing-tip vortices remains a subject of intense research due to its sensitivity to geometric and flow initial/boundary conditions. While a few papers addressed the effect of FST on vortex diffusion and meandering, there seem to be little research on the effect of Re on the vortex structure while it evolves under the effect of FST. This will be addressed in this paper in which an experimental investigation was performed in a grid generated flow at three different FST intensities and at two $\boldsymbol{Re}$, namely FST of 0.5%,3% and 6% and $\boldsymbol{Re}$ of 2×10^5 and 3×10^5. The objective of this work is to identify any possible non-linearity due to the coupled effect of FST and Re, including possible coupled effect with vortex meandering, at different downstream positions.

3.4 Methodology

3.4.1 Experimental set-up

The experiments were conducted in a closed-circuit, low-speed wind tunnel located in the Department of Mechanical Engineering at Université de Sherbrooke (QC, Canada). The wind tunnel has a test section of 1.82×1.82 m^2 cross section. The flow in the empty tunnel is uniform to within ±3%, with a turbulence level of less than 0.5%. The model used in this study, was a rectangular planform half-wing with a NACA 0012 profile. The half-wing was manufactured from Glass-Filled Nylon Powder using a high resolution 3D printer (Synergeering Group, LLC). The wing had a chord, c_w, of 0.3 m and a semi-span, $b/2$, of 0.9 m, corresponding to an aspect ratio, AR, of 6. The wing was placed 2.7 m downstream the exit of the contraction at an AOA of 5°. The origin of the coordinate system was anchored to the wing-tip at the quarter-chord location with x,y and z axes aligned respectively with the streamwise, spanwise and transverse directions of the wind tunnel reference frame, as illustrated in Figure 3.1.

The experiments were conducted in a closed-circuit, low-speed wind tunnel located in the Department of Mechanical Engineering at Université de Sherbrooke (QC, Canada). The wind tunnel has a test section of 1.82×1.82 m^2 cross section. The flow in the empty tunnel is uniform to within ±3%, with a turbulence level of less than 0.5%. The model used in this study, was a rectangular planform half-wing with a NACA 0012 profile. The half-wing was manufactured from Glass-Filled Nylon Powder using a high resolution 3D printer (Synergeering Group, LLC). The square-tipped half-wing had a chord $c_w = 0.3$ m and a semi-span $b/2 = 0.9$ m, corresponding to an aspect ratio, $AR = 6$ at an angle of attack (AOA) of 5°. The origin of the coordinate system was anchored to the wing-tip at the quarter-chord location with x,y and z axes aligned respectively with the streamwise, spanwise and transverse directions of the wind tunnel reference frame, as illustrated in Figure 3.1.

Table 3.1 Details of the grid geometries and experimental conditions.

	M (mm)	w (mm)	σ	$L_x/M^\dagger$	$\frac{\sqrt{\overline{u^2}}}{\bar{u}_0}(\%)^\dagger$
no-grid	-	-	-	-	0.5
GP1	76.2	25.4	0.43	1.31	3
GP2	76.2	25.4	0.43	1.48	6

† Evaluated at $x/c_w = -0.25$ (position of the leading edge of the wing).

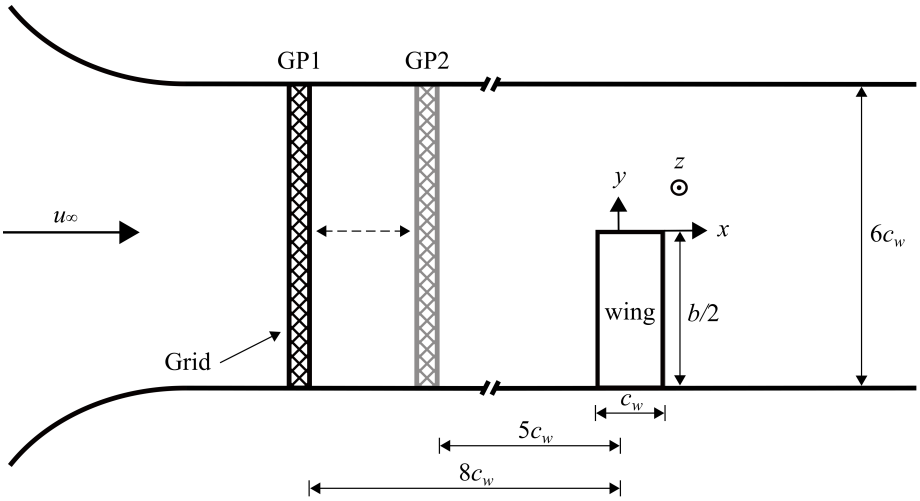

Figure 3.1 Schematic of the experimental set-up

3.4.2 Measurement techniques

Single-point measurements of the grid turbulence were obtained using a miniature single-wire probe (Auspex scientific, AHWU-100) with tungsten sensors having a diameter of 5 μm and a length of 0.9 mm. The probe was powered with a multi-channel constant temperature anemometer (TSI IFA 300). The hot-wire signal was low-pass filtered at a cut-off frequency of 10 kHz (3 dB point) and was sampled at a frequency of 20 kHz, using a 16 bit, 1 MHz analog-to-digital converter (National Instruments PCI-6230). To ensure a good statistical representation of the coherent structures of the flow, records of 2^{20} data points were acquired at each measuring position. The hot-wire probe was positioned in the flow by a two-dimensional, computer controlled traversing system (model: Velmex BiSlide®) having a resolution of 0.02 mm. The single hotwire probe was positioned such that it measures the instantaneous streamwise component of the velocity.

The three components of the instantaneous velocity field in the wake were measured using stereoscopic Particle Image Velocimetry (SPIV). The system consisted of a Quantel Evergreen dual cavity Laser with a maximum pulse frequency of 15 Hz emitting visible green light at a wavelength of 532 nm. The maximum pulse energy of the Laser was 200 mJ. A Laser light steering arm was used to deliver the Laser beam to the light sheet optics which was mounted on an optical rotary table and a two-axes traversing system. This arrangement allowed 5 degrees of freedom for the Laser sheet, covering much of the viewing area of the test section. The airflow was seeded with water-glycol-based fog particles generated by a thermal smoke generator (model: Pea Soup Rocket) that produced particles with a typical diameter of 1 μm. Recording of the particles image pairs was accomplished with two 16-bit double-frame sCMOS cameras having a 2560×2160 px^2 sensor resolution, equivalent to a sensor size of approximately 16.64×14.04 mm^2, and a pixel-pitch of 6.5 μm. The cameras were equipped with Nikon Nikkor fixed focal length of 200 mm adjusted to a numerical aperture of $f_{\#} = 11$. 2000 images were recorded in double-frame mode at a frequency of 15 Hz. The stereo calibration, self-calibration and analysis of the PIV data were performed using LaVision Davis 8.4®. The velocity vector fields were calculated at a final correlation window size of 32 px × 32 px with an overlap of 75%, resulting in a vector spacing of approximately 0.5 mm.

Ensemble-averaged velocity components of the measured flow field were evaluated using the following expression:

$$\bar{u}_{(x,y,z)} = \frac{1}{N-1}\sum_{i=1}^{N} u_{(x,y,z)} \tag{3.1}$$

where N is the number of the PIV independent frames and $u(x, y, z)$ are the corresponding instantaneous velocity fields.

The fluctuations of the instantaneous velocity components were determined as:

$$u'_{(x,y,z)} = u_{(x,y,z)} - \bar{u}_{(x,y,z)} \tag{3.2}$$

The measurement uncertainty for the velocity vectors was estimated to be about 3%. This value was found using the method reported in Mula [85] and Pentelow [51]:

$$\frac{\delta U}{U} = \sqrt{\left(\frac{\delta\alpha_m}{\alpha_m}\right)^2 + \left(\frac{\delta\Delta X_{CCD}}{X_{CCD}}\right)^2 + \left(\frac{\delta\Delta t}{\Delta t}\right)^2 + \left(\frac{\delta\ U_{seed}}{U_{seed}}\right)^2} \tag{3.3}$$

where $\delta_{\alpha m}$ is the uncertainty of the magnification coefficient, $\delta\Delta X$ is the uncertainty of the displacement of a particle on the CCD, $\delta\Delta t$ is the uncertainty in the time between frames and $\delta\ U_{seed}/U_{seed}$ is the uncertainty associated with the ability of the particles to follow the fluid.

3.4.3 Turbulence field

FST was generated upstream the leading edge of the wing using a squared-mesh grid inserted after the wind tunnel contraction. The grid was constructed using wooden bars overlapped in a bi-planar array and firmly fixed to an aluminum frame. The grid had a mesh size, M, of 76.2 mm and a solidity, σ, of about 0.44. Hot-wire measurements of the flow downstream of the grid along the wind tunnel center line, when the latter was placed at a position (GP1) of $8c_w$, and at a position (GP2) of $5c_w$ upstream of the location of the wing's leading edge were performed at Re_1 of 2×10^5 and Re_2 of 3×10^5. Figure 3.2a shows the variation of the streamwise turbulence intensity, $\sqrt{\overline{u^2}}/\bar{u}_c$ ($\bar{u}_c$ is the local centerline velocity), along the center line of the wind tunnel. It was found to decay as :

$$\frac{\sqrt{\overline{u^2}}}{\bar{u}_c} = A\left(\frac{x_g - x_{g_0}}{M}\right)^{-n} \tag{3.4}$$

where $A = 0.98$ and $n = 1.2$. The figure shows a good collapse of the data for cases GP1 and GP2 with the empirical fit. The value of n is well within the range of previous experimental values of n between 1 and 1.45 as reported in [86].

The streamwise development of the measured integral length scales, L_x, is plotted in Figure 3.2b, for the two grid positions. The integral length scale increased downstream as :

$$L_x \propto (x_g - x_{g_0})^n \tag{3.5}$$

where $n = 0.4$ for GP1 and GP2, respectively. The values of the exponent n are in agreement with those reported in [87–90]. The turbulence intensity at the leading edge of the wing was measured to be 3% and 6% when the grid was positioned at GP1 and GP2 upstream of the wing, respectively. Careful examination of the streamwise development of the turbulent quantities of each of the grid cases showed that Re number had little effect on the downstream development of the turbulent intensity. Figure 3.2a depicted that the turbulence intensities of the GP1 and GP2 cases maintained a similar rate of decay at both Re_1 and Re_2. On the other hand, Figure 3.2b showed that the length scales of GP1 and GP2 cases decreased by nearly 20% when Re number was increased to Re_2. However, similar to the streamwise development of turbulence intensities, the length scales of GP1 and GP2 cases maintained the same rate of decay at both Re_1 and Re_2. A comprehensive wake survey was then conducted at the downstream positions $x/c_w = 1.25, 3.25, 6.25$ and 7.75 for no-grid, 3% and 6% and at Re_1 of 2×10^5 and Re_2 of 3×10^5.

3.5 Results and discussion

Traditionally, quantities such as the streamwise and the circumferential velocities, $\bar{u}_x$ and $\bar{v}_\theta$, respectively, and the streamwise vorticity, $\bar{\xi}_x$, are evaluated to assess the wing-tip vortex evolution in the wake. These will be presented in this section.

3.5.1 Streamwise velocity deficit

Contour plots of the normalized streamwise velocity deficit, $\bar{u}_d = (\bar{u}_0 - \bar{u}_x)/\bar{u}_0$, where $\bar{u}_0$ is the local free-stream velocity, are shown in Figure 3.3a, 3.3d and 3.3g for the no-grid case, Figure 3.3b, 3.3e and 3.3h for GP1 and Figure 3.3c, 3.3f and 3.3i for GP2, at the measurement planes $x/c_w = 1.25$, 6.25 and 7.75, respectively, and for $Re_1 = 2 \times 10^5$. Contour plots of the normalized velocity deficit at the same positions and FST intensities were also evaluated at $Re_2 = 3 \times 10^5$ and shown in Figure 3.4. Note at these streamwise positions and Re numbers, $\bar{u}_0$ marginally changed and was no more than 3% higher than

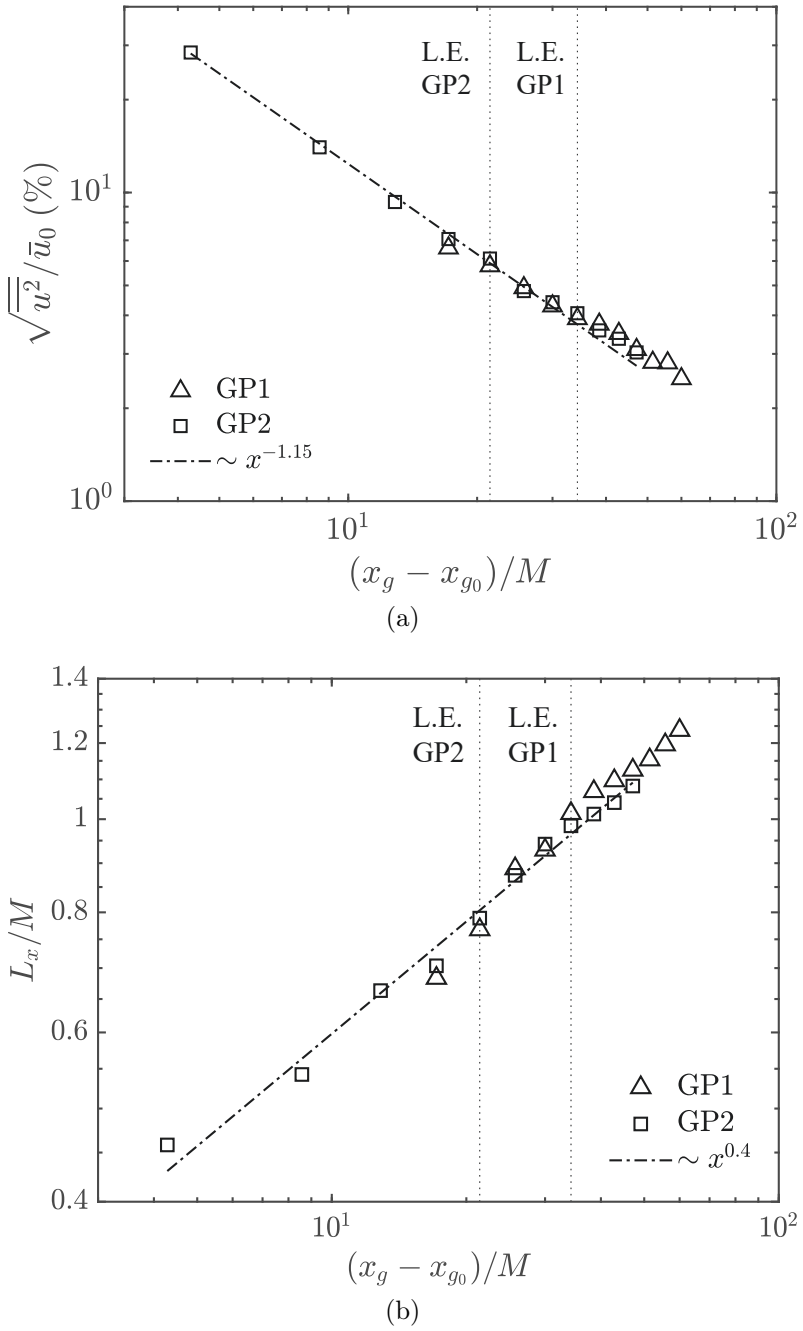

Figure 3.2 Grid flow characteristics at $\boldsymbol{Re}_c 1 = 2 \times 10^5$. (a) Downstream turbulence intensity decay and (b) integral length scale.

$\bar{u}_\infty$. In all cases, the contours outlined the wing-tip vortex structures that displayed wake-like profile with $\bar{u}_d$ in the core region decreasing downstream, in agreement with Lee and Pereira [37], Ahmadi-Baloutaki et al. [81], and Baily and Tavoularis [33].

To further elucidate the effect of FST and Re number on $\bar{u}_d$, peak values of $\bar{u}_d$ at different streamwise positions are plotted in Figure 3.5 for FST intensities of 0.5%, 3% and 6% and $Re_1 = 2\times10^5$ and $Re_2 = 3\times10^5$. As reported in the literature, the current measurements showed that $\bar{u}_d$ decreased downstream with increased FST and Re number led to increased velocity deficit. With increased FST and for the same Re, the maximum velocity deficit at $x/c_w = 1.25$ decreased by nearly 26% and 35% for GP1 and GP2 cases compared to the no-grid case, respectively. Further downstream and at $x/c_w = 7.75$, $\bar{u}_d$ was 60% and 74% smaller for GP1 and GP2 cases with respect to the no-grid case, respectively. Accordingly, the vortex became more diffuse with increased downstream distances and increased FST but no evident changes in the appearance of the vortex structure can de discerned when Re number was increased. To further elucidate the effect of FST and Re number on $\bar{u}_d$, peak values of $\bar{u}_d$ at the vortex core at different streamwise positions are plotted in Figure 3.5 for FST intensities of 0.5%, 3% and 6% and $Re_1 = 2\times10^5$ and $Re_2 = 3\times10^5$. Furthermore, as seen in 3.5, peak values of $\bar{u}_d$ decreased monotonically in the wake but the decay rate was much more significant when the vortex was subjected to FST. More specifically, the no-grid case, the change of $\bar{u}_d$ with x/c_w can be described by a power law with an exponent of -0.18 at Re_1 and -0.19 at Re_2, suggesting that the decay rate is nearly unaffected by Re. However, it appears that the effect of Re number is confined to the wing-tip proximity. In that, increasing Re from 2×10^5 to 3×10^5 caused the values of $\bar{u}_d$ to increase by up to 20% at the farthest downstream position. It may be surmised that much of the Re number effect is limited to the formation stages of vortex. Increasing Re from 2×10^5 to 3×10^5 caused the values of $\bar{u}_d$ to increase by nearly 20%. It appears that much of the Re number effect was limited to the formation stages of the vortex. When the wing-tip vortex was subjected to FST of 3% and 6%, the downstream decay of the peak values of $\bar{u}_d$ can also be described by a power law with a significantly larger exponents, of -0.52 and -0.61, respectively for $Re_1 = 2\times10^5$. Curve fitting suggested that the difference in the values of the exponents for the two Re numbers was less than 8% and 3% for GP1 and GP2, respectively. In contrast, the differences in the value of the exponents for the two FST intensities were 16% and 20% at Re_1 and Re_2, respectively. As such, FST had a greater effect on the streamwise velocity of the vortex compared to Re number, after its formation.

3.5.2 Circumferential velocity

To further examine the wing-tip vortex evolution in the wake, the radial variations of the ensemble-averaged circumferential velocity, $\bar{v}_\theta$, were evaluated. The profiles of $\bar{v}_\theta$, shown in Figure 3.6, were calculated using the measured Cartesian velocity components, $\bar{u}_y$ and $\bar{u}_z$, as:

$$\bar{v}_\theta = (\bar{u}_z - \bar{u}_{zc})\cos\theta - \left(\bar{u}_y - \bar{u}_{yc}\right)\sin\theta \tag{3.6}$$

where $\bar{u}_{yc}$ and $\bar{u}_{zc}$ are the local spanwise and transverse velocities of the ensemble-averaged vortex center, respectively. The circumferential velocity was expressed in the polar coordinates (r,θ), centered around the ensemble-averaged vortex center position. The circumferential velocities were plotted as a function of the radial distance from the vortex center. The profiles were averaged at each radial interval. The vortex radius, r_c, was defined as the distance from the vortex center to the radial location of the peak value of $\bar{v}_\theta$. This region, enclosed by the circle of the radius r_c centered at the mean vortex center, is often referred to as the inner core region. Accordingly, the flow outside the core region is termed the outer region of the vortex. The radial distributions of the normalized mean circumferential velocity, $\bar{v}_\theta/\bar{u}_0$, for the no-grid case, GP1 case and GP2 case are shown in Figure 3.6a, 3.6b, 3.6c and 3.6d, for both Re_1 and Re_2 and at x/c_w = 1.25, 3.25, 6.25 and 7.75, respectively. For the no-grid case and for Re_1, the normalized $\bar{v}_\theta/\bar{u}_0$ reached a peak value,$\bar{v}_\theta$,/$\bar{u}_0$, of nearly 0.24 at x/c_w = 1.25, located at a normalized radial position, r^* of about 0.038. At subsequent downstream positions, profiles of the circumferential velocity, $\bar{v}_\theta/\bar{u}_0$, showed little change with downstream distance and essentially no noticeable change in their peak value. When FST=3% (GP1), the gradient of $\bar{v}_\theta/\bar{u}_0$ within the core region decreased when compared to the no-grid case, accompanied with a decrease in the peak value of $\bar{v}_\theta$ and an increase in the vortex radius, r_c, with the effect being more pronounced at larger downstream distances. Further increasing FST to 6% (GP2) resulted in a significant decay in $\bar{v}_\theta/\bar{u}_0$ in the core region as well the outer region of the vortex. Thus, increasing FST promotes vortex diffusion by increasing its radius to nearly twice of that of the no-grid case as the vortex evolved downstream. For the GP2 case and at x/c_w = 7.75, the peak value of the circumferential velocity was less identifiable compared to all other cases. Furthermore, the distribution of $\bar{v}_\theta/\bar{u}_0$ in the outer region of the vortex seemed to asymptate to nearly constant value in agreement with Bailey et al. [91]. The circumferential velocity profiles of all cases studied at $Re_2 = 3\times10^5$ show similar behavior to that observed at Re_1. Nonetheless, peak values of $\bar{v}_\theta/\bar{u}_0$ were found to slightly increase with increased Re number which resulted in a decreased vortex radius.

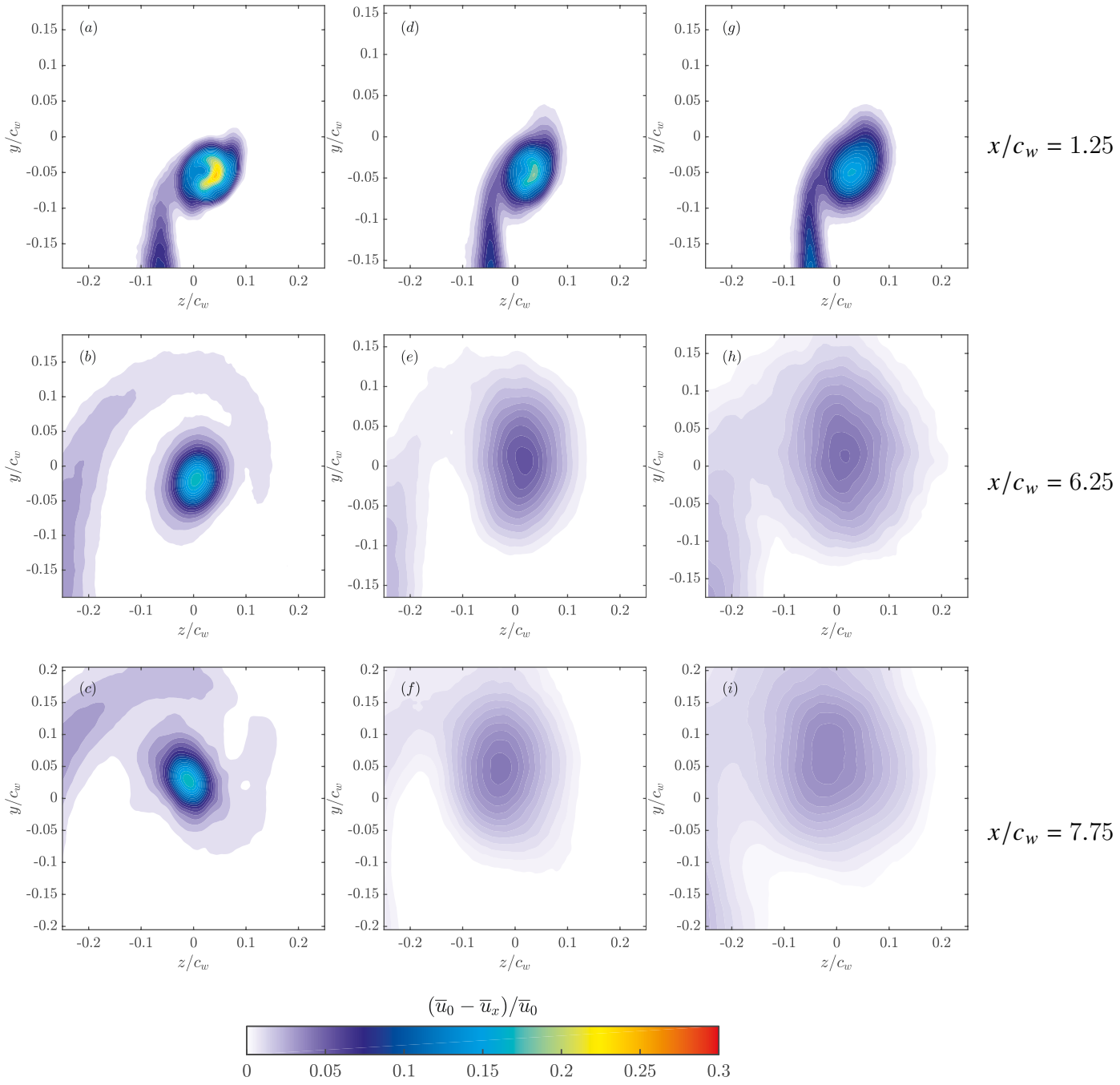

Figure 3.3 Contours of the normalized streamwise velocity deficit at $Re_1 = 2 \times 10^5$. (a), (b), (c): no-grid, (d), (e), (f): GP1 and (g), (h) and (i): GP2.

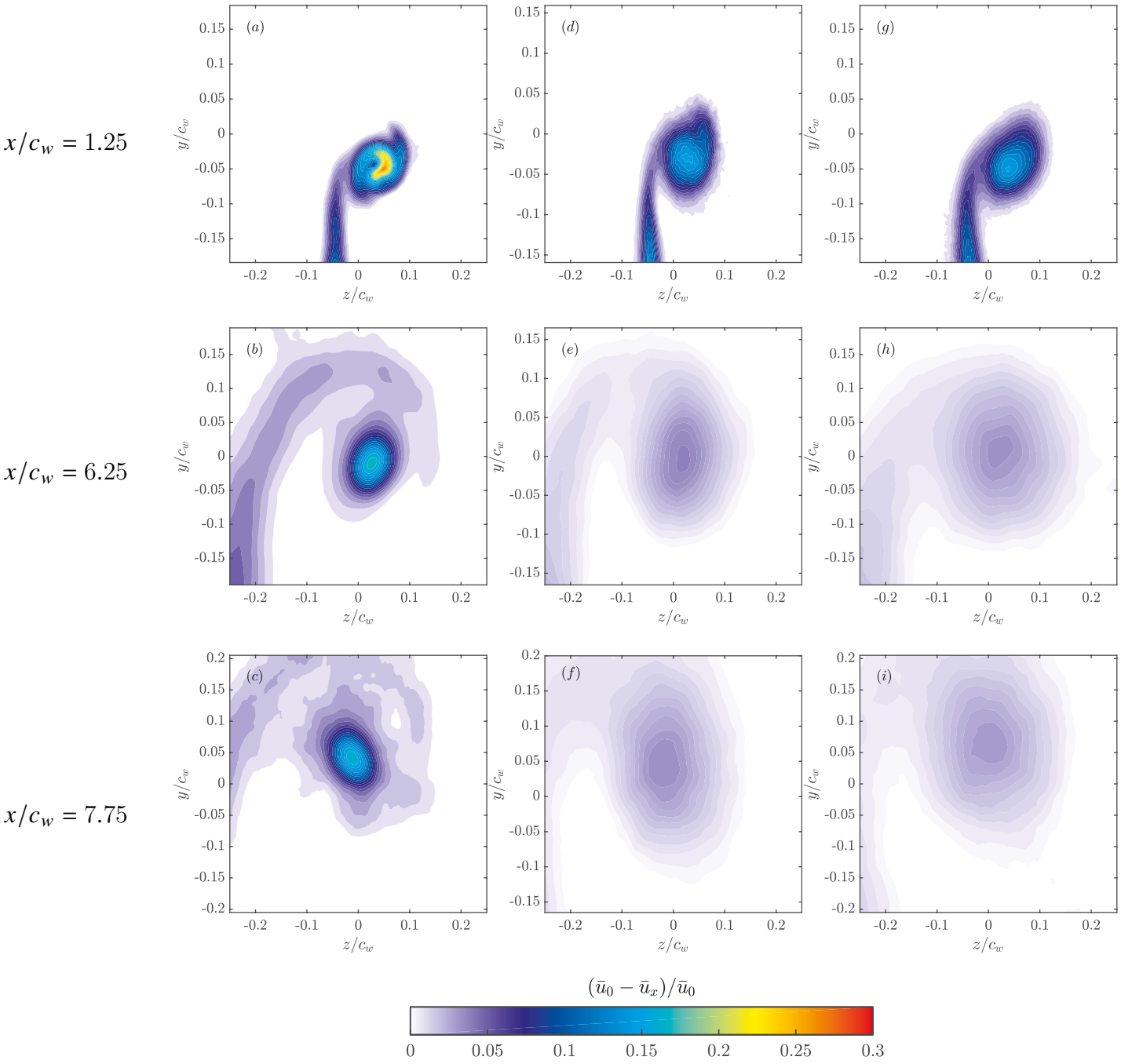

Figure 3.4 Contours of the normalized streamwise velocity deficit at $Re_2 = 3 \times 10^5$. (a), (b), (c): no-grid, (d), (e), (f): GP1 and (g), (h) and (i): GP2.

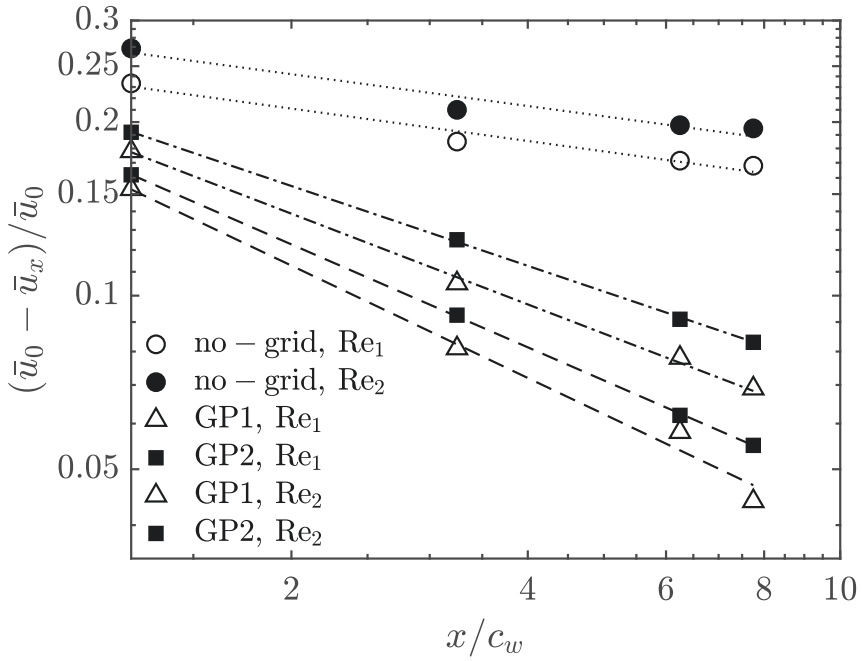

Figure 3.5 Maximum velocity deficit at different downstream positions

For a more quantitative description of the FST and Re number effects on the vortex development, normalized peak values of circumferential velocity, $\bar{v}_{\theta_m}/\bar{u}_0$, and normalized vortex radius, r_c/c_w, at different streamwise positions are plotted in Figure 3.7 for FST intensities of 0.5%, 3% and 6% and $Re_1 = 2 \times 10^5$ and $Re_2 = 3 \times 10^5$. As illustrated in these figures, peak values of $\bar{v}_\theta/\bar{u}_0$ and r_c/c_w for the no-grid case showed little change with streamwise distance, in that, power-law fits suggested $\bar{v}_{\theta,m}/\bar{u}_0 \sim x^{-0.005}$ at Re_1 and $\bar{v}_{\theta,m}/\bar{u}_0 \sim x^{-0.004}$ at Re_2, and $r_c/c_w \sim x^{0.006}$ at Re_1 and $r_c/c_w \sim x^{0.004}$ at Re_2, in agreement with the exponents reported in [33, 91]. This further suggests that, the rate of change of the vortex core radius and the rate of decay of the peak circumferential velocity are independent of Re number. When the wing-tip vortex was subjected to FST of 3% and 6%, the downstream decay of the peak values of $\bar{v}_\theta/\bar{u}_0$ can also be described by a power law with a significantly larger exponents which were nearly insensitive to Re but that strongly depended on FST compared to the no-grid case. Curve fitting suggested that the difference in the values of the exponents for the two Re numbers was less than 8% and 3% for GP1 and GP2, respectively. In contrast, the differences are more significant for FST cases. The value of the exponent for the two FST intensities were 16% and 20% at Re_1 and Re_2, respectively.

It has been shown in the previous section that the length scales of FST for GP1 and GP2 cases were of the same order of magnitude. In particular, at the leading edge of the wing, the normalized turbulence length scales, L_x/M, were measured to be 0.96 and 0.81 for GP1 and GP2 cases, respectively. However, the similar order of magnitude and the rate of increase of both vortex radii ($x^{\sim 0.5}$) and length scales ($x^{\sim 0.4}$) suggests that the ratio r_c/L_x remained roughly constant as the vortex evolves from $x/c_w = 1.25$ to 7.75, as illustrated in Figure 3.9. Therefore, for a particular grid case, the downstream development of the vortex structure is only sensitive to the turbulent intensity, which is the main focus of this study. This conclusion is in agreement with the findings of Van-Jaarsveld [82] in which they reported that the vortex structure and meandering amplitudes were insensitive to the changes in the integral length scales of the turbulence field. When the wing-tip vortex was subjected to FST of 3% and 6%, the downstream decay of $\bar{v}_{\theta,m}/\bar{u}_0$ can also be described by a power law with a significantly larger exponents which were nearly insensitive to Re but that strongly depended on FST compared to the no-grid case. Curve fitting showed that the values of the exponents increased from -0.55 to -0.51 and from -0.60 to -0.58 for GP1 and GP2, respectively, as Re number increased from Re_1 to Re_2.

It has been reported in Phillips [50] that the circumferential velocity profiles in the core of a wing tip vortex adopt a self-similar behavior, when $\bar{v}_\theta$ is normalized by the peak

value, $\bar{v}_{\theta,m}$, and plotted against the normalized vortex radius, $\eta = r/r_c$. The profiles of the normalized circumferential velocity can be described by:

$$\frac{\bar{v}_\theta}{\bar{v}_{\theta,m}} = \left(1 + \frac{1}{2\alpha}\right)\frac{1}{\eta}\left(1 - e^{-\alpha\eta^2}\right) \tag{3.7}$$

where α is the soltution of $e^\alpha = 1 + 2\alpha$, yielding a value of α of about ≈ 1.26. Equation (3.7) along with the experimental data of the no-grid, GP1 and GP2 cases are shown in Figure 3.9a, 3.9b, 3.9c and 3.9d at Re_1, and in Figure 3.9e, 3.9f, 3.9g and 3.9h at Re_2. Inside the vortex core ($\eta \leqslant 1.2$), a slight departure from the theoretical fit is noticeable at $x/c_w = 1.25$. For larger downstream distances $x/c_w \geqslant 3$, the profiles of the normalized azimuthal velocity were found to collapse fairly well with the curve fit proposed in [50], indicating a self-preserved vortex structure.

It may be inferred from the data of Figure 3.9 that, at $x/c_w \sim 3$, the rollup process was completed and the vortex core had evolved asymptotically to reach a nearly axisymmetric distribution. With FST, and at both Re_1 and Re_2, Figure 3.9 shows that neither turbulence nor Re number appear to alter the structure of the vortex core as the profiles of $\bar{v}_\theta/\bar{v}_{\theta,m}$ exhibited a reasonable collapse with the fit of equation 3.7 at all downstream locations, suggesting an asymptotic state of the vortex core.

3.5.3 Streamwise vorticity

Contours of the normalized axial vorticity, $\bar{\xi}_x\ c_w/\bar{u}_0$, are plotted in Figure 3.10a, 3.10d and 3.10g for the no-grid case, Figure 3.10b, 3.10e and 3.10h for GP1 and Figure 3.10c, 3.10f and 3.10i for GP2, at the measurement planes $x/c_w = 1.25$, 6.25 and 7.75, respectively, and for $Re_1 = 2 \times 10^5$.

The axial vorticity contours of the no-grid case clearly show two distinct regions in the flow field; namely the wake shear layer and the wing-tip vortex. The former exhibited a spiral shape with relatively low vorticity levels, whereas the latter contained most of the vorticity within an area of a nearly circular shape with a radius of about $0.05c_w$. Outside the wake and the tip vortex regions, the vorticity was essentially zero. The peak value of the normalized axial vorticity at the center of this region was about 13 at $x/c_w = 1.25$. As the vortex evolved downstream, the wake shear layer thickened and its vorticity levels decreased by nearly 50% at $x/c_w = 7.75$. With FST and under case GP1, vorticity contours appeared to be more diffuse than the no-grid case and covered a larger area around the vortex core.

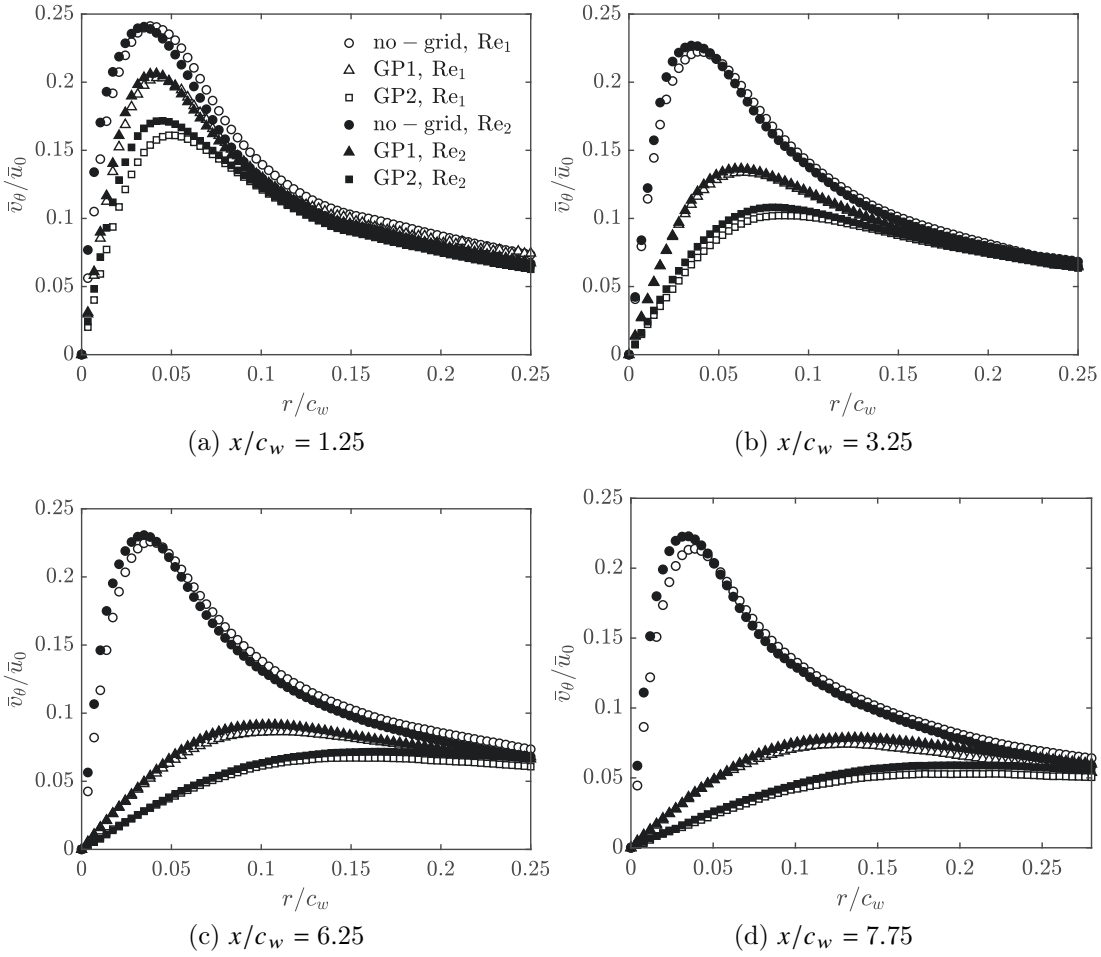

(a) $x/c_w = 1.25$ (b) $x/c_w = 3.25$

(c) $x/c_w = 6.25$ (d) $x/c_w = 7.75$

Figure 3.6 Circumferential velocity profiles at different downstream positions

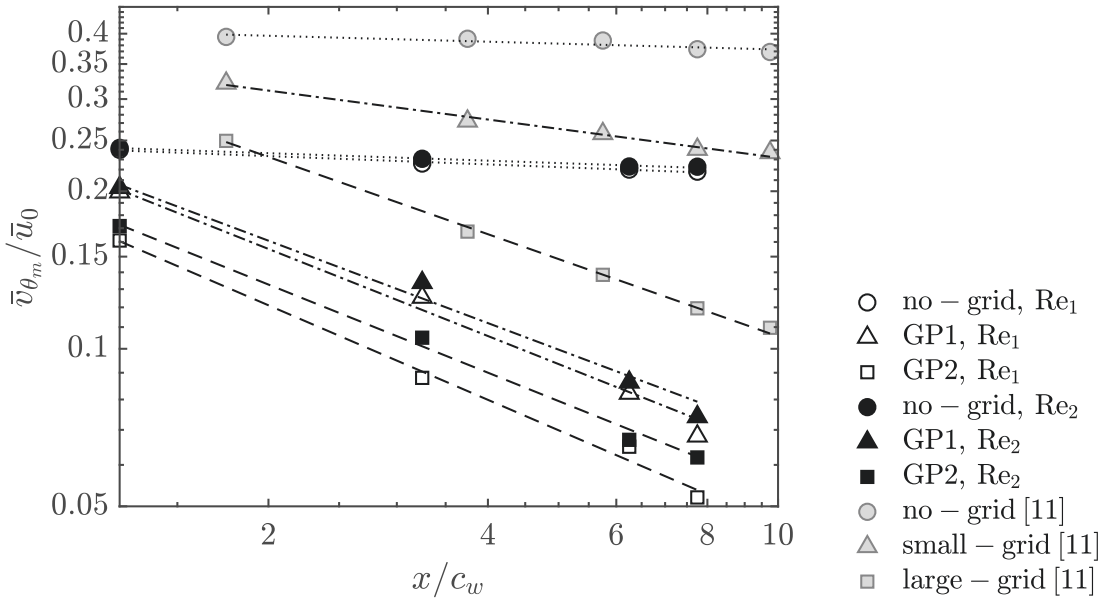

Figure 3.7 Circumferential velocity peak values at different downstream positions

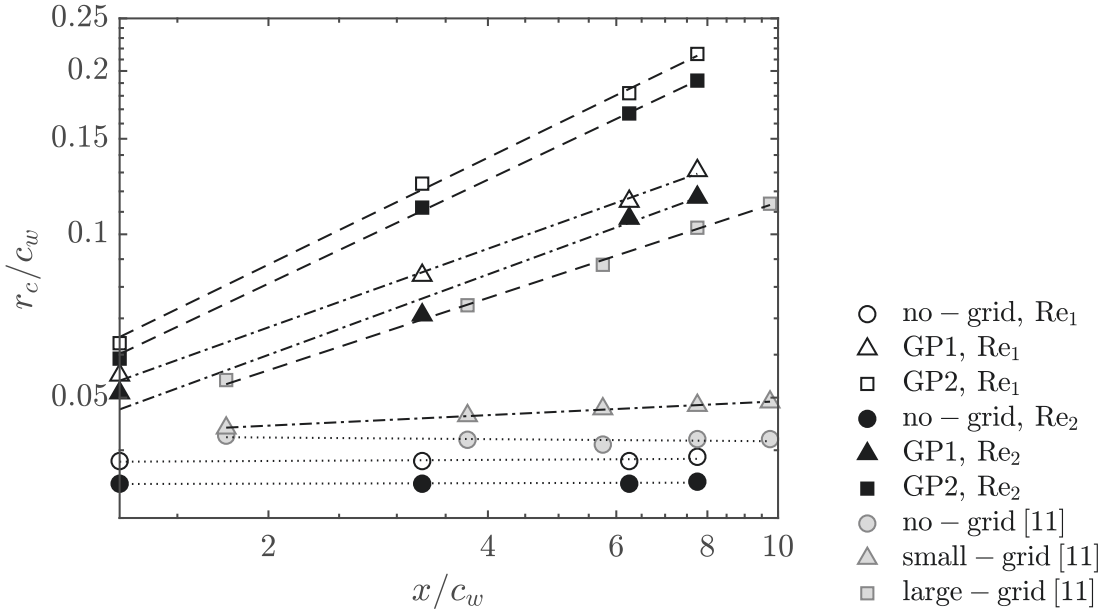

Figure 3.8 Vortex core radius at different downstream positions

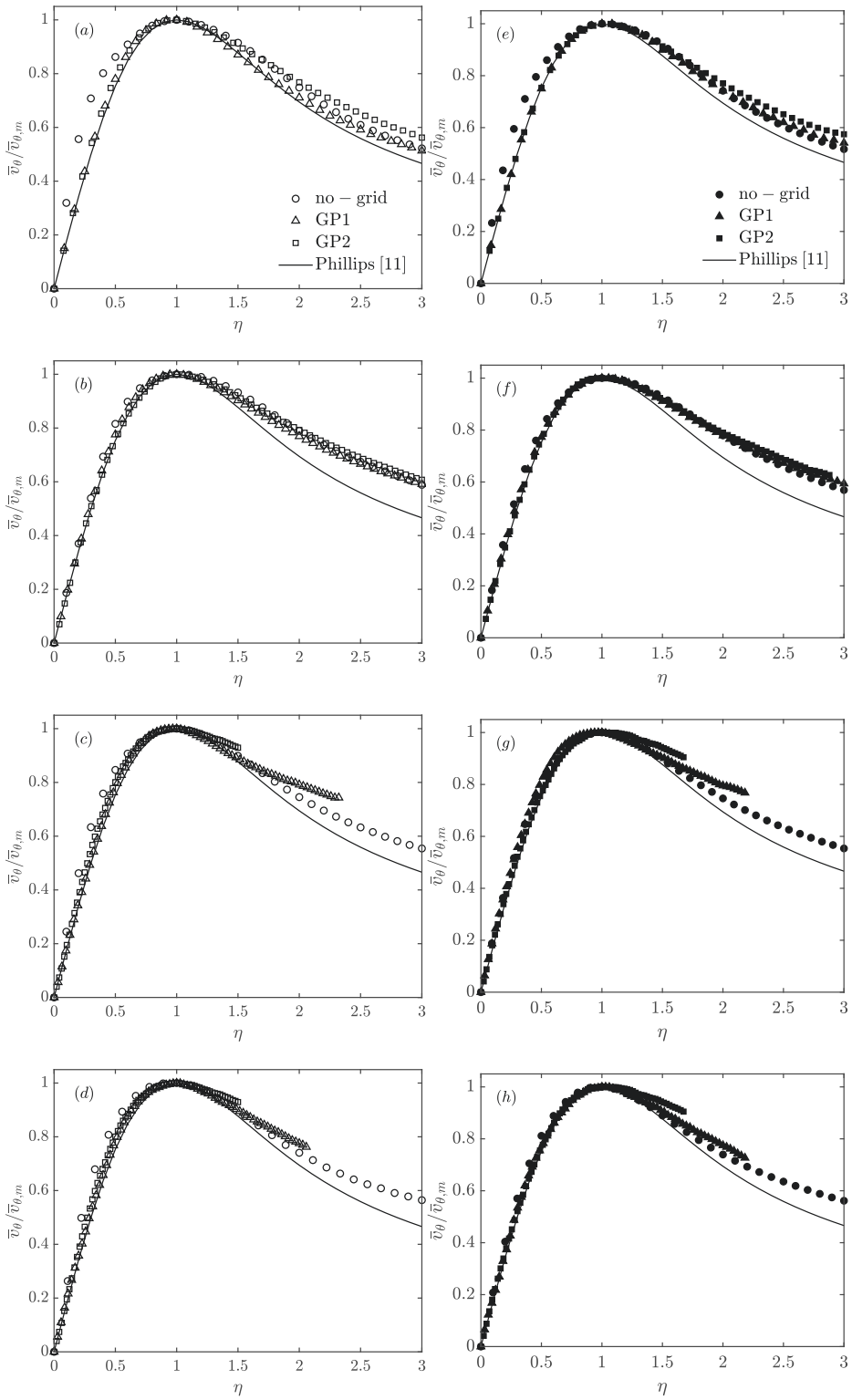

Figure 3.9 Circumferential velocity profiles with the fitting curve of Philipps [50] (a): $x/c = 1.25$, (b):$x/c = 3.25$, (c): $x/c = 6.25$, (d) : $x/c = 7.25$, (a)(b)(c)(d)$Re_1 = 2 \times 10^5$ and (d)(e)(f)(g)$Re_1 = 3 \times 10^5$

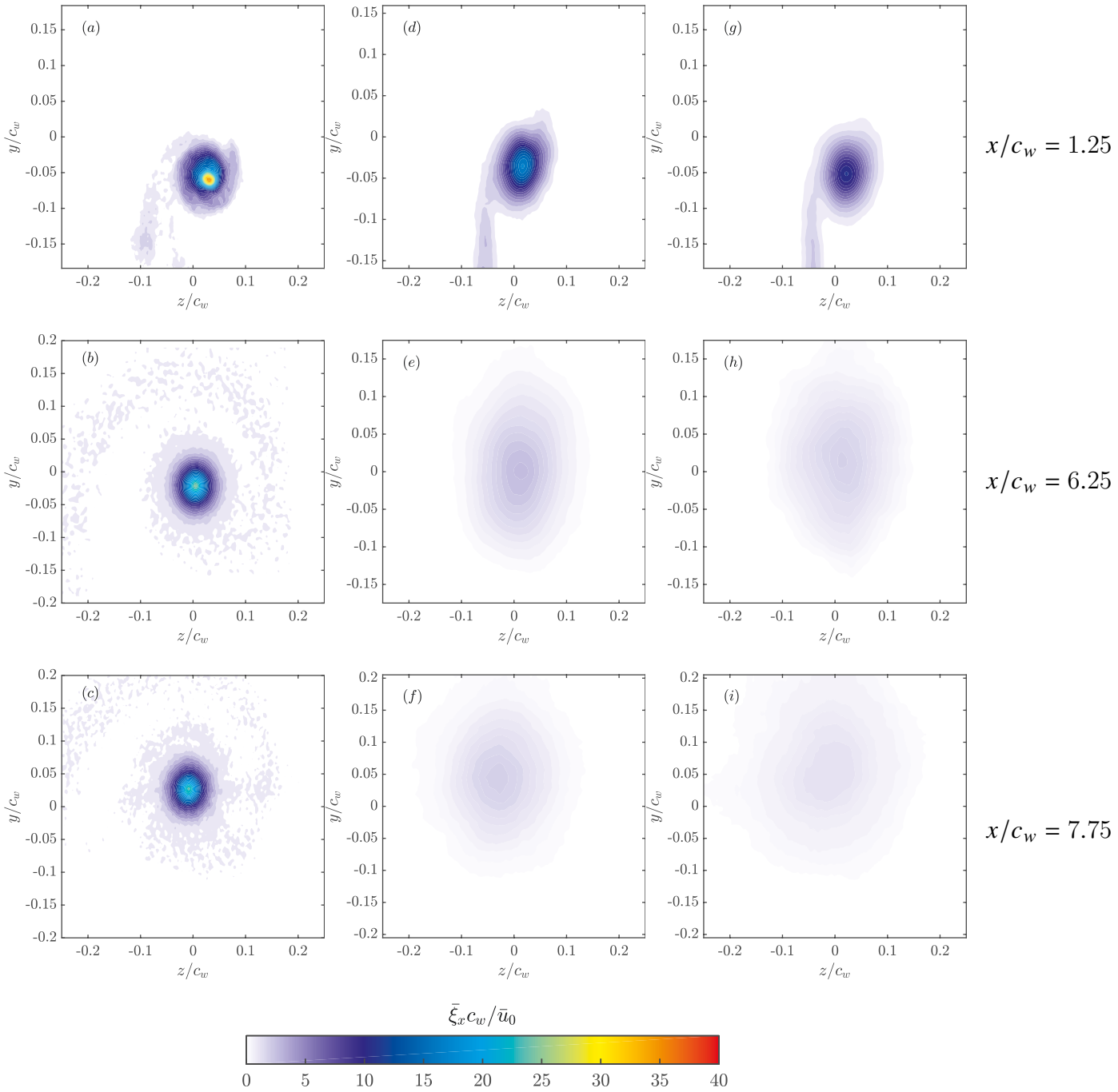

Figure 3.10 Contours of the normalized axial vorticity at $x/c = 1.25$, $x/c = 6.25$,$x/c = 7.25$ for $Re_1 = 2 \times 10^5$. (a)(b)(c): No-grid, (d)(e)(f): GP1, (g)(h)(i): GP2

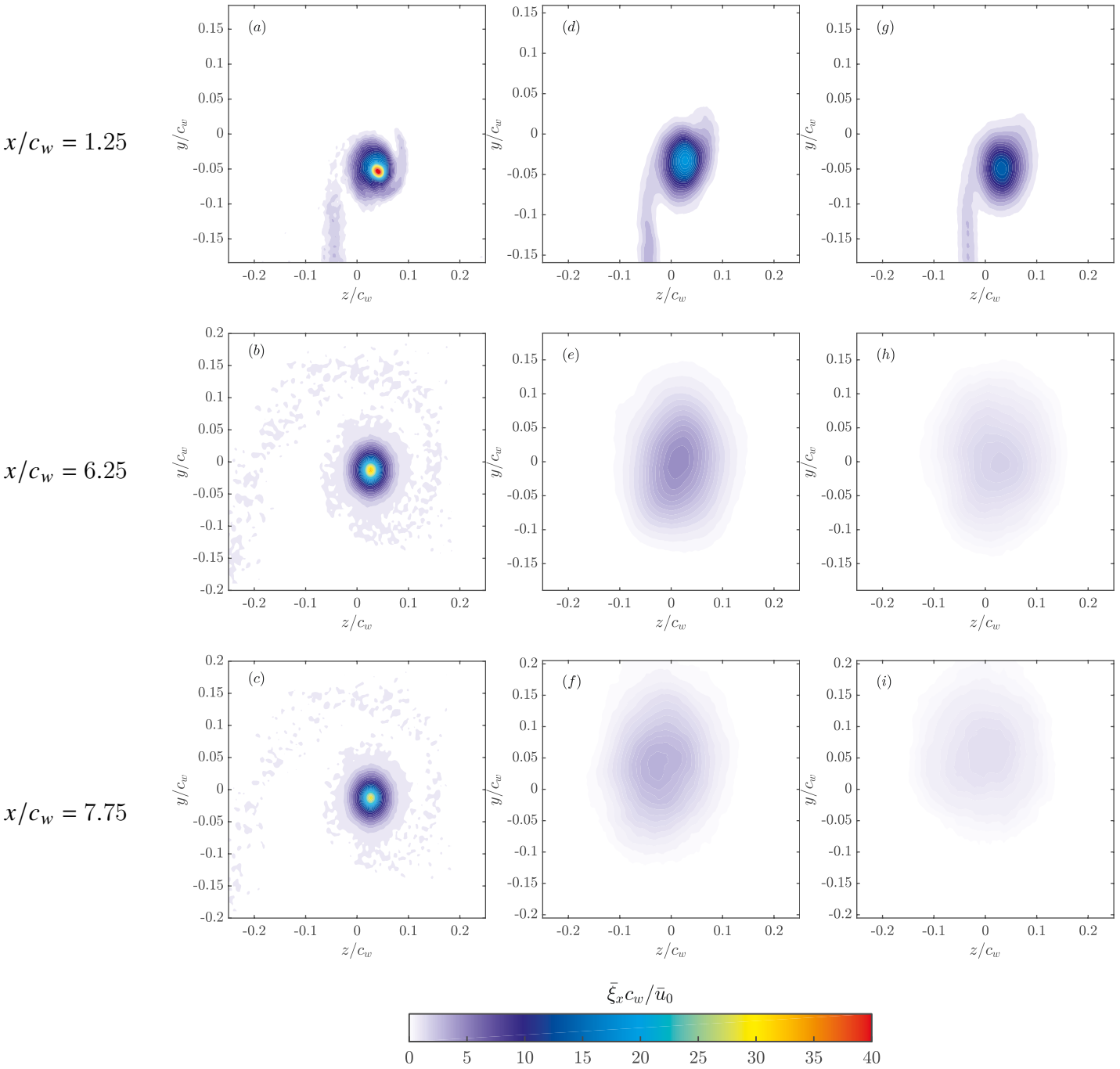

Figure 3.11 Contours of the normalized axial vorticity at x/c = 1.25, x/c = 6.25,x/c = 7.25 for $Re_1 = 3 \times 10^5$ (a)(b)(c): No-grid, (d)(e)(f): GP1, (g)(h)(i): GP2

At $x/c_w = 1.25$, the peak value of $\bar{\xi}_x \, c_w/\bar{u}_0$ decreased by nearly 50% compared to the no-grid case. Further downstream, the peak value of the vorticity decreased substantially from a value of about 20 at $x/c_w = 1.25$ to a value of about 8.5 at $x/c_w = 7.75$. For GP2 case, the higher FST led to a further decrease in the peak value of the axial vorticity at all downstream positions. Note that GP2 case had the most significant impact on the vorticity levels compared to the GP1 case. In fact, over 70% and 50% lower than the no-grid case and GP1 case, respectively. Furthermore, contours of the axial vorticity appeared to cover a larger area around the vortex core region compared to the no-grid and GP1 cases at all downstream positions. At $x/c_w = 7.75$, peak value of the axial vorticity of GP2 case was found to decrease by roughly 60% compared to that at $x/c_w = 1.25$. It can be inferred from these contours along with the data presented in the previous sections that the reduced vorticity levels and peak circumferential velocities, along with increased vortex radius for both GP1 and GP2, that FST enhanced vortex diffusion.

3.5.4 Vortex meandering

It has been well-documented in the literature that wing-tip vortices exhibit a broadband, low-frequency motion of their core which is referred to as vortex meandering. The origin of this low-frequency random motion of the vortex center was not very well elucidated in the literature despite its important effect on the mean averaged velocity field quantities. In the near field, the meandering effect is usually considered negligible however it becomes amplified as the vortex evolves downstream, as reported in [33, 76].

Vortex meandering can be quantified by examining the instantaneous position of the vortex center. A detailed review of the different techniques was reported in [92]. The method used in this paper is based on a non-Galilean invariant approach introduced by [74]. In effect, these positions are extracted from each individual SPIV velocity field by computing a scalar function Γ_1 as (bold indicates a vector quantity)

$$\Gamma_1(P) = \frac{1}{N} \sum_S \frac{(\boldsymbol{PM} \times \boldsymbol{u}_M) \cdot \hat{\boldsymbol{e}}_x}{|\boldsymbol{PM}||\boldsymbol{u}_M|} = \frac{1}{N} \sum_S sin\,(\theta_M)\,, \tag{3.8}$$

where S is a two-dimensional area centred on point P and N is the number of points inside S. θ_M is the angle between the radius vector from P to a point M that lies on S. $\boldsymbol{u}_M$ is the total velocity vector at point M and $\hat{\boldsymbol{e}}_x$ is the unit vector normal to the measurement plane. The vortex center corresponds then to the measurement point where the scalar function Γ_1 is maximum. The advantage of the Γ_1 function is that the velocity fluctuations caused by large scale vortices are separated from those related to small scale turbulence [74]. The

in-plane coordinates of the vortex center positions were then plotted with respect to the ensemble-averaged vortex position $(z_w, y_w) = (0, 0)$, as indicated by the red cross symbol plotted in Figure 3.12. In Figure 3.12a. The standard deviations of the in-plane vortex center position displacement were defined as the meandering amplitudes, namely σ_z and σ_y, in both z and y directions, respectively. The scatter of the instantaneous vortex center positions of the no-grid case at $x/c_w = 1.25$ exhibited a symmetrical motion around the mean vortex position with no particularly preferred direction. As the vortex evolved to at $x/c_w = 6.25$, the meandering amplitudes of the vortex positions scatter were found to increase with the dispersion pattern being symmetrical with respect to the mean vortex center position (as observed at $x/c_w = 1.25$). With FST, the scatter of the instantaneous vortex center positions covered a larger area around the position of the mean vortex center compared to the no-grid case. As the vortex was convected to $x/c_w = 6.25$, the area covered by the scatter of the instantaneous vortex center positions was shown to be larger than those at $x/c_w = 1.25$, particularly for GP1 and GP2.

The streamwise development of the z and y meandering amplitudes, σ_z and σ_y, was summarized in Figure 3.13. For the no-grid case, the meandering amplitudes were found to slightly grow with increased streamwise distance, consistent with the observations reported in [33, 76, 93]. For GP1 and GP2 cases at $x/c_w = 1.25$, the meandering amplitudes, in both z and y directions, were found to be nearly 4 and 8 times higher than those of the no-grid case, respectively. Note that the meandering amplitudes, σ_z and σ_y, were found to rapidly increase with increased downstream distances (roughly an order of magnitude higher) with the effect being more pronounced under the case GP2. It is interesting to note that the meandering amplitudes for all the cases studied seem to decrease with increased Re number at all streamwise positions suggesting a lower meandering-induced turbulence within the vortex core and subsequently a lesser diffuse vortex.

3.5.5 Turbulent kinetic energy

In order to gain further insight into the mechanisms of the vortex decay under the effect of FST, contour plots of the normalized total turbulent kinetic energy, $k/\bar{u}_0^2$, were plotted in Figure 3.14a, 3.15 and 3.14g for the no-grid case, Figure 3.14b, 3.14e and 3.14h for GP1 and Figure 3.14c, 3.14f and 3.14i for GP2, at the measurement planes $x/c_w = 1.25$, 6.25 and 7.75, respectively. The normalized TKE was evaluated using the following expression:

$$\frac{k}{\bar{U}_0^2} = \frac{1}{2}\left(R_{uu} + R_{vv} + R_{ww}\right) \tag{3.9}$$

where $R_{uu} = \overline{u'u'}/\bar{U}_0^2$, $R_{vv} = \overline{v'v'}/\bar{U}_0^2$ and $R_{ww} = \overline{w'w'}/\bar{U}_0^2$ are the normalized streamwise, spanwise, and transverse Reynolds stresses, respectively. u', v' and w' are the fluctuating velocities in the x, y and z directions, respectively, which include both coherent and turbulent components.

For the no-grid case and at $x/c_w = 1.25$, the highest values of $\bar{k}/\bar{U}_0^2$ were concentrated in the wake shear layer region with a peak value of about 7×10^{-3}. The contours showed also a region of concentrated turbulence inside the core of the vortex where the peak value was about 5×10^{-3}. As the vortex evolved downstream, the turbulent kinetic energy in the shear layer decreased as a result of the wake shear layer thickening. Inside the core region, the peak value of the turbulent kinetic energy decreased by nearly 70% as the vortex was convected from $x/c_w = 1.25$ to $x/c_w = 7.75$.

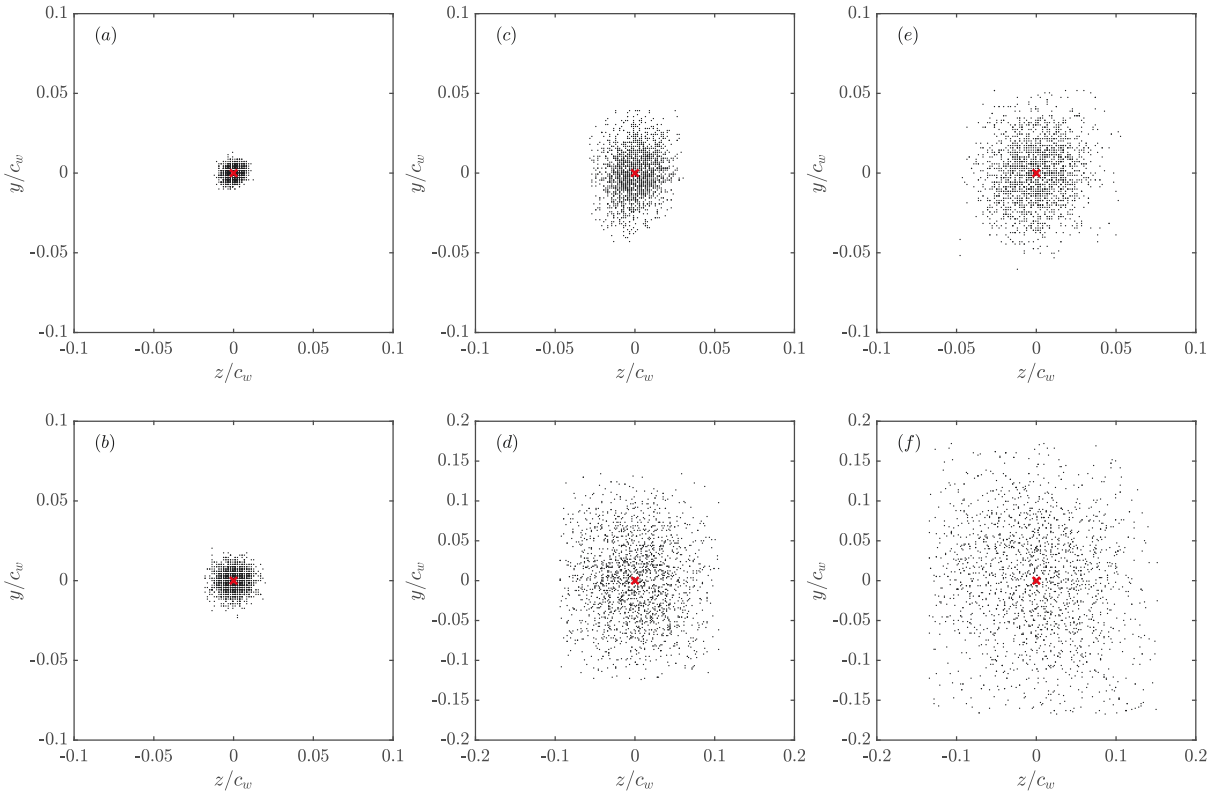

Figure 3.12 Instantaneous vortex center positions at $x/c_w = 1.25$ and 6.25 and for $Re_c = 2 \times 10^5$. (a), (b): No-grid case, (c), (d): GP1 case and (e),(f): GP2 case.

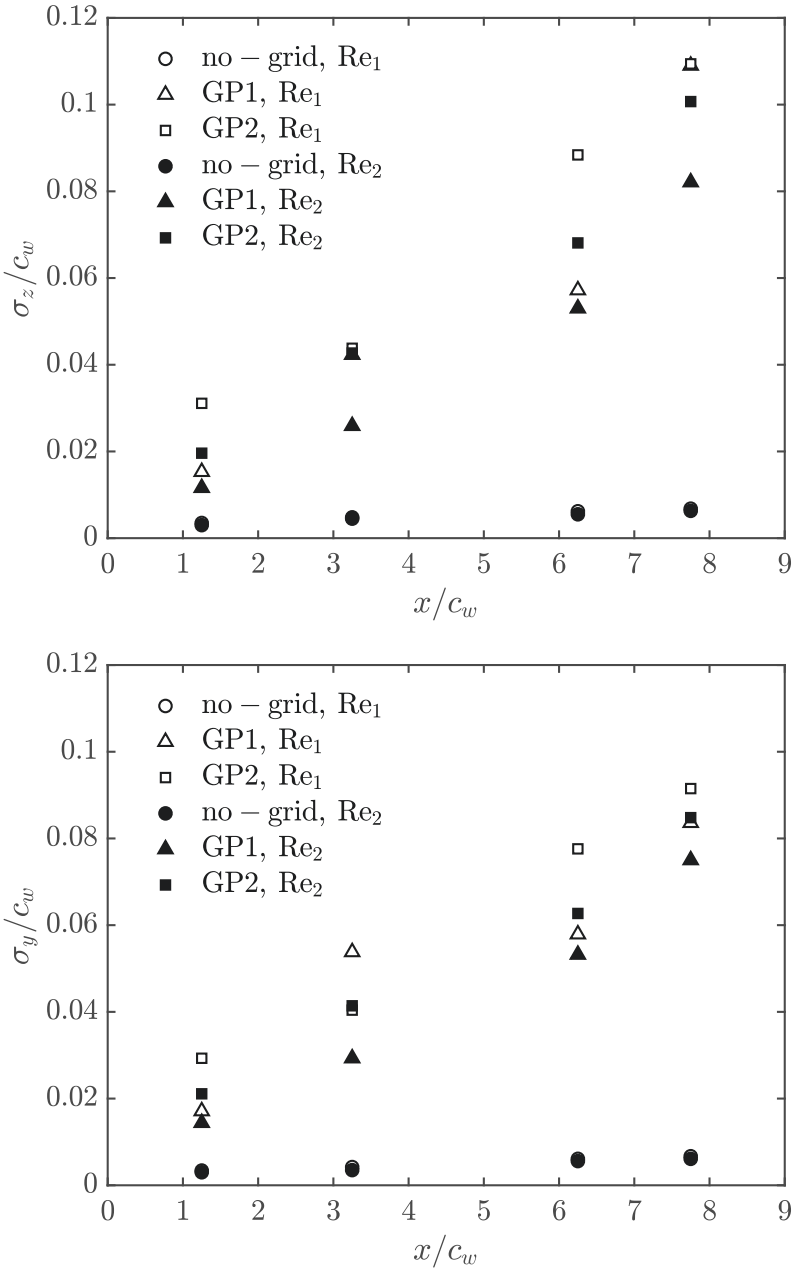

Figure 3.13 Vortex meandering amplitudes σ_z and σ_y at different downstream positions.

This can be attributed to the high viscous effect within the vortex core in agreement with [48]. Under GP1 case, the freestream turbulence entrained by the wrapping vortex structure was found to cover a larger region around the vortex core, with a peak value of about 15×10^{-3}, as reported in [94]. The nearly axisymmetric region of concentrated turbulence evolved into a more axisymmetric shape in the wake as the vortex evolved downstream. Furthermore, the region of high turbulence spread over a larger radial area compared to the no-grid case. Further increasing FST to 6% resulted in an increased levels within the vortex core at $x/c_w = 1.25$. As the vortex evolved to $x/c_w = 7.75$, the increased diffusion of turbulence within the vortex core caused the peak level of TKE to decrease by nearly 40% compared to that at $x/c_w = 1.25$, however it remained significantly larger than those of the no-grid and GP1 cases at the same downstream location. Although the total TKE within the vortex core of the grid cases were essentially higher than that of the no-grid case at increased downstream locations, it is believed that the turbulence introduced by FST may have been greatly reduced due to dissipation and that the turbulence observed at streamwise locations further downstream was mainly due to the effect of long-wave propagation on the vortex structure, i.e. vortex meandering. As mentioned above, the meandering phenomenon is known to create "artificially" induced turbulence within the vortex core as reported in [76, 93, 95]. Due to the significant meandering amplitudes reported in this study, a correction is believed to be necessary in order to isolate the effect of vortex meandering from the effect of FST on the total TKE. Using the correction method reported in [80], the instantaneous vortex velocity fields were realigned such that the instantaneous vortex center positions collocated with the ensemble-averaged vortex center position, directly removing the effect of meandering while retaining the true random fluctuations of the velocity field within the vortex core.

It is worth noting that in contrast to the correction method of Devenport [76], the technique used in this study makes no assumptions about the nature and amplitudes of the vortex meandering as it directly uses the true instantaneous locations of the vortex center positions. Despite the fair prediction of the meandering-corrected velocity field using the technique of Devenport, the latter failed to provide an effective approach to gauge the contribution of meandering to the total TKE of the vortex. The significant vortex diffusion caused by the increased meandering under the effect of FST can be inferred by closely examining the contours of the meandering-corrected TKE. In Figure 3.16a, contours of the raw TKE, $k/\bar{u}_0^2$, of the no-grid case exhibited hight TKE levels within the vortex core surrounded by low levels in the core periphery and the wake shear layer. On the other hand, contours of the meandering-corrected TKE, $\hat{k}/\bar{u}_0^2$, revealed a strikingly different behavior.

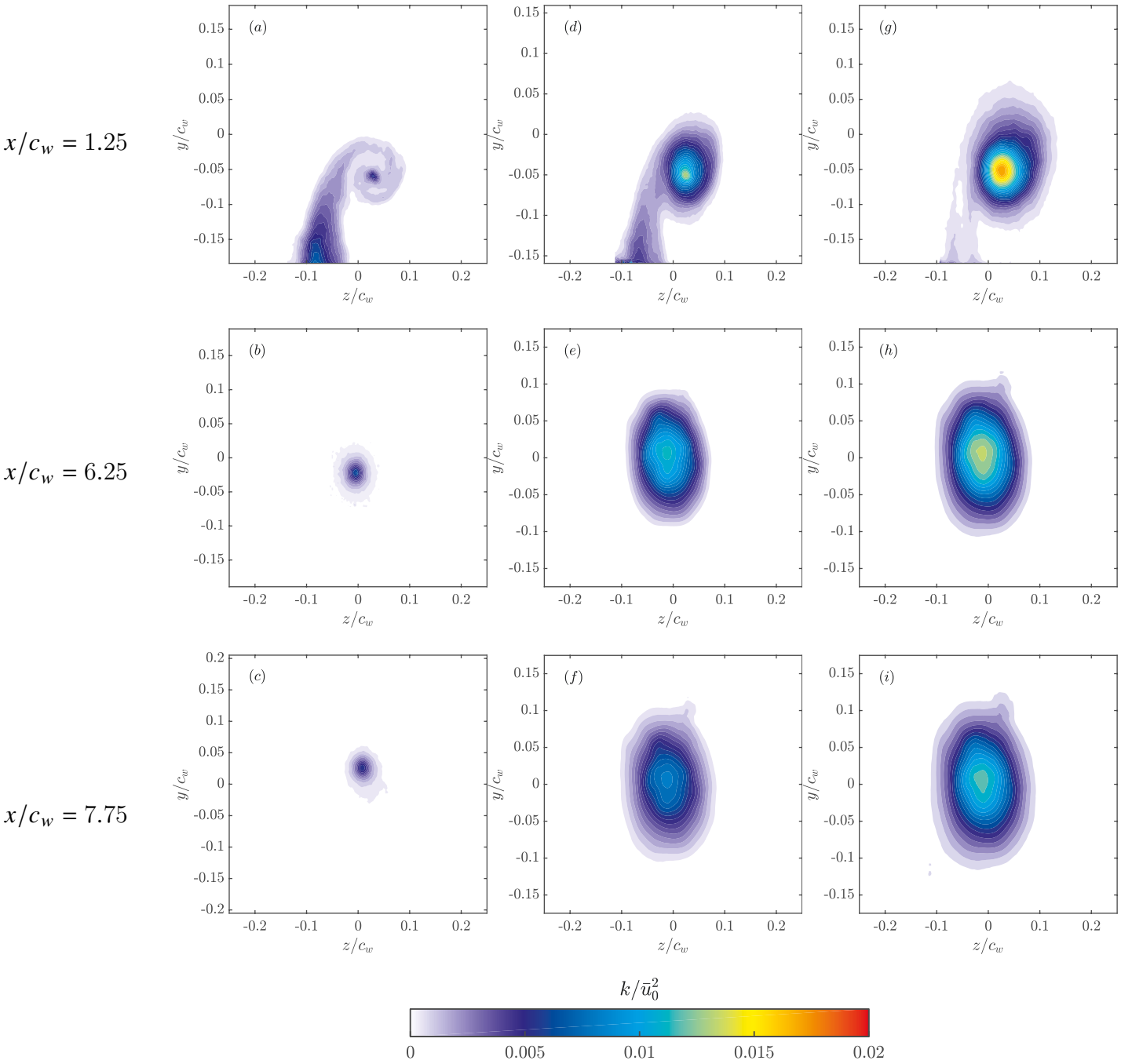

Figure 3.14 Contours of the normalized TKE at x/c_w = 1.25, 6.25 and 7.75. (a), (b), (c): No-grid case, (d), (e), (f): GP1 and (g), (h), (i): GP2

In that, Figure 3.16d showed a turbulence-free vortex core where TKE levels at the vortex center were measured to be zero. Outside the core region, turbulence was evidenced by a region of lower TKE levels surrounding the vortex core. The existence of a laminar core at the center of the vortex surrounded by low turbulence levels near the core radius has previously been observed experimentally by [76, 93, 96], computationally by [79], and has been further supported by the analytical studies of [97, 98]. This behavior arises from the stabilizing Coriolis effects of the strong rotational motion inside the vortex core which tends to relaminarize the turbulent fluid crossing the periphery of the vortex. The existence of the turbulent region around the vortex core is mainly attributed to the strong shearing between the laminar core and the rolling turbulent wake as suggested by [76, 96]. It is noteworthy that the meandering correction was found to reduce the peak level of TKE around the vortex core by nearly 50% compared to the values measured at the vortex core of the uncorrected cases. With correction, the meandering-induced turbulence, represented by the coherent component of the total TKE, was essentially removed from the core region of the vortex structure. Additionally, the size of the region of turbulence around the core was noticeably larger and covered larger radial area. This suggests that more turbulent fluid is believed to be ingested into the vortex core under the effect of FST causing higher turbulent mixing and therefore larger momentum transfer between the turbulent shear layer and the vortex core.

For comparison to TKE, effect of meandering correction on the mean velocity field was also investigated. Self-similar profiles of the uncorrected and corrected ensemble-averaged circumferential velocities at $x/c_w = 1.25$ and for all cases studied, $\bar{v}_\theta/\bar{v}_{\theta,m}$, and $\bar{\hat{v}}_\theta/\bar{\hat{v}}_{\theta,m}$, respectively, were plotted in Figure 3.15 along with Phillips [50] curve fit. Inside the vortex core ($\eta \leqslant 1.2$), all profiles were in agreement with the curve fit suggested in [50], indicating a self-similar behaviour of both corrected and uncorrected vortex structures. Note that, for the no-grid case, the uncorrected circumferential profile showed a slight departure from the fit due to the effect of the initial roll-up process on the vortex inner structure. Outside the vortex core ($\eta > 1.2$), the circumferential velocity profiles exhibited a slight departure from Phillips vortex model. This departure was observed in [65, 91, 99, 100] which may be attributed to the large turbulence levels around the vortex core and the smoothing velocity gradients which may lead to a higher outward spreading rate. In the present work, the meandering correction appeared to have a less discernible effect on the mean velocities as opposed to TKE, as suggested in [93]

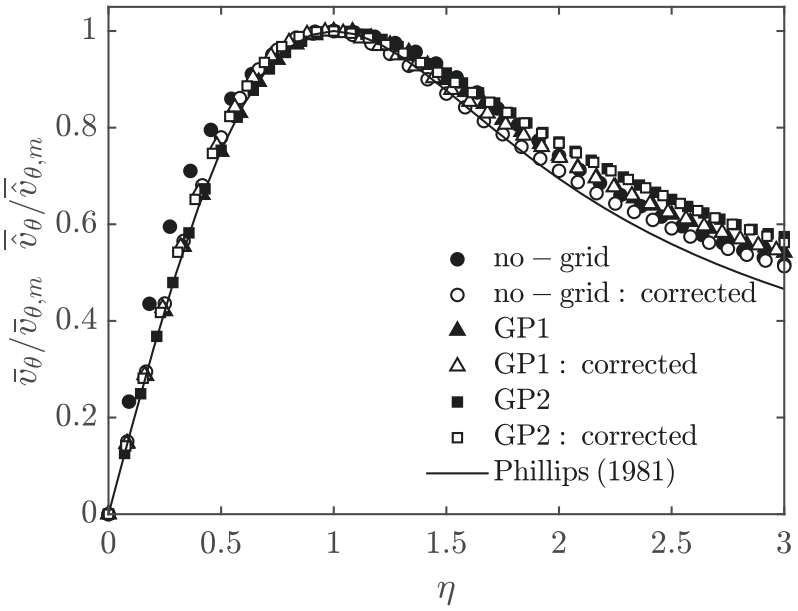

Figure 3.15 Meandering-corrected and uncorrected circumferential velocity profiles with the fitting curve of Philips [50] at $x/c_w = 1.25$.

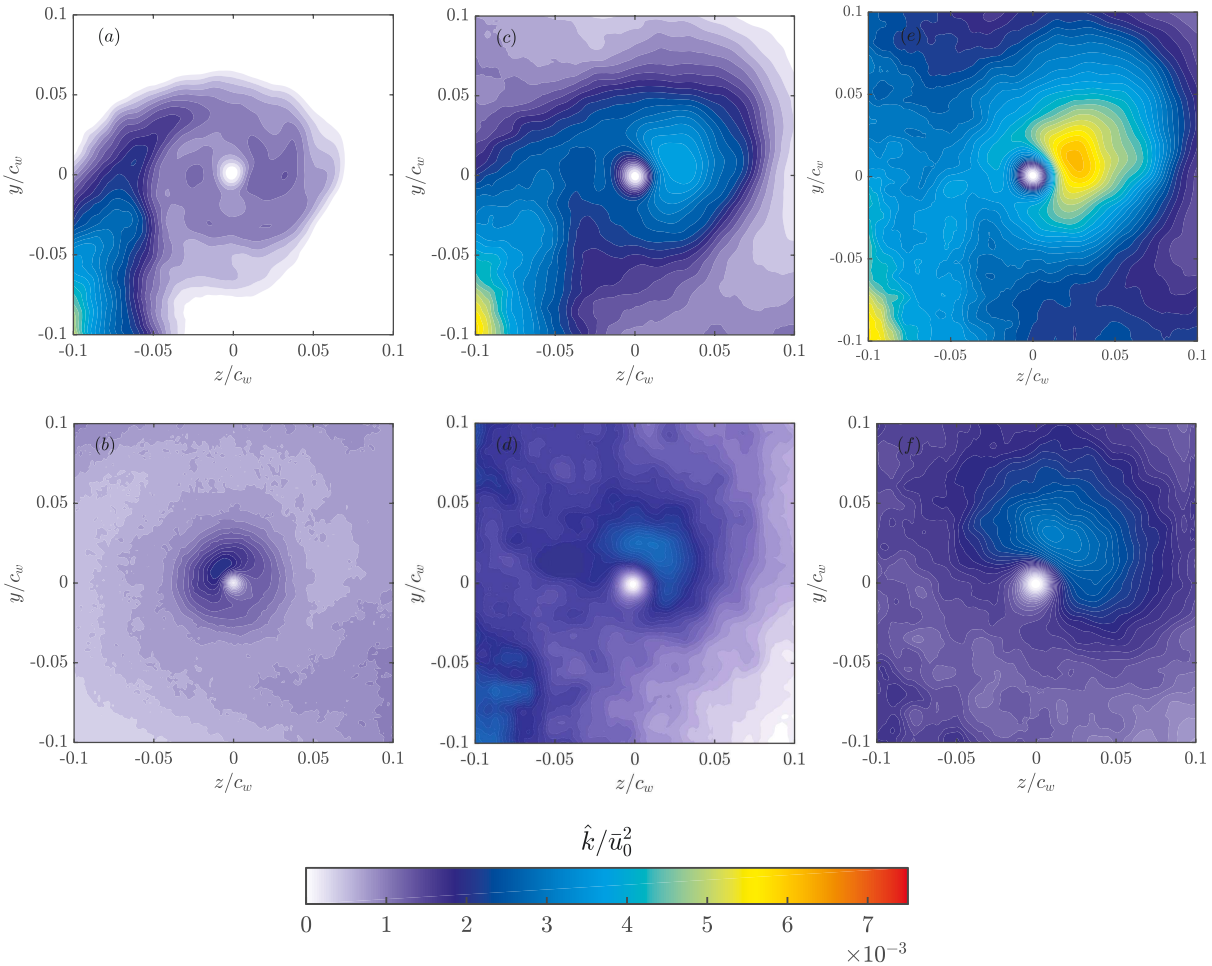

Figure 3.16 Contours of the corrected TKE at $x/c_w = 1.25$ and 6.25. (a), (b): No-grid case, (c), (d): GP1 and (e), (f): GP2.

3.6 Conclusions

In this paper, the interaction of a NACA 0012 wing-tip vortex with a grid-generated flow was investigated. Experiments were conducted in the near and mid-wake regions at three free stream turbulence (FST) levels of 0.5, 3 and 6%, and at two Reynolds numbers, based on the wing chord length, of 2×10^5 and 3×10^5. Stereoscopic Particle Image Velocimetry (SPIV) and hot-wire measurements were carried out at four downstream positions, namely $x/c = 1.25, 3.25, 6.25$ and 7.75. Vortex properties were explored and showed that the wing-tip vortex decayed with increased FST and downstream distance. The vortex core region depicted a decelerated streamwise velocity while the vortex adopted a wake-like profile. To identify any non-linearity between the coupled effect of Re and FST, power-law fitting was applied to the velocity deficit and peak circumferential velocity distribution downstream the wing. It was shown that Re effect was limited to the proximity of the wing. The rate of change of the vortex core radius and the rate of decay of the circumferential velocity were found to be nearly independent of Re. With FST, the power law fitting exponents for the circumferential velocity were found to be larger than the no-grid case, and were strongly dependent on FST. Additionally, FST was found to increase the vortex radius and meandering amplitudes. Increasing Re number showed a little variation of the vortex radius and the vorticity peak for the grid cases, particularly at larger downstream positions. Meandering correction showed that total TKE levels were virtually zero close to the vortex center indicating a turbulence-free vortex core.

Acknowledgments

This work was supported by the Fonds de recherche du Québec - Nature et technologies (FRQNT), Directorate of Technical Airworthiness and Engineering Support (DTAES) office of the Royal Canadian Air Force and the Natural Sciences and Engineering Research Council (NSERC) of Canada.

3.7 Further discussion

3.7.1 Grid flow

Free-stream turbulence (FST) was generated upstream the leading edge of the wing using a squared-mesh grid (Figure 3.17) mounted at the entrance of the test section. The grid was constructed using a set of wooden bars which have been overlapped in a bi-planar array and firmly fixed to an aluminum frame at the inlet of the test section. The width of the bars, w, was chosen to be 25.4 mm with a corresponding mesh size M of 76.2 mm. The ratio w/M was selected based on the definition of the grid drag [101]

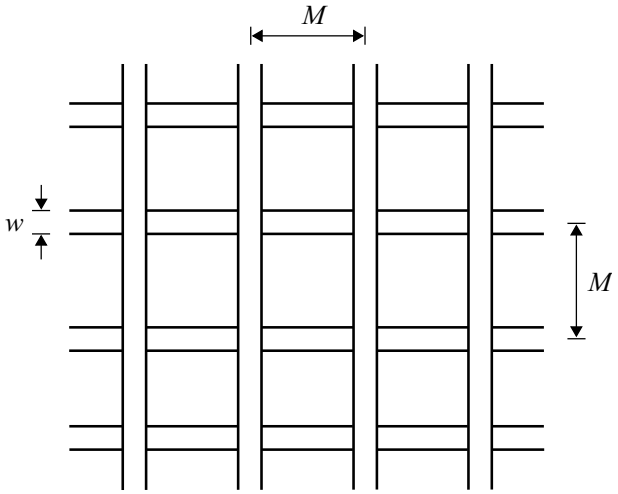

Figure 3.17 Grid geometry

$$C_D = \frac{\frac{w}{M}\left(2 - \frac{w}{M}\right)}{\left(1 - \frac{w}{M}\right)^4} \tag{3.10}$$

Laneville [101] recommended a value of C_D between 3 and 4. Similarly, Vickery [102] suggested a value of about 3.4, whearas Baines and Peterson [103] adopted a much higher value. The grid has a solidity of about 0.44 which was estimated as :

$$\sigma = \left(1 - \frac{w}{M}\right)^2 \tag{3.11}$$

This value was in agreement with those suggested by [104–106].

3.7.2 Vortex circulation

The assembled averaged circulation profile was evaluated by interpolating the values of $\bar{U}_\theta/\bar{U}_0$ in polar coordinates using the following equation :

$$\bar{\Gamma}(r) = \int_0^{2\pi} \bar{U}_\theta(r)\ r\, d\theta \tag{3.12}$$

The radial distribution of the vortex circulation is represented in Figure 3.18 for the no-grid case, GP1 and GP2 cases. As the vortex radius, r_c increased, the normalized circulation monotonically increased. For the no-grid case, an inflexion point could be observed at approximately $r/c \sim 0.01$, another inflexion profile could be seen at approximately $r/c \sim 0.05$ which decribes the extent of the rolling shear layer. Beyond this point, the circulation growth rate decreased as the velocity field converged to the free stream flow (irrotational state [25]). For the GP1 and GP2 cases, the normalized circulation profile depicted a similar trend in comparison to the no-grid case. The normalized circulation profile $\Gamma(r)$ increased with increased vortex radius. The first and the second inflexion points were slightly different. Beyond $x/c_w = 3.25$, the location of the inflexion points seemed to extend with increasing FST and downstream distance. For $x/c_w = 3.25$, the first inflexion point was located at $r/c \sim 0.02$ which increased to $r/c \sim 0.03$ for both $x/c_w = 6.25$ and $x/c_w = 7.75$ for GP1 case. Note that the second inflexion point is sensitively located in the same position for both $x/c_w = 6.25$ and $x/c_w = 7.75$ respectively. GP2 case did not depict a clear second inflexion point for $x/c_w = 6.25$ and $x/c_w = 7.75$. This suggests that FST for GP2 caused an increased outward diffusion of the vorticity with a broadening of the vortex size in comparison to the no-grid and GP1 cases, in agreement with [22, 25]. To further examine the effect of FST on the vortex development, the vortex core circulation,$\bar{\Gamma}_c$, was evaluated and is defined as:

$$\bar{\Gamma}_c = r_c \int_0^{2\pi} \bar{U}_\theta(r_c)\ d\theta \tag{3.13}$$

The streamwise development of the normalized vortex core circulation is illustrated in Figure 3.19. For clarity, the normalized core circulation,$\bar{\Gamma}_c$, was normalized by the no-grid case circulation $\bar{\Gamma}_{c_0}$. The normalized core circulation increased downstream and FST level respectively. At $x/c_w = 1.25$, the GP2 case depicted higher values in comparison to the no-grid case, particularly at $x/c_w = 7.75$ where the ratio between the core circulation and the no-grid core circulation was about 1.4. The rate of increase of $\bar{\Gamma}_c/\bar{\Gamma}_{c_0}$ depicted a linear

shape for GP1 and GP2 cases. Beyond the estimated fully formed vortex position, $x/c_w \sim 3$, the increase in $\bar{\Gamma}_c/\bar{\Gamma}_{c_0}$ might indicate an increase of the wing bound circulation [22].

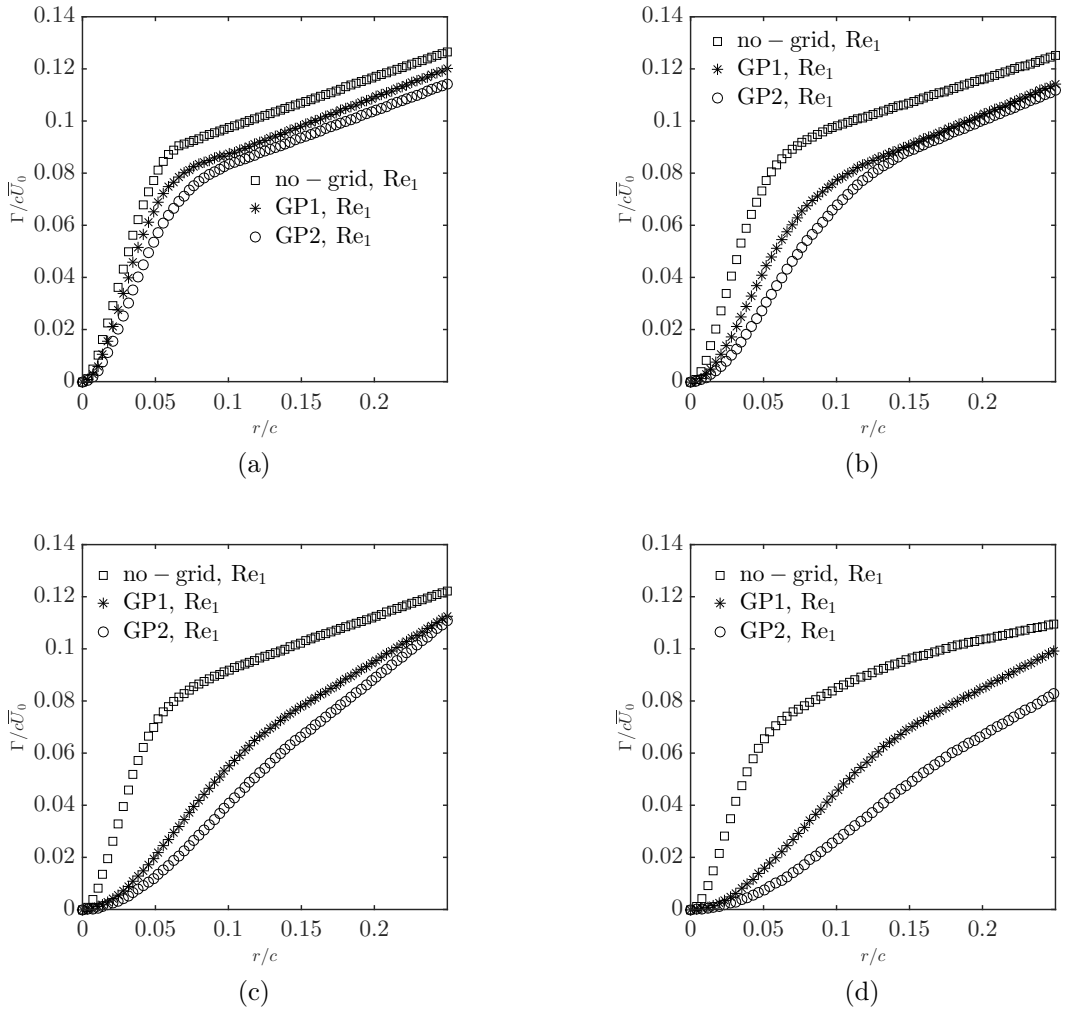

Figure 3.18 Normalized radial distribution of the vortex core circulation (a)x/c_w=1.25, (b)x/c_w=3.25, (c)x/c_w=6.25 and (d)x/c_w=7.75

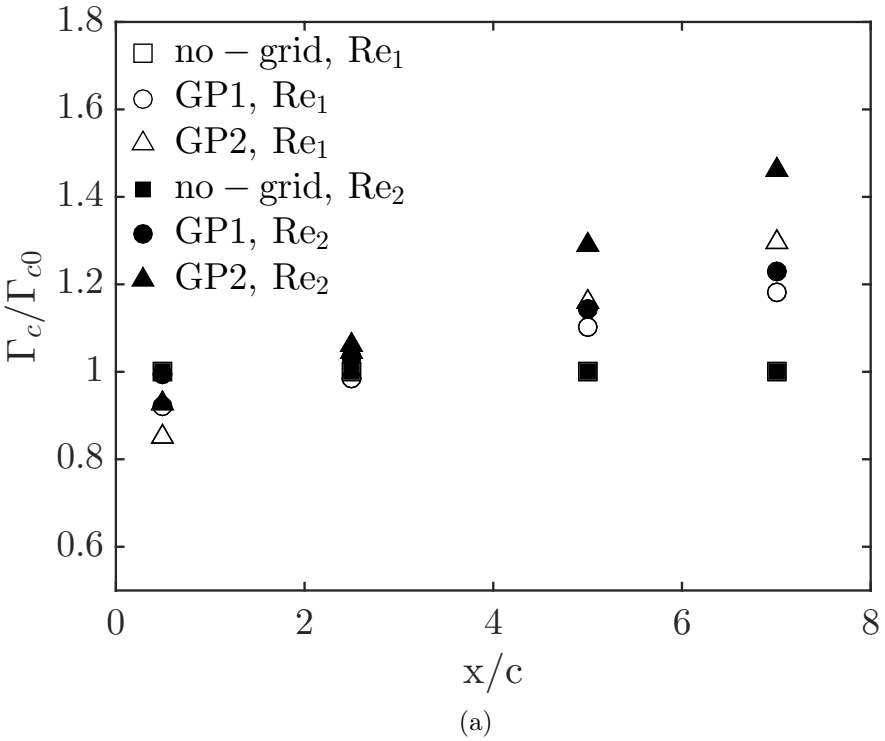

(a)

Figure 3.19 Streamwise development of the vortex core circulation

For all the reported cases, it was observed that the vortex core radii growth rate is essentially consistent with the core circulation increase. According to Saffman [46], the vortex core radius at which the maximum of circumferential velocity is reached could be expressed as:

$$r_m \sim \left(\frac{x}{c \times Re_c}\right)^{0.5} \tag{3.14}$$

For a Batchlor vortex, this radius could be given as:

$$r_m = 2.2418 \left(\frac{\nu x}{U_\infty}\right)^{0.5} \tag{3.15}$$

This form of vortex radius is valid with the condition of having a free stream velocity much more greater than the axial velocity deficit [107] with larger downstream distances. This equation could be used in fact to develop a similar correlation which implies the effect of FST. The dependence of the vortex radius on both Reynolds number and FST level, suggested that :

$$r_m = \left(\frac{L_g}{M}\right)^n r_m \tag{3.16}$$

$$r_m = \left(\frac{L_g}{M}\right)^n 2.2418 \left(\frac{\nu \times x}{U_\infty}\right)^{0.5} \tag{3.17}$$

L_g/M is proportional to the FST level, it represents the ratio between the grid distance from the wing leading edge and the grid mesh size. The previous equation suggested a reasonable fit for the normalized vortex core radii. The collapse with the experimental data became altered for $x/c_w = 7.75$ as the vortex is weak. For this study, the exponent n was estimated to be 0.8.

3.7.3 Vortex self similarity function

The effect of FST on the vortex core behavior can further be demonstrated using the radial distribution of the circulation, $\frac{\bar{\Gamma}_r}{\bar{\Gamma}_c}$ for the no-grid, GP1 and GP2 cases respectively. The self similarity of the inner vortex region is given by :

$$\frac{\bar{\Gamma}(r)}{\bar{\Gamma}_c} = A\eta^2 \quad \text{for} \quad \eta < 0.4 \tag{3.18}$$

$$\frac{\bar{\Gamma}(r)}{\bar{\Gamma}_c} = 1 + B\log(\eta) \quad \text{for} \quad 0.5 < \eta < 1.4 \tag{3.19}$$

where $A = 1.83$ and $B = 0.93$ For all cases, a reasonable collapse within $0 < \eta < 1.2$ was observed. The sixth-order polynomial curve suggested by [39] is given by :

$$\frac{\bar{\Gamma}(r)}{\bar{\Gamma}_c} = a_0\eta^2 + a_1\eta^4 + a_2\eta^6 \tag{3.20}$$

Radial profile of $\bar{\Gamma}_r/\bar{\Gamma}_c$ are plotted against $log(r/r_c)$ in Figure 3.20 at $x/c_w = 1.25$, 3.25, 6.25 and 7.75, with the emperical curve fitting suggested by [39]. For all reported positions, a reasonable collapse could be observed; the inner and buffer regions are well illustrated by the fitting suggested by [39] suggesting the self-similarity of the vortex. For both no-grid and grid cases GP1 and GP2, the behavior of the inner vortex region showed that $\bar{\Gamma}_r/\bar{\Gamma}_c \propto r^2$ for all the reported cases.

For reference, the exponents n, m, p, s depict the decay of $\bar{u_d}$, $\bar{v}_\theta$, r_c and k respectively. Not included in the discussion, Figure 3.21 represents the downstream decay of the peak of turbulent kinetic energy. This result confirms the above discussion, but was not included in the scientific paper.

3.7.4 Spectra Analysis

For a better assessment and understanding of the vortex meandering motion, frequency spectra measurements were conducted in the vortex core region, the shear layer region and an outer region in the main free stream. High (20 KHz) and low (200 Hz) frequency sampling were conducted in these three regions. With vortex meandering occurring at lower frequencies in comparison to the free stream turbulence frequencies, the presence of different levels of energy was not evident to be associated with a particular event concerning the vortex meandering motion, due to the strong dependence on the instantaneous velocity field data [91]. The the hot-wire signal contained a combined information from different vortex regions(vortex core, shear layer, free stream) as reported by Bailey [33]. A more pronounced effect was obtained with grid cases as the meandering amplitudes increased. Results are presented in Appendix A3.

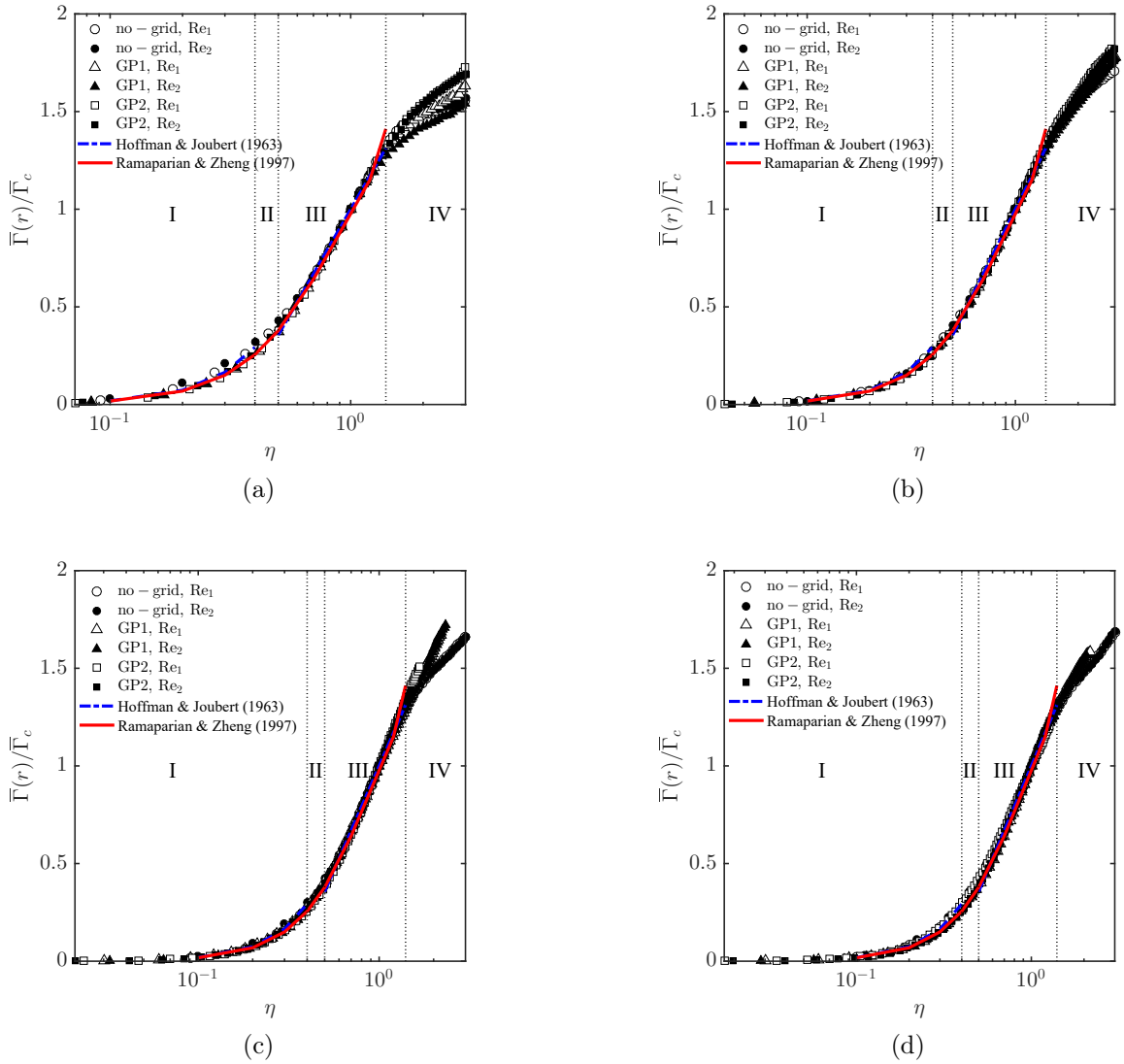

Figure 3.20 Self-similar profiles of the vortex core circulation (a)x/c_w = 1.25, (b)x/c_w = 3.25, (c)x/c_w = 6.25 and (d)x/c_w = 7.75

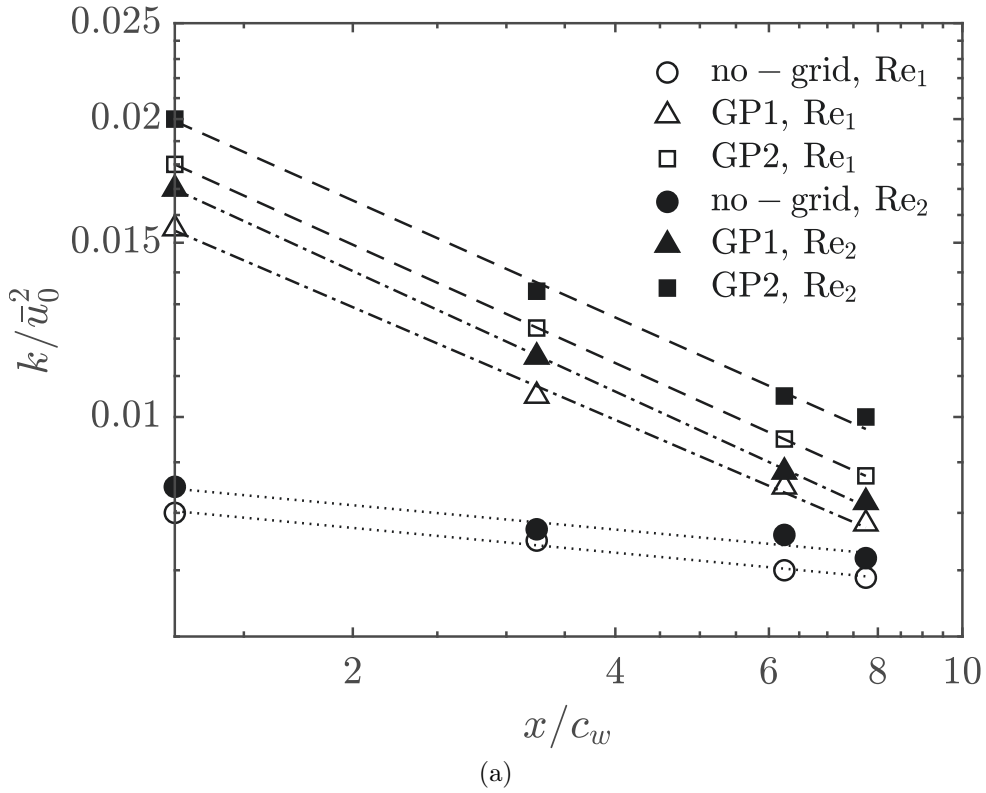

(a)

Figure 3.21 Streamwise development turbulent kinetic energy peak

Table 3.2 Summary of the power law coefficients for the fitting curves

	Re_1				Re_2			
	n	m	p	s	n	m	p	s
no-grid	-0.18	-0.005	0.006	-0.08	-0.19	-0.004	0.004	-0.08
GP1	-0.52	-0.55	0.49	-0.48	-0.48	-0.51	0.48	-0.50
GP2	-0.61	-0.60	0.62	-0.59	-0.59	-0.58	0.60	-0.59

CHAPTER 4

POD Analysis of a Wing-Tip Vortex Meandering in a Grid Generated Turbulent Flow

4.1 Introduction

Vortex meandering is a low frequency motion of the vortex core. This movement is characterized by a side-by-side drift of the vortex core about an average location, at frequencies much lower than those associated with turbulent motion ([33, 76, 78, 80]). Corsiglia et al. [78] suggested that vortex meandering is induced by wind tunnel background turbulence. Green and Acosta [42] and Bandyopadhyay et al. [96] proposed that meandering could result from the ejection of high vorticity fluid packets outside the vortex core. Rokhsaz et al. [108] and Bailey and Tavoularis [33] proposed that meandering mechanism consisted of velocity variations at other points in the flowfield, which induces displacements of the vortex core. Some authors attempted to quantify vortex meandering using different techniques. In fact, Devenport et al. [76] and Bailey and Tavoularis [33] developed analytical techniques to correct single-point flow field measurements and remove the meandering effect in order to recover the true velocity field of the wing-tip vortex. Heyes et al. [80] developed a more robust technique to correct for vortex meandering using particle image velocimetry (PIV) data. This method consists of re-aligning the vortex velocity fields such that the instantaneous vortex positions collocate with the mean vortex center position, directly removing the effect of meandering while retaining the true random fluctuations of the velocity field within the vortex core. Edstrand et al. [109] performed PIV measurements on a NACA0012 wake and used a similar method of Heyes et al. [80]. They removed the meandering induced turbulence from the measured velocity field and then recovered the coherent meandering motion using proper orthogonal decomposition (POD). The authors reported that high energy structures exhibited a helical mode corresponding to a wave number of $|m| = 1$. They observed that this mode depicted two-lobes beyond $x/c = 1.5$.

Heyes et al. [80] investigated the meandering of a wing-tip vortex under the effect of FST, they used two grids with a mesh size of 12.7 mm and 7.0 mm generating a free stream turbulence ranging between 1% and 5%. They observed a low level of turbulence in the vortex core. Baily and Tavoularis [33] performed hot-wire anemometry to quantify wing-

tip vortex dynamics as it evolved in a grid-generated turbulence field. They used two grids with a mesh size of 25.4 mm and 50.8 mm which correspond to a free stream turbulence level of 2.5% and 5%, respectively with a Reynolds number of $Re = 2.9 \times 10^4$. It was shown that the vortex circumferential velocity peak decay rate increased with increased FST, later confirmed by Ahmadi-Baloutaki et al. [81], but its radial position remained unaffected downstream in the wake. Meandering was observed to affect greatly the axial and circumferential velocities. Beresh et al. [93] conducted PIV measurements on a trailing vortex in the near wake. They observed that meandering amplitude increased with the downstream distance and decreased with the vortex strength in agreement with Heyes et al. [80]. A large turbulent kinetic energy peak was observed in the vortex core, which seemed to be meandering-induced according to the authors and was directly removed using the correction technique of [80]. More recently, Ghimire and Bailey [83] performed stereoscopic particle image velocimetry (SPIV) measurements to investigate the vortex decay in a grid-generated turbulent flow at $Re_c = 1.2 \times 10^4$ and two FST levels of 2.5% and 5%. The authors observed that increasing FST increased the rate of decay of the vortex peak of the circumferential velocity, whereas the rate of increase of the core radius remained unchanged. They also performed time-resolved PIV on a NACA0012 wing in a water tunnel with the same FST levels at $Re = 1.7 \times 10^4$ [84]. They observed a vortex decay with increasing FST and vortex stripping was also observed when the vortex was under FST effect, which suggested an ejection of the core fluid into the free stream. Bailey et al. [48] revisited their earlier wind tunnel measurements data combined with the experimental results of Ghimire and Bailey [83] and [84]. The authors reported that meandering amplitude scaled with FST and vortex core radius. They evaluated the vortex turnover time, defined as the product of the core circulation with the peak circumferential velocity. According to the authors, the vortex turnover time scaled with FST in agreement with Van-Jaarsveld et al. [82], however, meandering amplitude was insensitive to changes in the integral length and time scales of the turbulence. It has been documented that meandering is mainly dependent on the flow boundary conditions and has been adressed experimentally enough, however, its understanding remains a subject of research requiring further investigations. FST was found to increase meandering amplitudes, however, a complete assessment of the different mechanisms involved in this process were not evidently explained.

To advance the understanding of the wing-tip vortex meandering, the effect of FST on the roll-up process and the downstream development of a wing-tip vortex are addressed in this work, through measurements with Stereoscopic PIV in the near and mid-wake regions ($0.5 \leqslant x/c \leqslant 7$) at a Reynolds number of $Re = 2 \times 10^5$. Proper Orthogonal decomposition

was performed on the instantaneous velocity field data to extract the most energetic modes of the vortex structure. The meandering correction technique of Heyes et al. [80] was used to eliminate the meandering-induced turbulence from the the acquired velocity fields.

4.2 Proper Orthogonal Decomposition Analysis

In order to analyze the meandering motion of the vortex core, triple decomposition was applied to analyze the coherent structures of the vortex using the method of Reynolds and Hussain [110]. The effect of meandering on the measurements accuracy can be corrected using the method of Heyes et al. [80], where each instantaneous SPIV frame is shifted to the mean vortex center position, then the new velocity field is calculated. For each instantaneous velocity field, the vector $\boldsymbol{u}(x, t_k)$ can be written as [25, 109]:

$$\boldsymbol{u}(\boldsymbol{x}, t_k) = \bar{\boldsymbol{u}}(\boldsymbol{x}) + \hat{\boldsymbol{u}}(\boldsymbol{x}, t_k) + \boldsymbol{u'}(\boldsymbol{x}, t_k). \tag{4.1}$$

To extract the most energetic modes of the turbulent fluctuation of the vortex meandering, the triple decomposition technique is applied. A rich literature could be explored for the application of the triple decomposition in fluid mechanics and turbulent flows [111, 112]. Snaptshot Proper Orthoghonal Decomposition (SPOD) technique is applied when the number of samples (instantaneous velocity fields) is largely smaller than the number of the velocity vectors [25]. In the present study study, $N = 2000$ instantaneous velocity fields were captured, and each frame contained about 10^5 vectors. note that the SPOD technique required lower calculation in comparaison with the conventional POD technique [112]. The coherent vector field is then decomposed in a spatial function as:

$$\tilde{\boldsymbol{u}}(\boldsymbol{x}, t_k) = \sum_{k=1}^{N} a^k(t)\boldsymbol{\Phi}^k(\boldsymbol{x}). \tag{4.2}$$

where a^k are temporal coefficients.

To resolve the SPOD eigenvalue problem, each coherent velocity field was formulated as:

$$\mathsf{C}\boldsymbol{A}^k = \lambda^k \boldsymbol{A}^k, \tag{4.3}$$

where $\boldsymbol{C}$ is the co-variance matrix composed of coherent velocities snapshots S_w and S_v, for the coherent velocities $\tilde{v}$ and $\tilde{w}$, respectively [25].

$$\mathbf{\Phi}^k(\boldsymbol{x}) = \frac{\boldsymbol{\phi}^k(\boldsymbol{x})}{||\boldsymbol{\phi}^k(\boldsymbol{x})||}. \tag{4.4}$$

where λ^k and $\boldsymbol{A}^k$ are the eigenvalues and eigen vectors of the autocovariance matrix C, respectively. As C is symmetric and positive semi-definite, all the eigenvalues are real and non-negative and usually sorted in a descending order that relates to the decreasing turbulent kinetic energy, TKE, of the corresponding modes

$$\lambda^1 > \lambda^2 > ... > \lambda^N = 0. \tag{4.5}$$

The scalar modes $\boldsymbol{\phi}_w^k(\boldsymbol{x})$ and $\boldsymbol{\phi}_v^k(\boldsymbol{x})$, which respectively correspond to the coherent velocities $\tilde{w}$ and $\tilde{v}$, are obtained by the projections

$$\boldsymbol{\phi}_w^k(\boldsymbol{x}) = \mathsf{S}_w^T \boldsymbol{A}^k, \tag{4.6}$$

$$\boldsymbol{\phi}_v^k(\boldsymbol{x}) = \mathsf{S}_v^T \boldsymbol{A}^k. \tag{4.7}$$

The time coefficients are determined by projecting the coherent velocity field onto the scalar modes

$$a^k(t) = \mathsf{S}_w \mathbf{\Phi}_w^k(\boldsymbol{x}) + \mathsf{S}_v \mathbf{\Phi}_v^k(\boldsymbol{x}). \tag{4.8}$$

The main advantage of the POD approach is the ability to give the best approximation of the flow in an energetic sense. In that, the total turbulent kinetic energy (TKE) of the flow is given by the sum of the eigenvalues

$$\boldsymbol{E} = \sum_{k=1}^{N} \lambda^k. \tag{4.9}$$

A TKE percentage, based upon the scalar mode specific eigenvalue, can be determined to quantify the energy contribution of each mode to the total TKE

$$\boldsymbol{E}^k(\%) = \frac{\lambda^k}{\boldsymbol{E}} \tag{4.10}$$

4.3 Results and discussion

4.3.1 Vortex Meandering

The vortex meandering was characterized by analyzing the instantaneous vortex center position for each of the SPIV frames. To this end, in order to identify the instantaneous vortex center position, several techniques were reported in the literature. Most of these methods were based on the divergence of the velocity field [80, 93, 113, 114].

The standard deviations of the in-plane vortex center positions were defined as the meandering amplitudes, namely σ_z and σ_y, in both z and y directions, respectively. The scatter of the instantaneous vortex center positions of the no-grid case at $x/c_w = 1.25$ exhibited a nearly symmetrical distribution around the mean vortex position with no particularly preferred direction. At $x/c_w = 6.25$, the meandering amplitudes of the vortex positions scatter was found to increase with the dispersion pattern being symmetrical with respect to the mean vortex center position (as observed at $x/c_w = 1.25$). With FST, the scatter of the instantaneous vortex center positions covered a larger area around the position of the mean vortex center compared to the no-grid case. As the vortex was convected to $x/c_w = 6.25$, the area covered by the scatter of the instantaneous vortex center positions was shown to be larger than those at $x/c_w = 1.25$, particularly for GP1 and GP2. The streamwise development of the z and y meandering amplitudes, σ_z and σ_y, is summarized in Figure 4.1. For the no-grid case, the meandering amplitudes were found to slightly grow with increased streamwise distance, consistent with the observations reported in [33, 76, 93]. With FST and at $x/c_w = 1.25$, the meandering amplitudes, in both z and y directions, were found to be nearly 4 and 8 times higher than those of the no-grid case. Note that the meandering amplitudes, σ_z and σ_y, were found to rapidly increase with increased downstream distances (roughly an order of magnitude higher) with the effect being more pronounced under the case GP2. It is interesting to note that the meandering amplitudes for all the cases studied seem to decrease with increased Re number at all streamwise positions suggesting a lower meandering-induced turbulence within the vortex core and subsequently a lesser diffuse vortex.

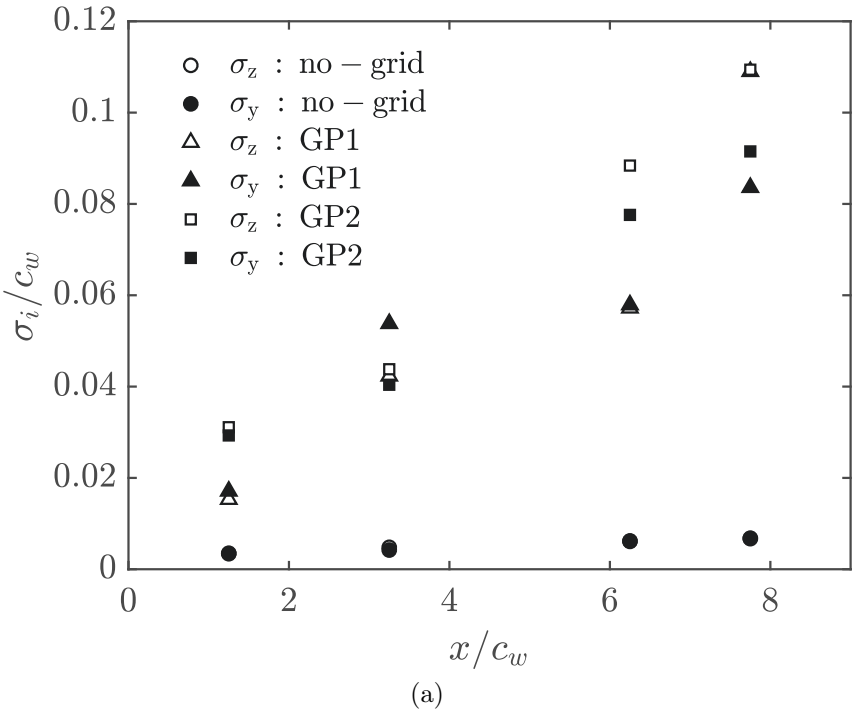

(a)

Figure 4.1 Vortex meandering amplitudes, σ_z and σ_y at different downstream positions

The vortex center positions may be fitted fairly well by a probability density function (p.d.f.) where the meandering amplitudes can be effectively represented by its corresponding standard deviations σ_z and σ_y in the z and y directions, respectively [25, 33, 76, 109]. Figure 4.2 displayes the p.d.f. profiles of the instantaneous vortex centres in z and y for all the cases studied at $x/c_w = 1.25$ and $x/c_w = 6.25$, respectively. The p.d.f.s were fitted with normal Gaussian profiles. For the no-grid case, Figure 4.2 showes a symmetric distribution of the p.d.f. profiles for both z and y directions around the mean vortex center position. With FST, p.d.f. profiles exhibited similar distribution to that of the GP1 and GP2 cases at the downstream locations $x/c_w = 1.25$ and $x/c_w = 6.75$. The symmetry observed in the p.d.f.s of the instantaneous vortex center positions is fairly consistent with the symmetry in the scatter of the vortex center positions. Short excursions of the vortex center positions were mostly clustered around the mean vortex center for both GP1 and GP2 cases. Their occurrences were characterized with high probabilities and were associated with the occurrences clustered around the mean vortex center position, whereas large excursions of the vortex center positions were characterized with low probabilities, with the effect being more pronounced under GP2 case.

Contours of the joint probability density function (j.p.d.f.) are represented in Figure 4.3a and 4.3d for the no-grid case, Figure 4.3b and 4.3e for the GP1 case and Figure 4.3c and 4.3f for the GP2 case, respectively. For the no-grid case, the j.p.d.f. distribution showed concentric iso-contours around the location of the mean vortex center. Contours of similar levels were seen to cover a larger area around the mean vortex center as the vortex was convected from $x/c_w = 1.25$ to $x/c_w = 6.25$. This suggests that the large excursions of the vortex center around its mean location were characterized with higher probabilities as the the vortex evolved to $x/c_w = 6.25$. With FST and at $x/c_w = 1.25$, iso-contours of the j.p.d.f. distributions of GP1 and GP2 cases depicted a nearly axisymmetric shape around the mean vortex center position. Similar contour levels were found to cover larger areas around the mean vortex center compared to the no-grid case indicating an increased vortex meandering with increased FST. Further downstream and at $x/c_w = 6.25$, iso-contours of the j.p.d.f. distributions for GP1 and GP2 cases occupied a rather larger areas around the mean vortex center compared to the no-grid case.

As the vortex is subjected to hight FST intensities, its increased meandering causes additional turbulence within the core region [48, 76, 93, 115]. In order to separate the contributions of both coherent and random turbulence to the mean and turbulent fields of the vortex, the correction method suggested by Heyes et al. [80] was applied to the instantaneous vortex velocity fields.

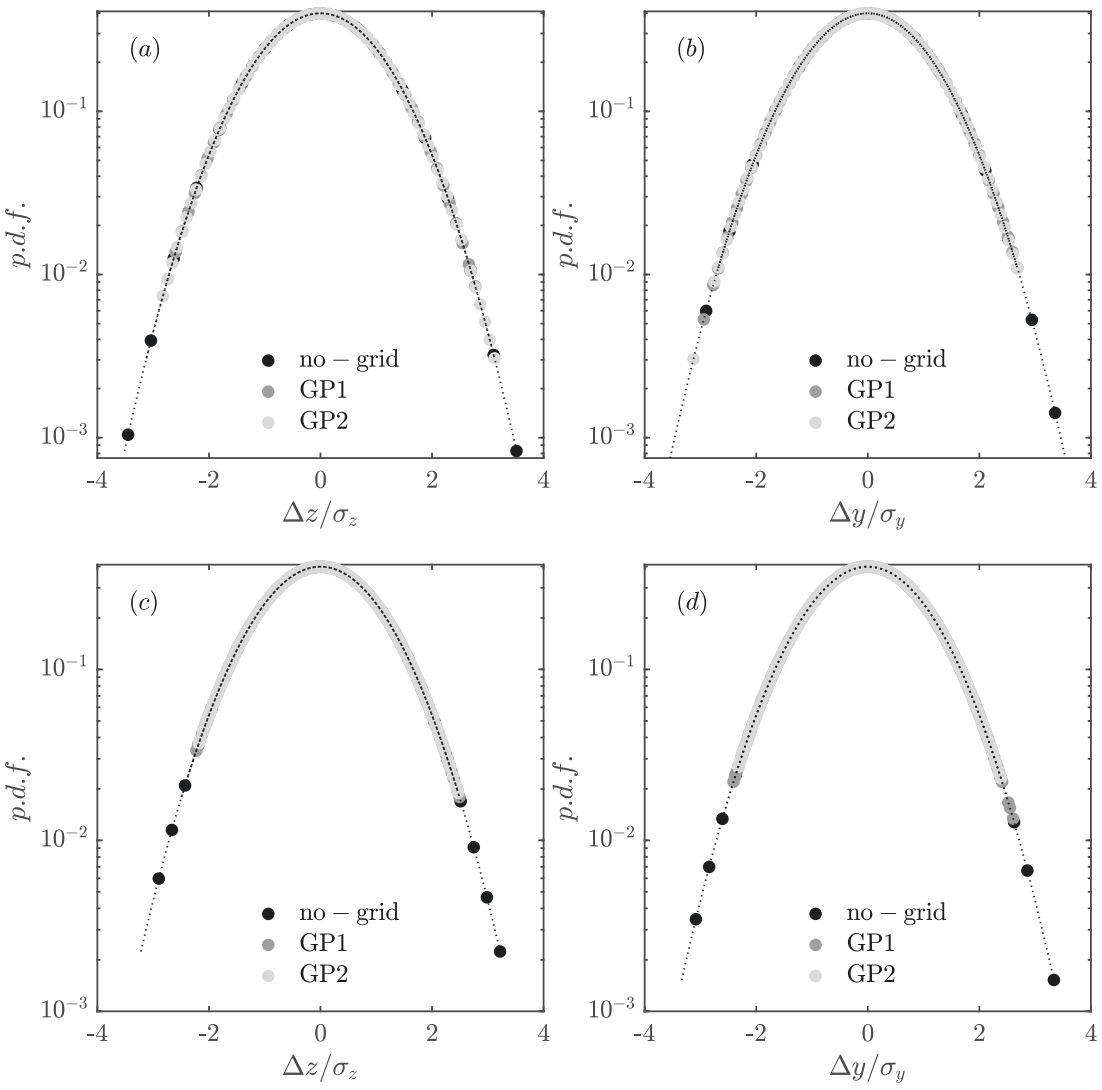

Figure 4.2 Contours of the p.d.f. distribution of the instantaneous vortex center positions in the y and z directions at $x/c_w = 1.25$ and 6.25. (a)(c): z direction, (b)(d) y direction

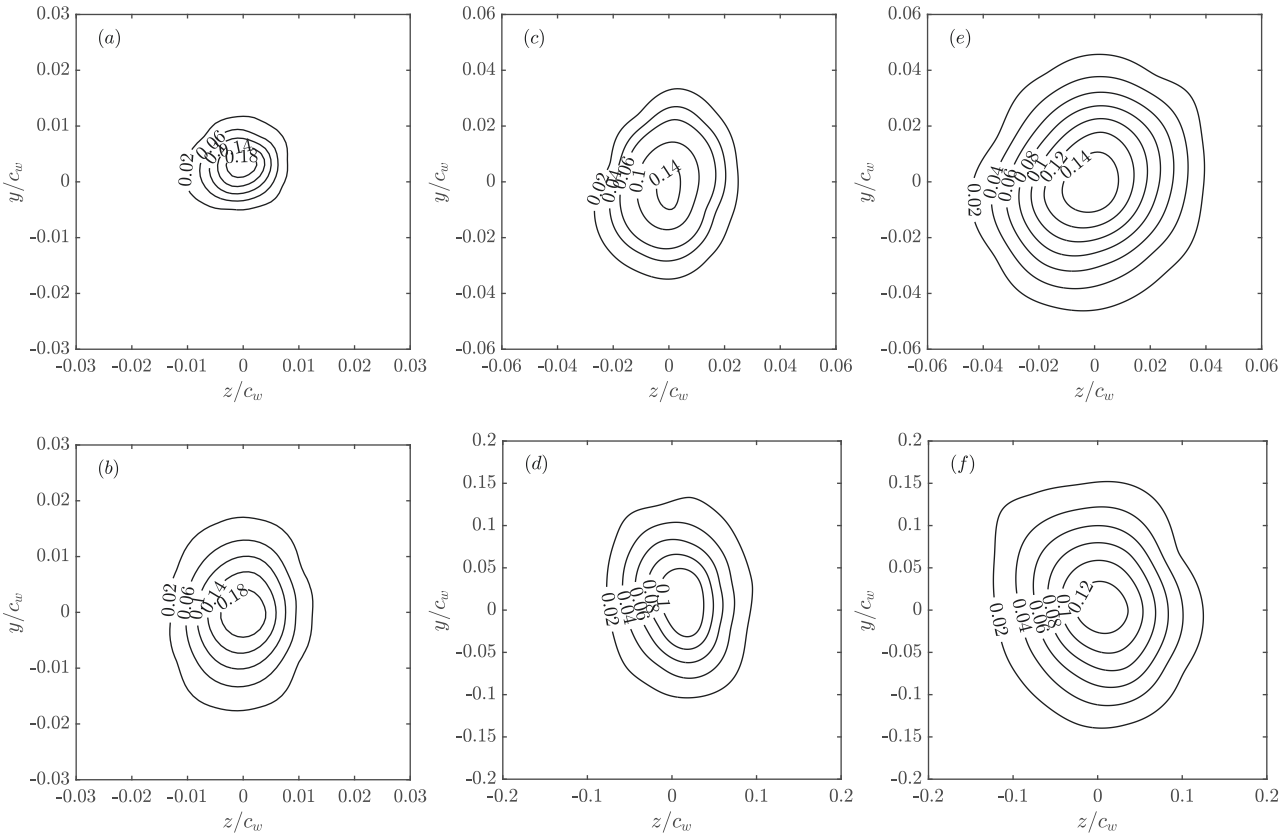

Figure 4.3 Contours of the Gaussian j.p.d.f. distribution of the instantaneous vortex center positions evaluated at $x/c_w = 1.25$ and 6.25. (a)(b): no-grid case, (c)(d): GP1 case and (e)(f): GP2 case.

Profiles of the uncorrected, $\bar{v}_\theta/\bar{u}_0$, and corrected, $\bar{\hat{v}}_\theta/\bar{u}_0$, circumferential velocities of the no-grid, GP1 and GP2 cases were plotted in Figure 3.15 at the selected downstream positions $x/c_w = 1.25$ and $x/c_w = 6.25$, respectively. For the no-grid case, a small increase in the peak value of the azimuthal velocity was obtained with the application of meandering correction (nearly 2%) however no significant effect was observed on the vortex radius. It is believed that, for the no-grid case, the little effect of the meandering correction on the mean circumferential velocity is probably attributed to the high turbulent fluctuations within the vortex core compared to the meandering-induced turbulence, as suggested in [93, 115] and [25]. With turbulence, the peak value of the corrected circumferential velocity, $\bar{\hat{v}}_\theta/\bar{u}_0$, was found to be 8% and 15% higher than the peak values of the non-corrected circumferential velocity $\bar{v}_\theta/\bar{u}_0$ for both GP1 and GP2, respectively. This increase was associated with nearly 20% and 27% decrease in the vortex radii of GP1 and GP2 cases, respectively.

Modal analysis of the mechanism of vortex decay

To further elucidate the features of the coherent and most energetic structures responsible for the vortex diffusion under grid turbulence, the snapshot proper orthogonal decomposition (SPOD) was performed on the velocity field data. Figure 4.5a and Figure 4.5d represents the first vorticity contours of the leading POD mode for the natural vortex case, Figure 4.5b and Figure 4.5e for case GP1, and figure 4.5c Figure 4.5ffor case GP2 at the measurement planes $x/c_w = 1.25$ and 6.25 respectively.

Figure 4.6a Figure 4.6d represent the second vorticity contours of the leading POD mode for the natural vortex case, Figure 4.6bFigure 4.6e for case GP1, and figure Figure 4.6c Figure 4.6ffor case GP2 at the measurement planes $x/c_w = 1.25$ and 6.25 respectively.

The first and second modes are the most dominant modes, which are paired helicaly. They are 90 degrees perpendicular and rotate orthogonally. For the no-grid case, the first mode depicted vorticity contours which are believed to be associated with the coherent wake shear layer as reported by [25]. Two nearly symmetrical regions with opposite signs could be seen around the vortex area with relatively high vorticity at $x/c_w = 1.25$. They were confined in a similar region size of about $0.02c_w$, which remained essentially the same as the vortex evolved downstream. At $x/c_w = 6.25$, the two regions observed a growth into a circular vortex dipole centered around the mean vortex center position, as illustrated in Figure 4.5a and Figure 4.5d. This dipole is consistent with the the helical displacement of the vortex with an azimuthal wavenumber $m = 1$, in agreement with the observations of [25, 109].

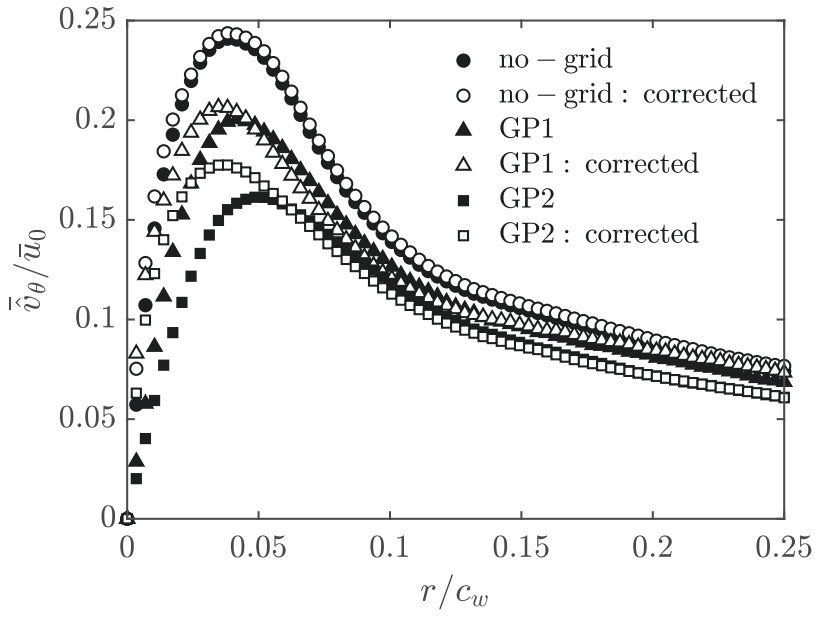

(a)

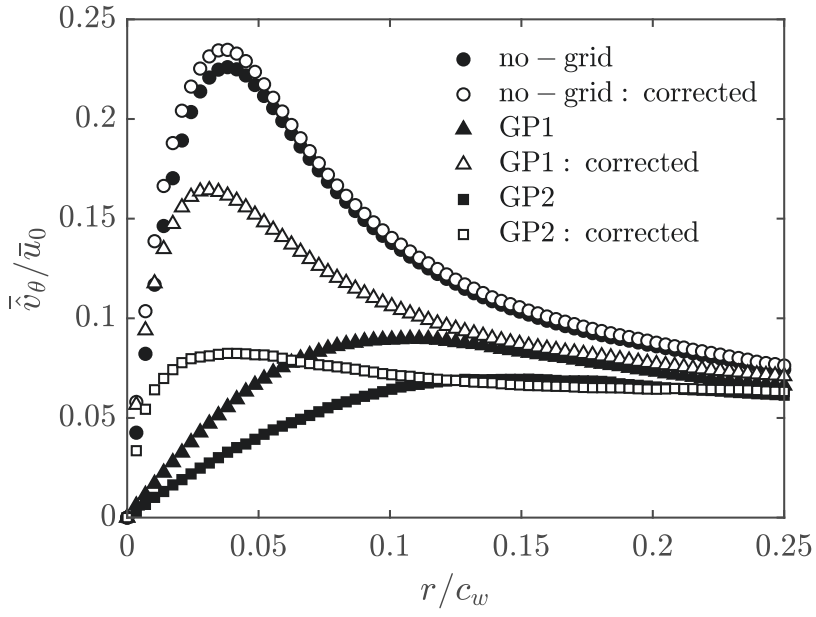

(b)

Figure 4.4 Corrected and uncorrected circumferential velocity profiles at $Re_{c_w} = 2 \times 10^5$ (a)$x/c_w = 1.25$ (b)$x/c_w 6.75$

The azimuthal symmetry of the vortex dipole is mainly associated with the global lateral displacement of the vortex where the decrease in one of the vortex doublet is compensated by an increase in the other, resulting in an overall helical displacement of the vortex core [116]. The second vorticity POD mode, depicted in Figure 4.6, exhibited a similar behavior to the first mode with the vortex dipoles being orthogonal to those of the first mode. It is believed that the first two modes are paired and orthogonally rotate together as the vortex evolves downstream; however, no conclusions on the direction of rotation can be drawn from figure 4.5 due to insufficient temporal resolution [25, 116]. The energies contained in the two leading modes were nearly similar but largely higher than the remaining POD modes, as indicated in the POD energy spectra of the first twenty modes shown in Figure 4.7. It is possible to associate the two dominant modes with the Kelvin wave of azimuthal wavenumber $m = 1$. The lower energy modes consisted of higher order azimuthal modes. The linear combination of the two dominant modes resulted in a relatively large fraction of the coherent TKE contained in the vortex core, as shown in figure 4.7. This portion of the energy is mainly used to displace the vortex which results in its meandering motion. In Figure 4.8, the meandering energy increased with increased downstream distances, in a similar manner observed in the streamwise evolution of the meandering amplitudes (Figure 4.1) [25]. For the grid cases, GP1 and GP2, the azimuthal symmetry of the helical structure was found to be disrupted as the two vortex doublet exhibited different shapes and largely asymmetric vorticity levels. At $x/c_w = 1.25$, the positive vorticity contours (colored in blue) were seen to be stretched similar to that observed in the scatter of the instantaneous vortex positions. The size and vorticity levels associated with the vortex doublet were larger than those recorded in the natural vortex case, indicating an increased meandering amplitudes of the turbulent vortex. As the vortex evolved downstream, the helical mode was seen to rotated at an azimuthal angle homologous without a preferred vortex meander direction, as displayed in Figure 4.5. In Figure 4.9, the streamwise growth of the meandering energy (associated with the dominant modes) corroborates results observed in Figure 3.16 as in the cases GP1 and GP2, a substantially higher energy is required to displace the vortex with larger meandering amplitudes. At very high meandering amplitudes, for instance in the case GP2, the vorticity leading modes showed that the dipole tended to dissipate into a more likely singular region consistent with the weakness of the vortex ($x/c_w = 6.25$). It is believed that the turbulent structures weakened the vorticity component of the vortex, which leads to a decrease of the momentum exchange between the vortex core and the spiral wake, in agreement with the conclusions on vorticity stripping by the coherent structures reported by Ghimire and Bailey [83].

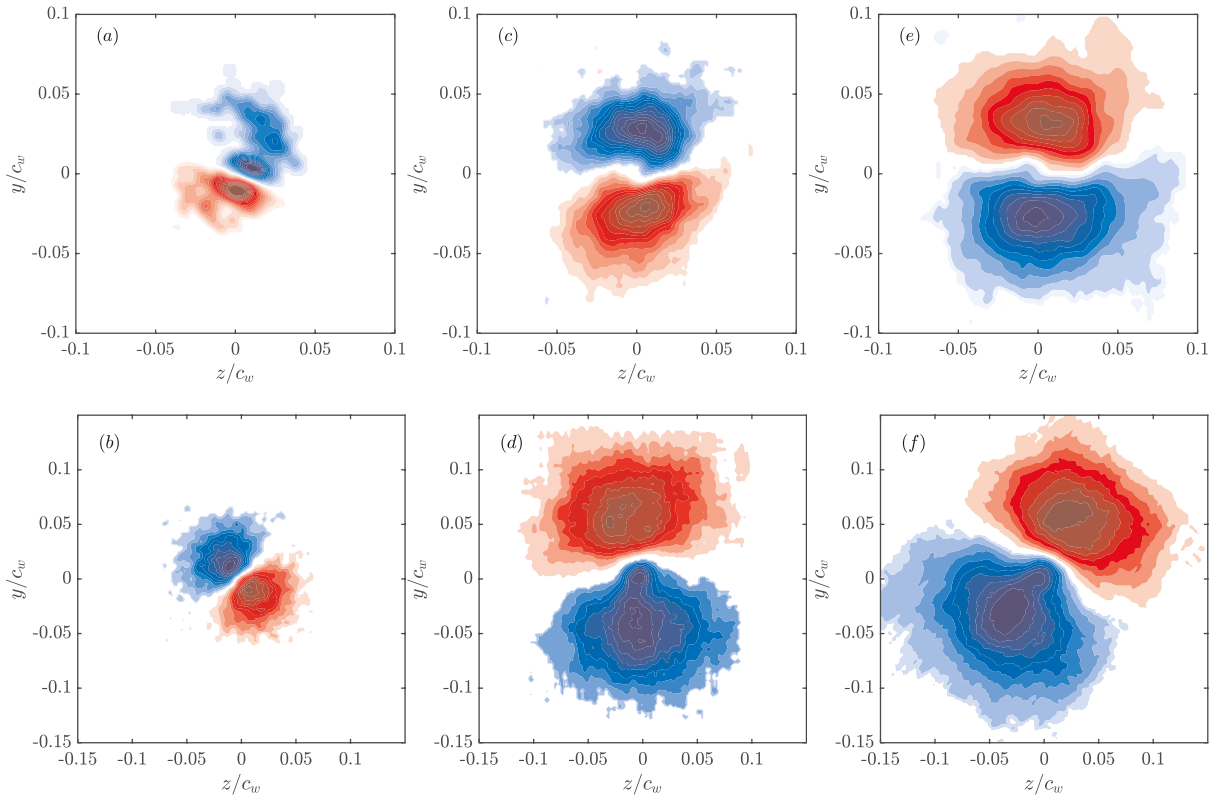

Figure 4.5 Axial vorticity contours of the first POD mode evaluated at x/c_w = 1.25 and 6.25. (a)(b):no-grid, (c)(d) GP1, (e)(f):GP2

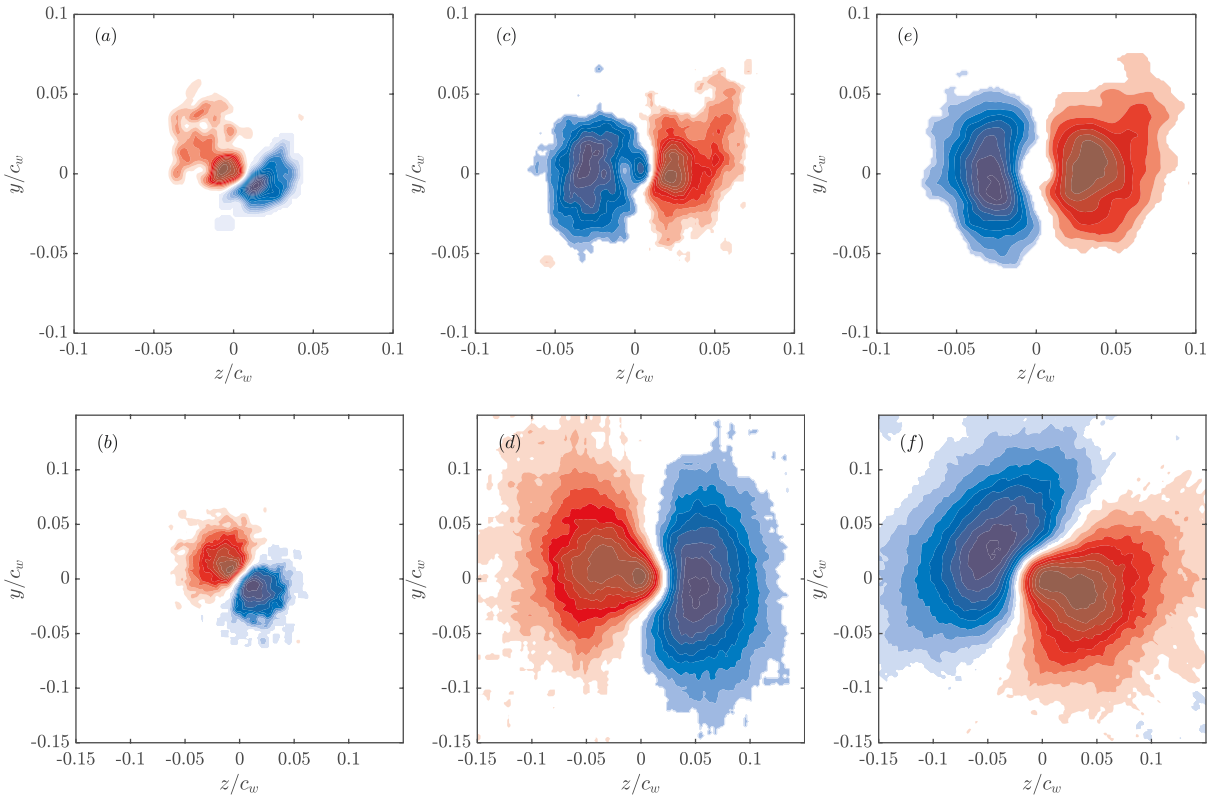

Figure 4.6 Axial vorticity contours of the second POD mode evaluated at $x/c_w = 1.25$ and 6.25. (a)(b):no-grid, (c)(d):GP1, (e)(f):GP2

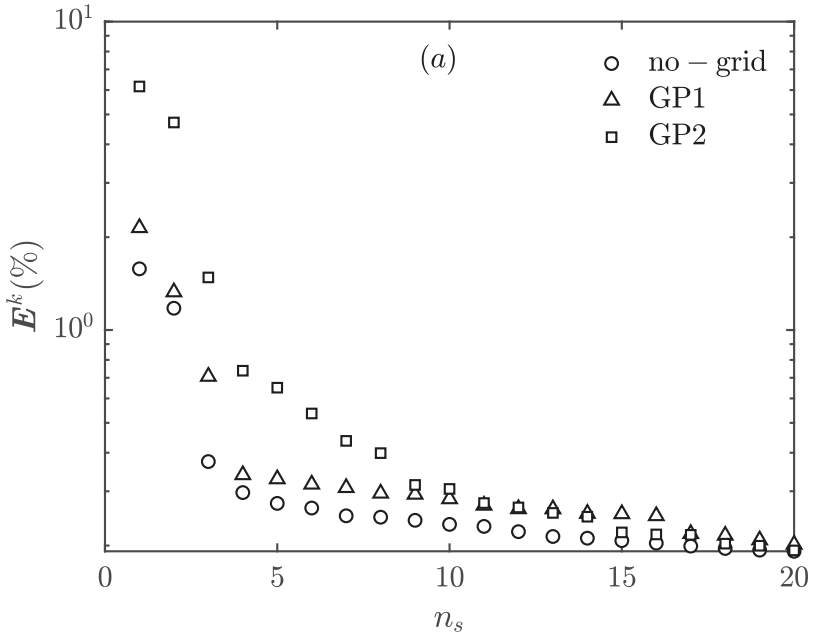

Figure 4.7 Energy spectra of the first twenty POD modes at $x/c_w = 1.25$

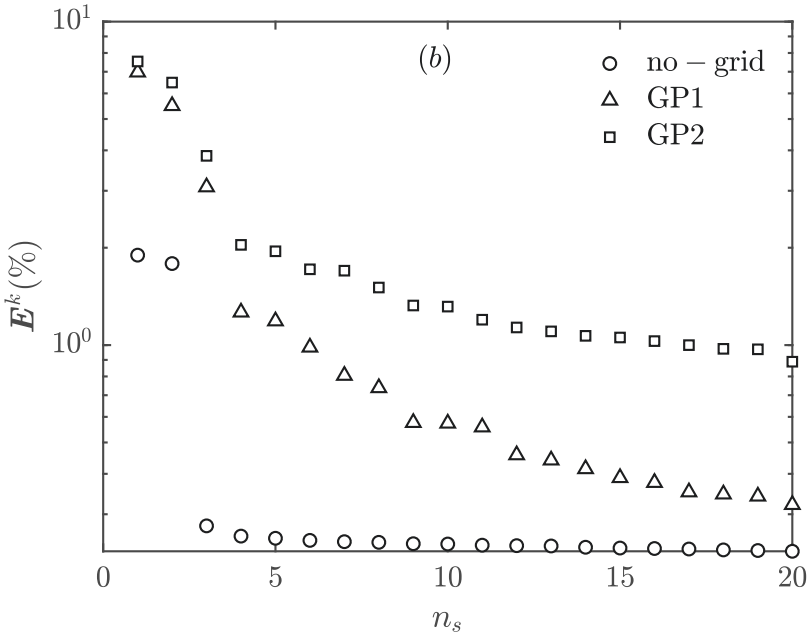

Figure 4.8 Energy spectra of the first twenty POD modes at $x/c_w = 6.25$

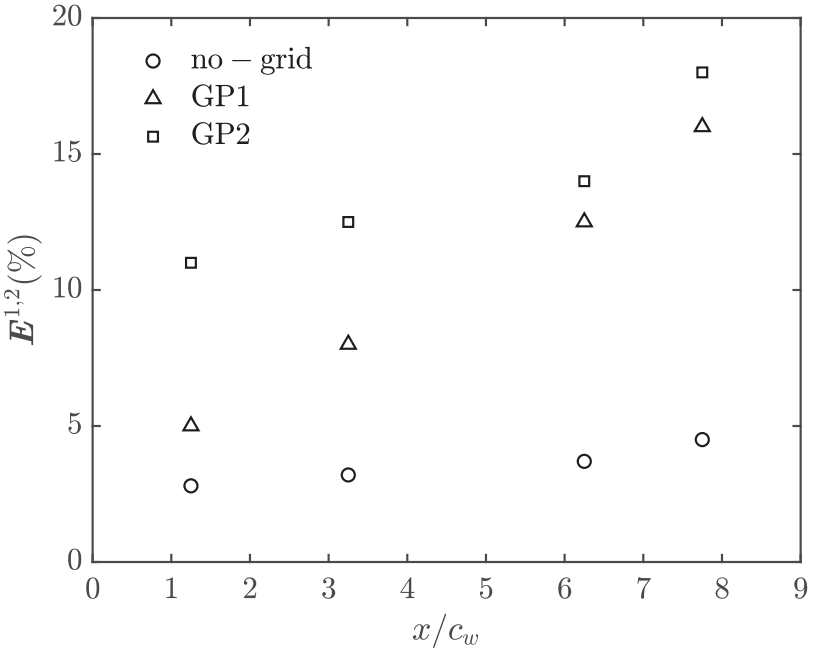

Figure 4.9 Energy content of the dominant helical mode (two first modes) as a function of streamwise distance

4.3.2 Mechanism of vortex diffusion: Enstrophy balance

A quantitative description of the physical mechanisms associated with the outward diffusion of the vortex core and the reduction of its strength can be obtained by examining the transport equation of the enstrophy, Ξ, defined as the trace of the time-averaged vorticity covariance, $\bar{\xi}_i\bar{\xi}_i$. Tennekes [88] and Balint *and al.* [117] derived the transport equation of the mean enstrophy from the momentum equation as [25]:

$$\begin{aligned}\frac{\partial}{\partial t}\left(\frac{1}{2}\Xi\right) = &\underbrace{-\bar{u}_j\frac{\partial}{\partial x_j}\left(\frac{1}{2}\Xi\right)}_{C^\Xi} - \underbrace{\frac{\partial}{\partial x_j}\left(\bar{\xi}_i\overline{\xi_i' u_j'}\right)}_{T^\Xi} + \underbrace{\overline{u_j'\xi_i'}\frac{\partial\bar{\xi}_i}{\partial x_j}}_{P^\Xi} \\ &\underbrace{+\bar{\xi}_i\overline{\xi_j' s_{ij}}}_{S^\Xi} + \underbrace{\nu\frac{\partial^2}{\partial x_j\partial x_j}\left(\frac{1}{2}\Xi\right)}_{\nu^\Xi} - \underbrace{\nu\frac{\partial\bar{\xi}_i}{\partial x_j}\frac{\partial\bar{\xi}_i}{\partial x_j}}_{\epsilon^\Xi}\end{aligned} \tag{4.11}$$

where $\bar{\xi}_i$ and ξ_i' are the components of the vorticity vector of the time-averaged and fluctuating fields respectively and are given by

$$\bar{\xi}_i = \epsilon_{ijk}\frac{\partial\bar{u}_k}{\partial x_j} \tag{4.12}$$

$$\xi_i' = \epsilon_{ijk}\frac{\partial u_k'}{\partial x_j} \tag{4.13}$$

where ϵ_{ijk} is the Levi-Civita symbol, and $\bar{u}_k$ and u_k' are the components of the time-averaged and the fluctuating velocity fields, respectively. Moreover, s_{ij} corresponds to the fluctuating strain rate.

Although not shown here, the spanwise and transverse components of the vorticity vector were found to be negligible compared to the axial component. Thus, the mean enstrophy can be reasonably approximated as only a function of the axial vorticity, $\Xi \approx \bar{\xi}_x\bar{\xi}_x$. Consequently, the different terms of the equation 4.11 can be written as

$$C^\Xi = -\bar{u}_z\frac{\partial}{\partial z}\left(\frac{1}{2}\Xi\right) - \bar{u}_y\frac{\partial}{\partial y}\left(\frac{1}{2}\Xi\right); \tag{4.14}$$

$$T^{\Xi} = -\frac{\partial}{\partial z}\left(\bar{\xi}_x\overline{\xi'_x u'_z}\right) - \frac{\partial}{\partial y}\left(\bar{\xi}_x\overline{\xi'_x u'_y}\right); \tag{4.15}$$

$$P^{\Xi} = \overline{u'_z\xi'_x}\frac{\partial\bar{\xi}_x}{\partial z} + \overline{u'_y\xi'_x}\frac{\partial\bar{\xi}_x}{\partial y}; \tag{4.16}$$

$$S^{\Xi} = \bar{\xi}_x\overline{\xi'_z s_{xz}} + \bar{\xi}_x\overline{\xi'_y s_{xy}}; \tag{4.17}$$

$$\nu^{\Xi} = \nu\left[\frac{\partial^2}{\partial z\partial z}\left(\frac{1}{2}\Xi\right) + \frac{\partial^2}{\partial y\partial y}\left(\frac{1}{2}\Xi\right)\right]; \tag{4.18}$$

and

$$\epsilon^{\Xi} = -\nu\left[\frac{\partial\bar{\xi}_x}{\partial z}\frac{\partial\bar{\xi}_x}{\partial z} + \frac{\partial\bar{\xi}_x}{\partial y}\frac{\partial\bar{\xi}_x}{\partial y}\right]. \tag{4.19}$$

where the term C^{Ξ} represents the advection of enstrophy by mean flow, T^{Ξ} is the transport of enstrophy by turbulent vorticity-velocity interactions, P^{Ξ} is the turbulence production term, S^{Ξ} corresponds to the production (or removal) of enstrophy caused by stretching (or squeezing) of fluctuating vorticity components by fluctuating strain rate, while ν^{Ξ} and ϵ^{Ξ} represent viscous diffusion and dissipation of enstrophy respectively.

Radial distributions of the dominant terms in the mean enstrophy transport equation are illustrated in Figure 4.10a, 4.10b and 4.10c for the no-grid, GP1 and GP2 cases, respectively, at the measurement plane $x/c_w = 1.25$ and $Re_c = 2\times10^5$. For the no-grid case, Figure 4.10a shows that the dominant terms in the transport equation are the convection term C^{Ξ} and the turbulent transport, T^{Ξ}, which mainly contributed to the generation of the mean enstrophy within the vortex core for the no-grid case. The transport of the mean enstrophy, which is a by-product of the vorticity created by the wing-tip vortex, was found to trigger other production terms within the vortex core region. In that, the transported vorticity was found to be stretched by the fluctuating strain rate resulting in a further production of enstrophy (P^{Ξ}). It can be inferred from Figure 4.10a that T^{Ξ}, S^{Ξ}, P^{Ξ} and ν^{Ξ} may be balanced with the advection due to the mean flow, C^{Ξ}, and the viscous dissipation, ϵ^{Ξ}. Consequently, the mechanism of turbulent production for the no-grid case was only limited to the vorticity stretching by fluctuating strain rate. Note that, outside the core region, all the terms asymptotically approach zero where the flow is nearly irrotational. With FST of 3% and at $X/c_w = 1.25$, the peak value of the turbulent transport term, T^{Ξ}, were found to decrease by nearly 30% compared to the no-grid case. This significant reduction in the turbulent transport may be attributed to the decrease in the mean vorticity caused by the diffusion of the vortex under the effect of FST. Additionally, the reduced mean vorticity caused the turbulent production term, P^{Ξ}, to be greatly reduced compared to the no-grid case. It can be surmised from Figure 4.10b

that the vorticity stretching caused the reduction of dissipation of the mean enstrophy as it appears to be the dominant term in the transport equation within the vortex core region. Further reduction in both convection and turbulent transport terms was depicted in Figure 4.10c when FST increased from 3% to 6%. This reduction was accompanied with nearly 20% decrease in the peak value of the stretching term, S^{Ξ}. It is noteworthy that the radial position of the peak values of these terms were seen to move further away from the vortex center indicating an increased outward transport of enstrophy under the effect of FST.

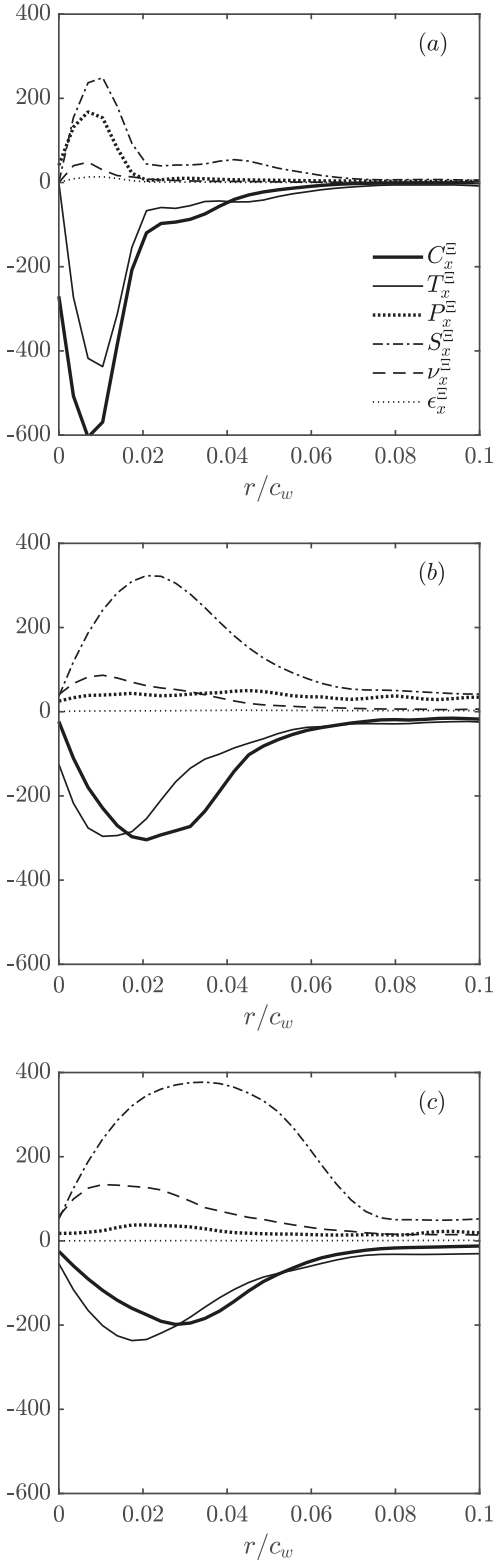

Figure 4.10 Radial distribution of the mean enstrophy budget at $X/c_w = 1.25$. (a):no-grid, (b):GP1 and (c):GP2

4.4 Further discussion

The contours of the Gaussian j.p.d.f. distribution are represented in Figure 4.12. The meandering amplitude is normalized by the wing cord length c_w instead of σ. A symmetric distribution could be observed for the no-grid, GP1 and GP2 cases for both z and y directions centered around the averaged vortex center, consistant with the observations made in Figure 4.12. A high displacement is observed for GP2 confirming the increased meandering amplitude. In addition to the enstrophy budget presented in Figure 4.11, contours of each term of the enstropy equation are represented in Figure 4.13, Figure 4.14, Figure 4.15, Figure 4.16 and Figure 4.17 for $x/c_w = 1.25$, for the terms, C^{Ξ}, T^{Ξ}, P^{Ξ}, S^{Ξ} and ν^{Ξ}, respectively.

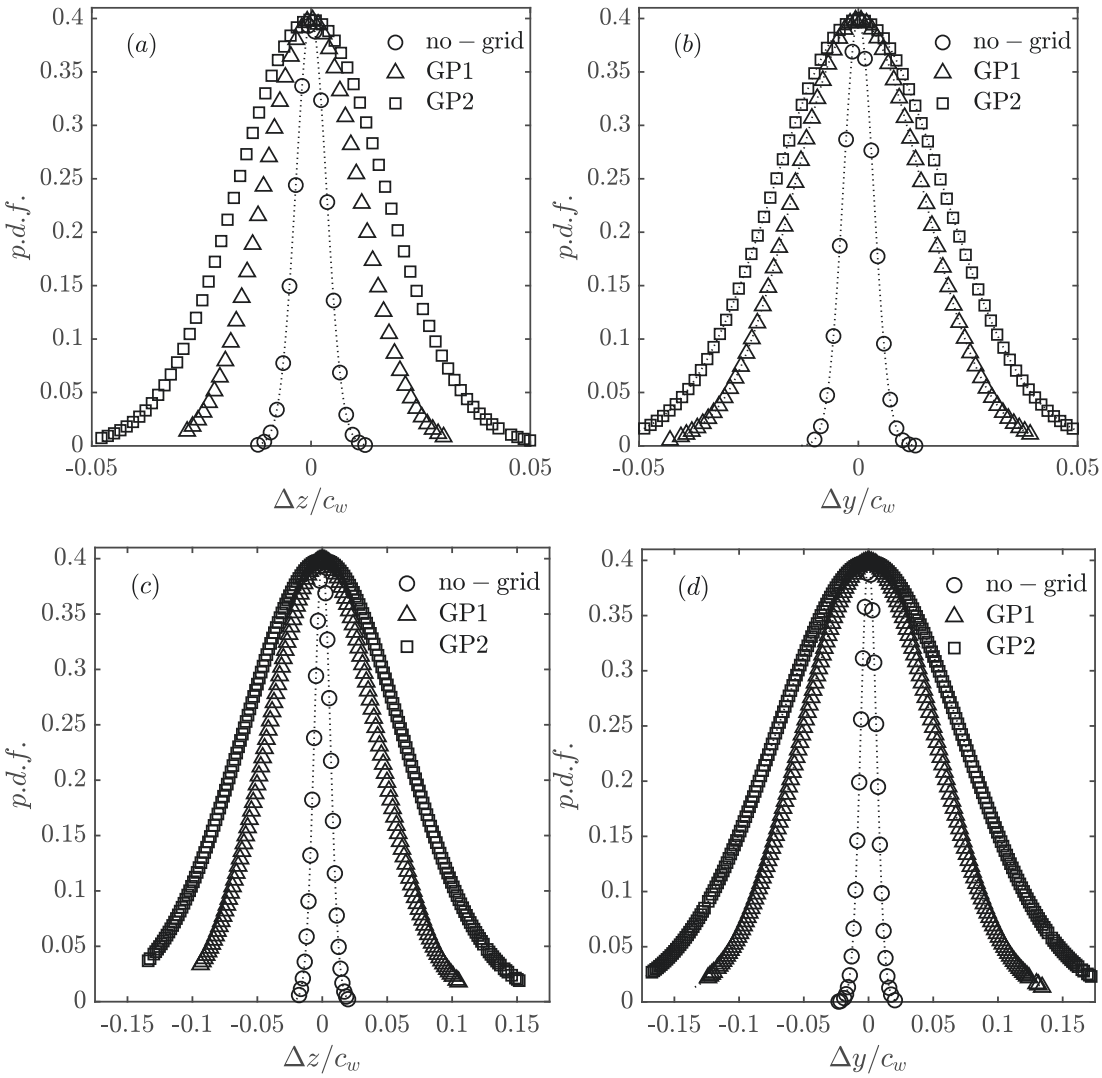

Figure 4.12 Contours of the Gaussian j.p.d.f. distribution of the instantaneous vortex center positions evaluated at $x/c_w = 1.25$ and 6.25

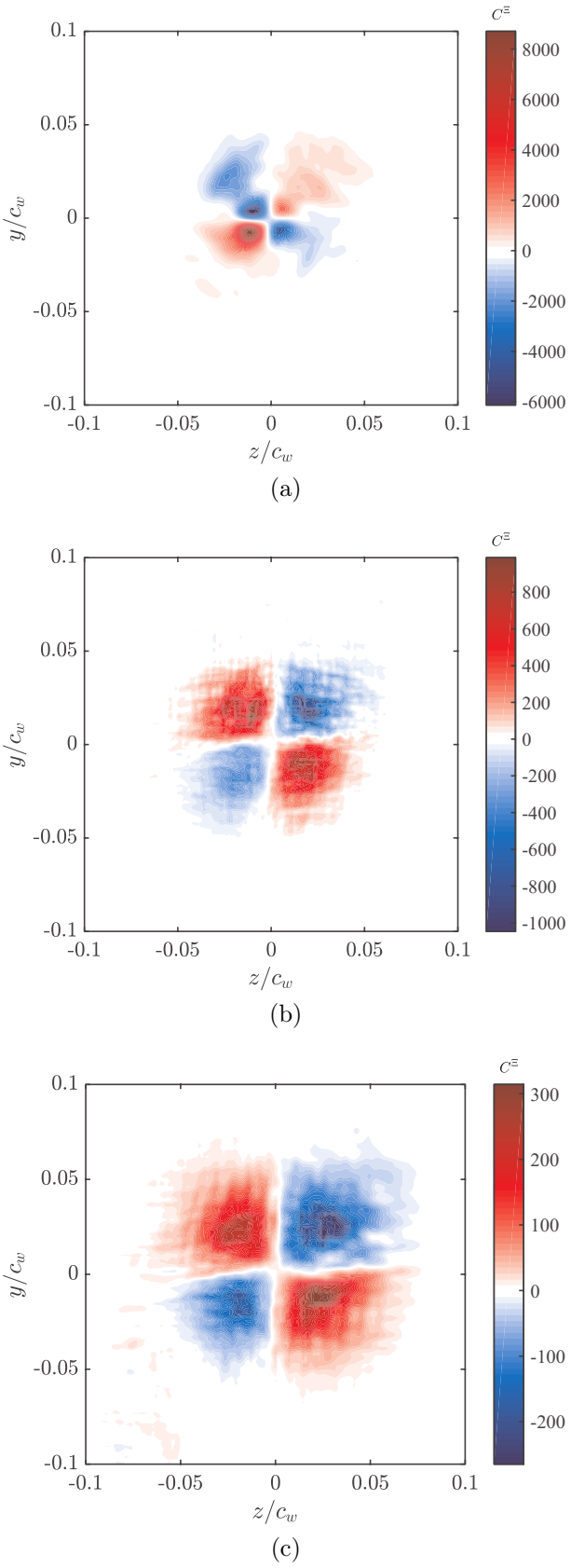

Figure 4.13 Enstrophy equation term $\boldsymbol{C}^{\boldsymbol{\Xi}}$ contours (a) no-grid (b) GP1 and (c) GP2

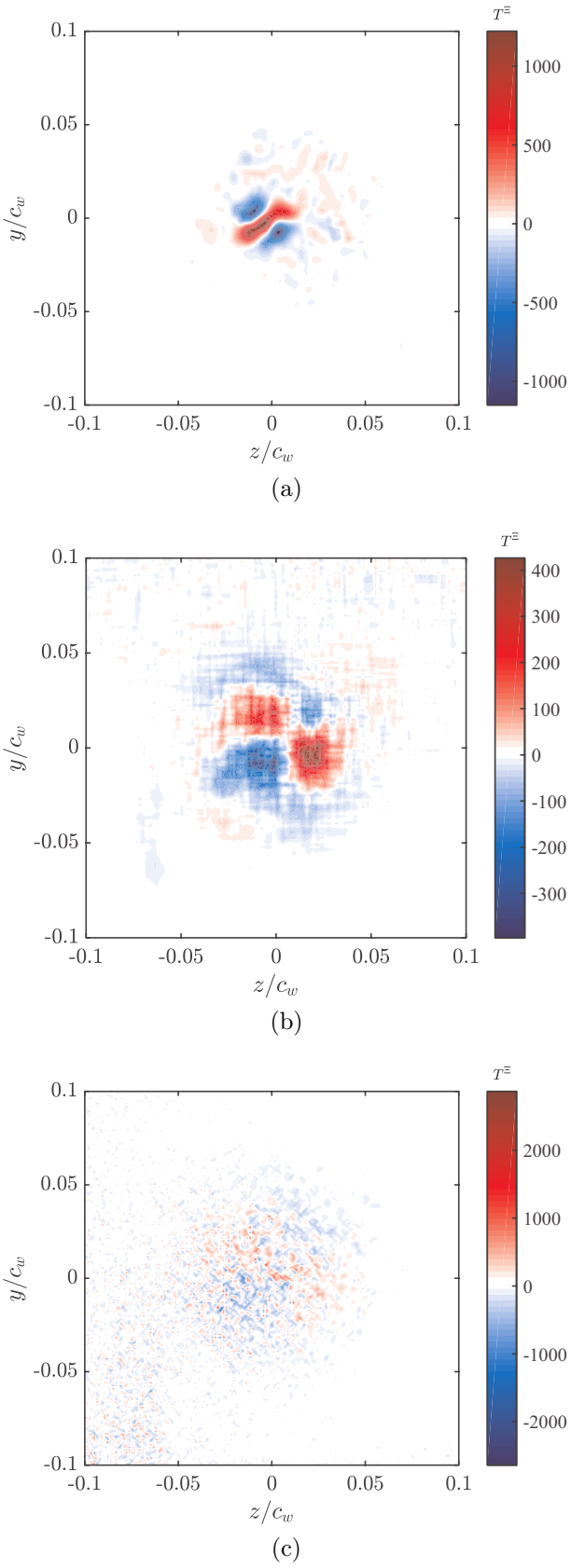

Figure 4.14 Enstrophy equation term T^{Ξ} contours (a) no-grid (b) GP1 and (c) GP2

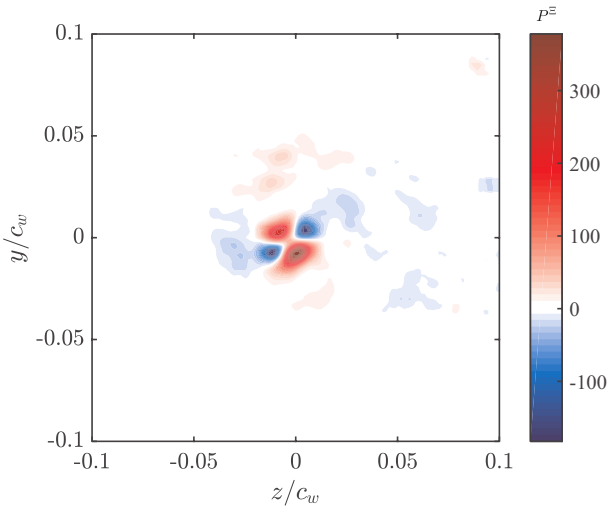

(a)

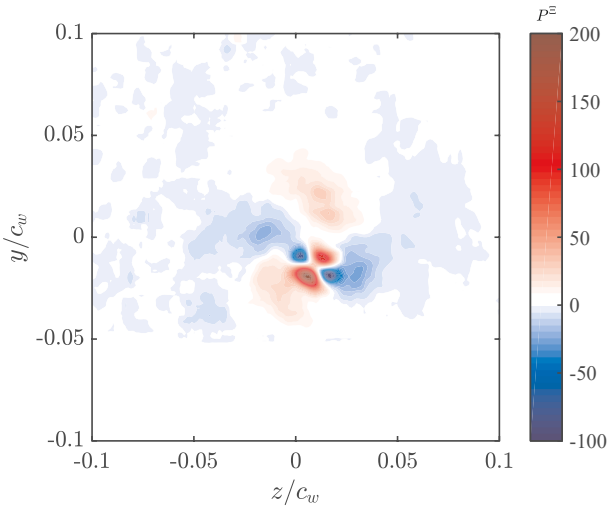

(b)

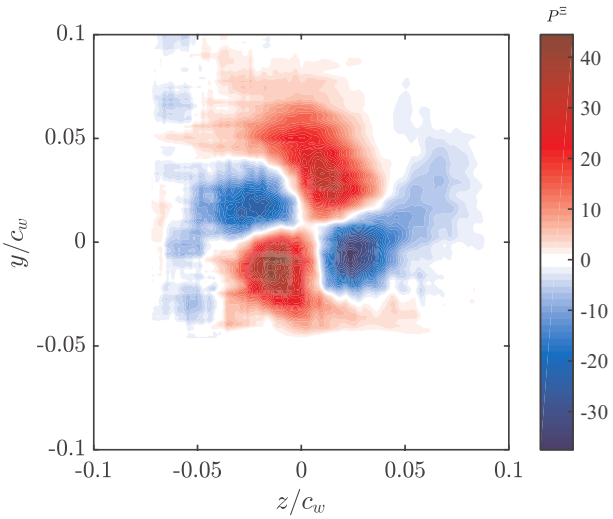

(c)

Figure 4.15 Enstrophy equation term P^{Ξ} contours (a) no-grid (b) GP1 and (c) GP2

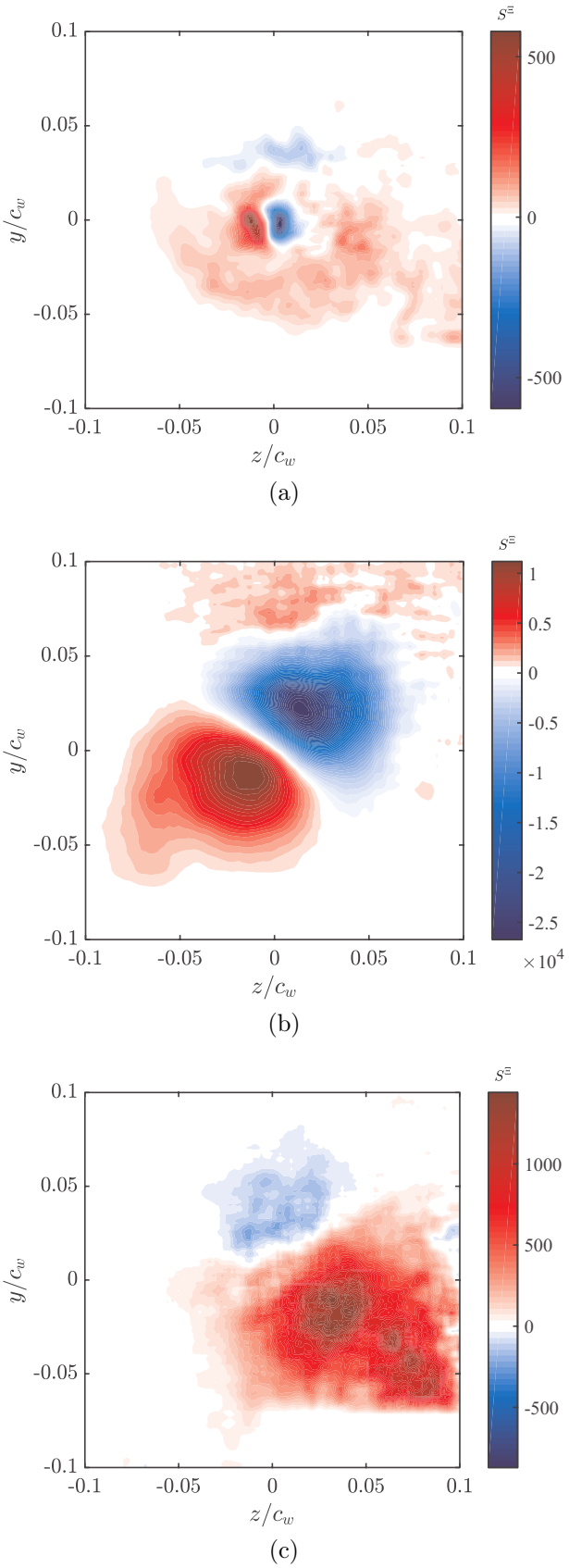

Figure 4.16 Enstrophy equation terms S^{Ξ} contours (a) no-grid (b) GP1 and (c) GP2

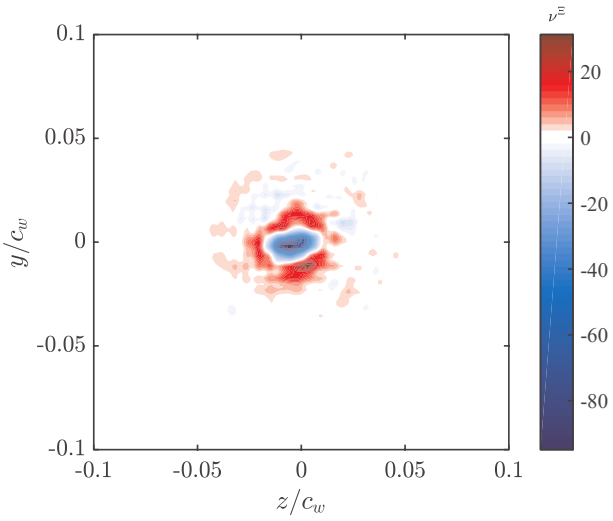

(a)

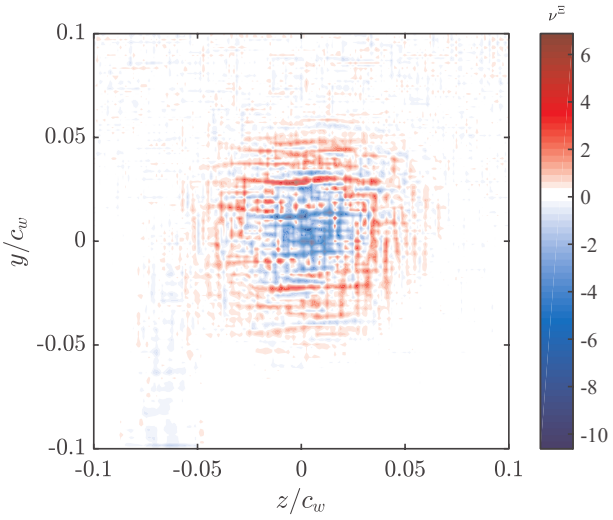

(b)

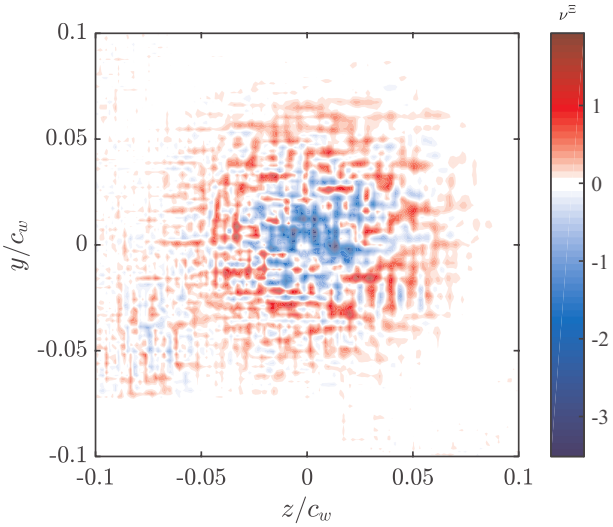

(c)

Figure 4.17 Enstrophy equation terms $\boldsymbol{\nu}^{\boldsymbol{\Xi}}$ contours (a) no-grid (b) GP1 and (c) GP2

4.5 Conclusions

In this chapter, the interaction of a NACA 0012 wing-tip vortex with a turbulent flow generated by a grid was experimentally investigated at a Reynolds number, based on the wing chord length, c_w, of 2×10^5 for the three FST levels considered previously. FST was found to increase the vortex meandering amplitude causing an induced meandering artificial turbulence in the vortex core. It was found to decrease when applying a meandering correction. A POD analysis depicted two helical and dominant modes which formed a dipole, consistent with the the helical displacement of the vortex with an azimuthal wavenumber $m = 1$. The estimation of the mean flow vorticity equation terms revealed that FST contributes to decrease the velocity-vorticity interaction by increasing the stretching and enstrophy terms.

CHAPTER 5

CONCLUSION GÉNÉRALE

La présente étude porte sur l'investigation expérimentale de l'interaction entre la turbulence de l'écoulement libre et le sillage d'un bout d'aile rectangulaire NACA 0012. L'aile a été placée dans la soufflerie à un angle d'attaque de 5 degrés et testée à deux nombres de Reynolds basés sur la corde, $Re_1 = 2 \times 10^5$ et $Re_2 = 3 \times 10^5$, sous l'effet de trois intensités de turbulence, à savoir FST=0.5% (soufflerie sans grille), FST=3% (position GP1) et FST=6% (position GP2), créées à partir d'une grille de maillage carré placée en amont du bord d'attaque de l'aile. Avant d'entreprendre les mesures du champ de vitesse du sillage de l'aile, des mesures par fils chauds ont permis de caractériser la diminution de la turbulence libre ainsi que l'évaluation de l'échelle intégrale de turbulence. Ces deux paramètres ont été évalués, et trouvés en bonne concordance avec les modèles théoriques de turbulence. Ensuite, les mesures du champ de vitesse du sillage ont été entreprises en utilisant la vélocimetrie par imagerie de particules stéréoscopique (SPIV). Les prélèvements ont été effectués dans quatres plans en aval du bord de fuite de l'aile, à savoir x/c_w = 1.25, 3.25, 6.25 et 7.75 pour les trois intensités de turbulence FST=0.5%,3% et 6%. Les contours de champs de vitesse axiale reportés dans les plans de mesures ont révélé des structures de vortex qui s'assimilent aux profils type "wake-like". Ils décrivent ainsi un déficit de vitesse dans le coeur du vortex, $\bar{u}_d$, qui décroit longitudinalement en aval du bord de fuite de l'aile. A la position x/c_w = 1.25, et pour le même nombre de Reynolds, une réduction du maximum de déficite de vitesse a été observée avec l'augmentation de FST, correspondant à 26% et 35% pour GP1 et GP2 respectivement, en comparaison avec le cas sans grille. Entre autre, les profils de vitesse tangentielle normalisée, $\bar{v}_\theta/\bar{u}_0$, et le rayon normalisé, r_c/c_w, du tourbillon ont été évalués. Il a été constaté que le taux de changement du rayon du tourbillon, et le taux de décroissance du maximum de la vitesse tangentielle sont indépendants du nombre de Reynolds Re. Des interpolations avec des fonctions de puissance ont suggéré des exposants de -0.005 à Re_1 et -0.004 à Re_2 pour les valeurs maximales de $\bar{v}_\theta/\bar{u}_0$, et 0.006 à Re_1 et 0.004 à Re_2. De plus, un ajustement avec la courbe théorique de Phillips [50] a été appliqué sur les profils de vitesse tangentielle. Un bon agrément a été observé qui décrit un tourbillon auto-préservé. Il a été déduit que l'étape d'enroulement du tourbillon a été complétée et le coeur du tourbillon a évolué asymptotiquement à partir de $x/c_w \sim 3$. Cependant, la structure du coeur du vortex ne semblait pas être altérée par la turbulence de l'écoulement libre ou le nombre de Reynolds, comme

les profils de vitesse tangentielle décrivaient une concordance raisonable avec l'équation théorique pour toutes les positions en aval du bord de fuite de l'aile. D'autre part, les contours de vorticité ont permis également de constater que l'augmentation de l'intensité de turbulence dans le sillage avait un effet considérable, particulièrement pour la position de grille GP2. Plus précisément, l'augmentation de FST favorise la diffusion du tourbillon. En effet, à $x/c_w = 1.25$, le maximum de vorticité atteint au coeur du tourbillon est de $\bar{\xi}_x \, c_w/\bar{u}_0 = 13$, qui décroit de 50% à $x/c_w = 7.75$. La compréhension du mouvement de l'axe horizontal du tourbillon, nommé aussi errance du tourbillon a été menée suite à la détermination du centre instantané des tourbillons en aval de l'aile. Ceci a permis de déterminer les amplitudes de l'errance du tourbillon qui augmente avec l'augmentation de FST. Entre autres, son estimation a permis d'appliquer une correction de turbulence apparente, générée sur les contours de l'énergie cinétique turbulente.

Dans une deuxième partie de l'étude, une analyse détaillé sur l'errance du tourbillon a été effectuée en utilisant la Décomposition Orthogornale aux valeurs Propres (POD). L'extraction du mouvement des structures cohérentes a été traitée pour les positions reportées dans les parties précédentes pour les trois intensités de turbulence, mais pour $Re_1 = 2 \times 10^5$. Les modes les plus énergétiques ont été déterminés. De plus, une caractérisation des mécanismes de diffusion du tourbillon a été obtenue à travers l'évaluation des termes de l'équation de transport de l'enstrophie. Il a été ainsi déduit que le FST contribue à la réduction de l'interaction vitesse-vorticité tout en augmentant les termes de cisaillement et d'enstrophy.

Recommendations pour travaux futurs

- Effectuer des mesures par vélocimétrie par imagerie de particules dans le sens longitudinal afin d'examiner le trajet de l'axe du tourbillon. Un système avec hautes fréquences serait bénifique pour permettre d'améliorer la résolution temporaire.
- Effectuer des mesures de points par fil chaud sur une région du coeur du vortex. Des points supplémentaires pourraient fournir d'autres informations comparables aux résultats de la SPIV.
- Effecter des visualisations sur différents plans. Un arrangement interne est à prévoir.

- Effectuer une vélocimetrie par imagerie de particules résolue à hautes fréquences sur l'aile pour détecter les structures secondaires, cette information pourrait contribuer aux connaissances sur la formation du tourbillon.

CHAPTER 6

GENERAL CONCLUSION

The present study concerns an experimental investigating of free stream turbulence (FST) interaction with a wing-tip vortex of a rectangular NACA 0012 wing, placed at 5 degrees inside the wind tunnel. Two Reynolds numbers, based on the wing cord length, $Re_1 = 2 \times 10^5$ and $Re_2 = 3 \times 10^5$ were considered, with three FST levels, FST=0.5% (no grid), FST =3% (position GP1) and FST=6% (position GP2), generated using a squared mesh grid placed upstream the wing's leading edge.

At first, before performing measurements of the wake velocity field, hot wires were used to characterize the decay of the free stream turbulence and evaluate the integral length scale. These two main parameters were found in good agreement with the theoretical models of turbulence. The vortex velocity field was quantified using stereoscpic particle image velocimetry (SPIV). Samples were taken at four downstream positions, $x/c = 1.25$, 3.25, 6.25 and 7.75 for the three free stream turbulence levels, FST=0.5%, FST=3% and FST=6% with two Reynolds numbers 2×10^5 and 3×10^5. The axial velocity field contours revelead that the vortex structures assimilated a wake-like profile where they depicted an axial velocity deficit in the vortex core region, $\bar{u}_d$, which decreased in the streamwise direction. At the position $x/c = 1.25$ and for the same Reynolds number, a peak of the velocity deficit was reported with increased FST, corresponding to 26% and 35% for GP1 and GP2 respectively, in comparison with the no-grid case. The normalized circumferential velocity profiles, $\bar{v_\theta}/\bar{u}_0$ and the normalized radius,r_c/c_w, of the vortex core were estimated. It was suggested that the rate of change of theses two parameters is independant of Re number. Interpolations with a power law suggested exponents of -0.005 for $Re = 2 \times 10^5$ and 0.004 for $Re = 3 \times 10^5$ for the peak values of $\bar{v_\theta}/\bar{u}_0$, and 0.006 for $Re_1 = 2 \times 10^5$ and 0.004 for $Re_2 = 3 \times 10^5$. These results were in agreement with those reported by [33, 91].

In addition, an adjustment with the theoretical model of Phillips [50] was applied to the circumferential velocity profiles. A good collapse has been observed which dictated a self-preserved vortex. It may be inferred from the presented data that, at $x/c_w \sim 3$, the roll up process was completed and the vortex core had evolved asymptotically to reach a nearly axisymmetric distribution. The vorticity contours also showed that the FST had a considerable effect on the vortex diffusion, particularly for the GP2 position, at $x/c = 1.25$; the maximum vorticity reached in the heart of the vortex is 13 which decreased by 50%

at $x/c = 7.75$. Understanding the movement of the horizontal axis of the vortex, has also been addressed in this thesis. The amplitudes of the vortex meandering were observed to increase with FST increase. A correction of the apparent turbulence generated on the contours of the turbulent kinetic energy, was also applied and showed decreased turbulence levels after meandering correction.

In the last part of the study, the extraction of the coherent structures was processed for the positions reported in the previous part for the three FST levels, but for $Re_1 = 2 \times 10^5$. The most energetic structure have been determined. In addition, a characterization of the vorticity diffusion mechanisms was obtained through the evaluation of the enstrophy transport equation terms. The FST contributed to the reduction of velocity-vorticity interaction while increasing the shear and enstrophy terms.

As the vortex is generated behind the trailing edge of the wing, it decays after a certain time and distance. It was shown in previous studies that FST greatly affects a wing-tip vortex formation and development, and increasing Re strengthens the vortex. While current solutions do not prevent the vortex formation, there are several technologies that could benefit from this study. Our data could be explored from our study if future technologies use turbulence to reduce the vortex strength. As a matter of fact, a recent experimental study performed by DLR in Germany used runway "dissipators" where vertical plates are placed at the edge of runways to accelerate the dissipation rate of the vortex.

Recommendations for future works

- Perform Stereoscopic Particle Image Velocimetry in the streamwise direction, to evaluate the vortex axis path. Time resolved would also be beneficial as the temporal resolution shall be improved. In this study, the temporal resolution was 15 Hz, a time revolved system would have much more higher frequency of acquisition (in the range 200 Hz).
- Perform flow visualization in different planes. Due to Wind tunnel accommodation, this task requires internal setup.
- Perform Hot-wire point measurements on a vortex core region, additional points on the spectra could map the vortex core meandering frequencies.
- Perform Time resolved Particle Image velocimetry on the wing. The secondary structures were not visualized in this study, however, such information could bring additional information on the vortex formation.

APPENDIX A
Appendix

A.1 Experimental procedure

In this section, a description of the experimental procedure is provided. It includes the work that was achieved on the wind tunnel before the measurements compaign, and several experimental data that were used for the processing and post-processing. For clarity, no screen shots from the software used are presented herein.

In order to investigate the effect of free stream turbulence on the vortex formation and development, it is important that the generated grid turbulence does not contain any additional background turbulence. It is actually purely related to the flow quality of the flow inside the wind tunnel test section. The generated turbulence has to be as close as possible to an isotropic turbulence [118].

The wind-tunnel airflow is generated using a rotating engine delivering 200 horse power Figure A.1a. The as-built background turbulence intensity was 0.3%. Temperature increase was noticed inside the wind tunnel which was created by the engine heat, it could affect the sensitivity of the probes such as the hot-wire. Operating the wind tunnel for long hours is for instance a challenge. To overcome this issue, custom-made heat exchangers were installed in the upper section of the wind tunnel to allow a certain cooling. This option showed some improvement as the air temperature increase was controlled at a certain level. It was about 2-3 degrees Celsius. The wind tunnel was powered off between testing campaigns to allow more cooling. The heat exchangers were made of copper tubes installed vertically in the upper section of the wind tunnel, Figure A.1b, with a diameter of 15 mm. Cold water with a temperature of 4° Celsius supplies the tubes to allow maximum cooling and heat loss when the air flows. In order to smoothen the air passage from the upper section of the wind tunnel to the lower one, guidance vanes are installed at the end of the wind tunnel contraction. Honeycombs were installed at the exit of the guidance vanes which allow to straighten the deflected flow coming from the upper section Figure A.2. Hexagonal shape is commonly used as it allowed a lower pressure drop coefficient Figure A.2. The flow structure has to be rigid enough and smaller than the smallest lateral wavelength of the velocity variation. It is important that the incoming air flows with a yaw angle lower than 10° in order to avoid honeycomb cells stalling. It reduces their effectiveness and causes a pressure drop as well [119]. This shape removes the air swirl motion and decreases the lateral variations in mean and fluctuating velocity while they allow a more horizontal flow parallel to the wind tunnel axis [120]. According to Barlow et al. [121] and Rae et al. [122], Hexagonal shape offers the least pressure drop comparing to circular or square shapes. The authors stated that the smallest lateral wavelength of the velocity variation should be greater than the cell size. Few figures describging the experimental setup are represented in figures Figure A.3, Figure A.4, Figure A.5, Figure A.6.

(a)

(b)

Figure A.1 (a) Wind tunnel test section (b) Heat exchangers inside the wind tunnel

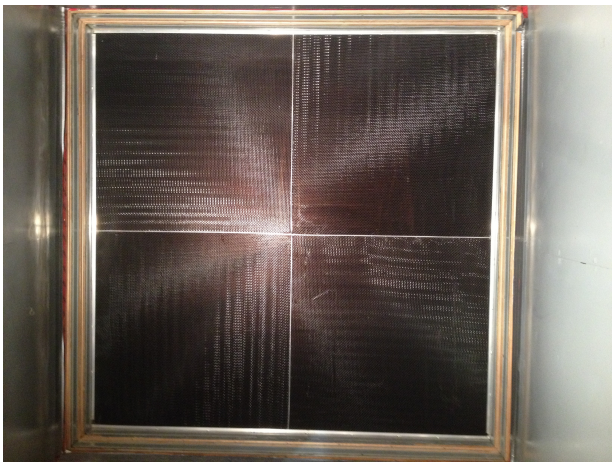

Figure A.2 Wind tunnel Honeycombs

The Reynolds number has an important effect on the efficiency of screens and honeycombs. Both the screen and honeycombs should be rigid enough and also must not create any additional turbulence in the flow. The velocity fluctuations in the streamwise and spanwise directions are considerably reduced when using a screen. Schubauer et al. [123] performed experiments with different screens and different wire diameters. They stated that the scale of turbulence is unchanged while using a damping screen, any additional turbulence generation could result from the presence of a vortex shedding and the screens aim to cascade large-scale turbulent fluctuations into smaller scales. In our study, two screens with a square meshing of 1/32 and 1/4 inches were used Figure A.7. The flow quality was evaluated for both screens. With the insertion of screens, honeycombs and grid, a certain pressure loss is created inside the wind tunnel. This latter was estimated using the screen pressure loss formula given by Rae et al. [122]:

$$K = K_0 + \frac{55.2}{R_d}, \tag{A.1}$$

where:

$$K_0 = \frac{1 - 0.95 \times \beta}{0.95 \times \beta^2}, \tag{A.2}$$

and :

β=projected Opened Area/ Total Area

And R_d is the Reynolds number based on the rods diameter of 10 mm. The grid solidity is 0.43 while the estimated pressure loss is about 22%.

A.1.1 Measurement procedure

the wind tunnel measurements have been achieved using a cobra probe and hot-wires. The TSI single and crossed wire were used to evaluate the flow quality and detect areas where the flow uniformity is not respected.

A.1.2 Cobra and hot-wire measurements

The Cobra Probe has been largely used in turbulent flows. It can allow a range of frequencies higher than 2 KHz [122] and can measure velocities up to 100 m/s. The Cobra Probe incorporates four 0.5 mm pressure taps in a multi-faceted head, Figure A.8. The probe has four holes which give access to the flow three velocity components. It allows pressure measurements and all six Reynolds stresses as well. The frequency response of the Probe is linearized to allow estimation of the mean velocity component to more than 2000 Hz [124]. The probe is self-calibrated and ready to use, manufacturer's recommendation stated however, that occasional transducer re-calibration is needed (approximately each 6 months). The TFI turbulent flows software has a friendly user interface which allowed easy and quick acquisitions. An A/D Texas instrument card is used to connect the cobra probe.

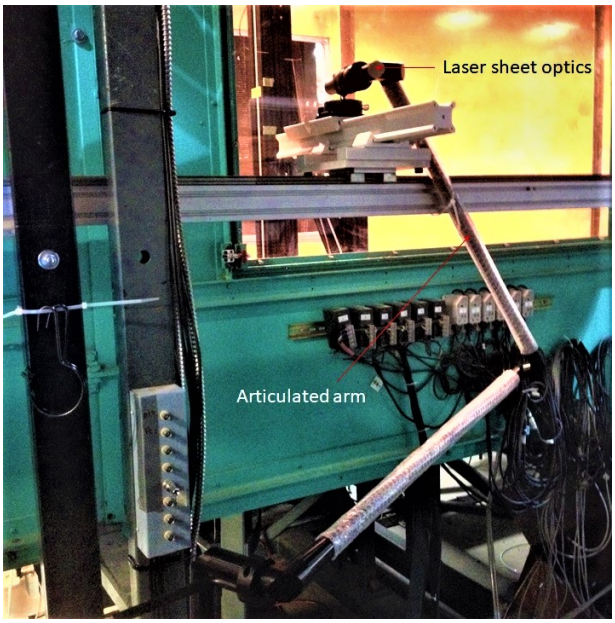

Figure A.3 Articulated arm

The Hot-wire is a reference turbulence measurement device Figure A.9. Beside the fact that it has been largely used, hot-wires still present a high frequency response to flow fluctuations. Compared to cobra probe, there is certainly a large gap as it can reach up to 100 kHz while cobra allows a maximum of 2 kHz (Some devices can acquire with higher

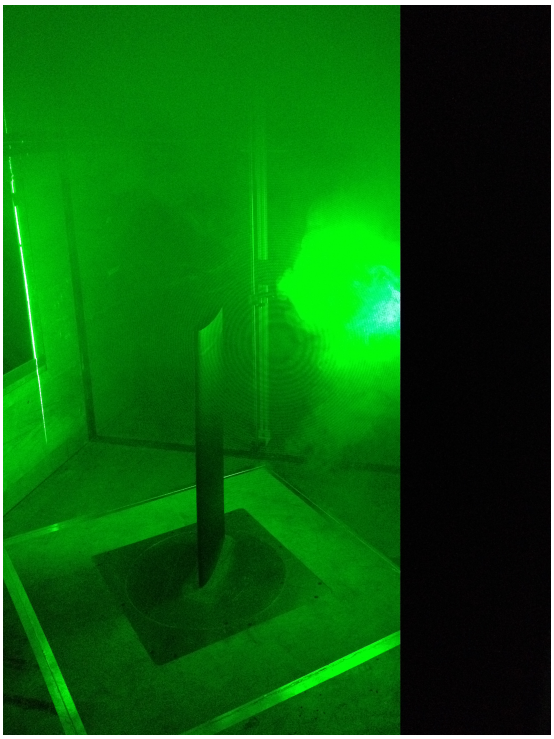

Figure A.4 Wing

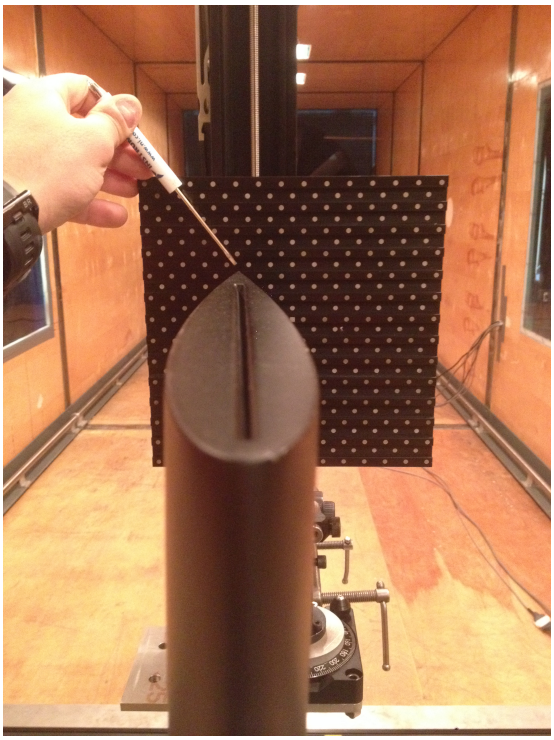

Figure A.5 Calibration plate

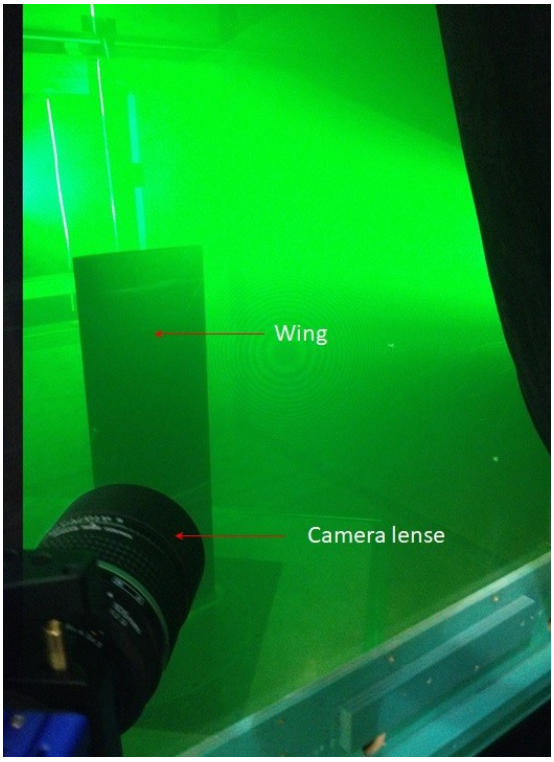

Figure A.6 Camera angle

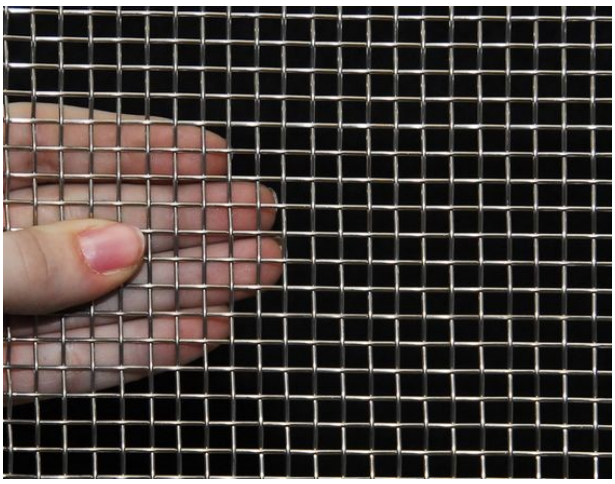

(a)

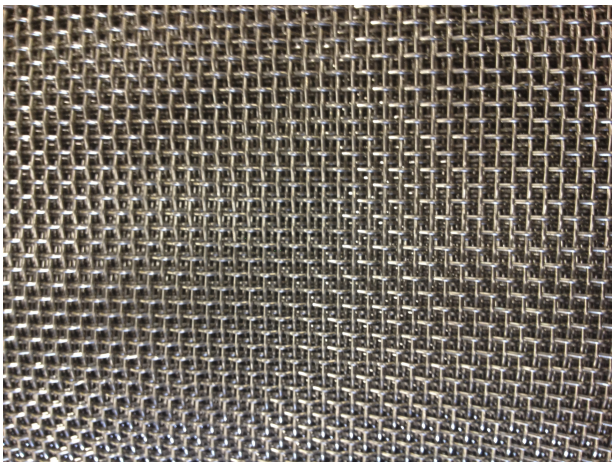

(b)

Figure A.7 (a) 1/4 inches screen (b)1/32 inches screen

(a)

Figure A.8 Cobra probe

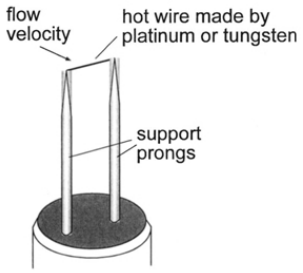

(a)

Figure A.9 Single Hotwire probe

frequency). The use of hot-wires requires however more diligent precautions due to their fragility. While the cobra probe is self-calibrated, hot-wires require a concise calibration. In this study, the TSI single and cross-wires were installed inside the wind tunnel to evaluate the flow quality and the turbulence decay. A Constant Temperature Anemometry (CTA) setup is used with an IFA300 anemometer. It is suitable for flows having sensitive fluctuations. In fact, by warming the hot-wire, its resistance is translated to a voltage which is converted to velocity using the King's law, or the 4^{th} order polynomial law. The resistance of the cable, the wire and the operating resistance need prior measurement before starting the calibration. A TSI calibration jet is used for that purpose. The King law is given by:

$$E^2 = (A + B \times U^n) \times (T_W - T_a), \tag{A.3}$$

- T_w : Wire temperature
- T_a : airflow temperature
- U : Normal velocity to the wire
- E : Measured Voltage at Wheatstone bridge
- n : Exponent, estimated from the calibration process
- A and B are constants, estimated from the calibration process

The wire resistance is estimated as follows:

- Cable resistance (RC): Using a shorting probe, the cable resistance is determined without any hot-wire installed. R_c is the resistance of the cable connecting the IFA300 and the probe support.
- After placing the hot-wire on its support, the measured resistance gives the total resistance of the circuit, the cable with the wire and the support. As a matter of

fact, the support is a rigid tube with internal connections that allow the voltage reading.

The wire resistance R_W is obtained by subtracting the cable resistance (which includes the probe support) from the total resistance, such as:

$$R_W = R_T - R_C, \tag{A.4}$$

An overheat factor is required to be applied on the wire resistance to increase its effectiveness. This operation is applied for both wires in the case of a cross-wire. The current values were 1.37 Ohm and 7.79 Ohm for the cable and operating resistances, respectively. Also, note that a gain of 10 and an offset of 1.3 were used.

The cobra probe is disposed inside the wind tunnel along with a hot-wire sensors, separated with approximately 5 cm (Figure A.10). This provided enough space to avoid any interference between the two measuring probes. To estimate the flow quality, acquisition is acquired in an area of interest of about 4 ft^2. Both cobra probe and hot-wires were disposed on a VELMEX 32 bi-slide traversing system (Figure A.11). Constructed with hard-coat anodized, aluminum dovetail ways, the VELMEX 32 is equipped with a lead screw that offers an accuracy of 0.003" ($0.076mm$) over the entire course distance. The flow quality measurement is conducted on the leading edge position of the wing with a Reynolds number, based on a chord length of 30 cm, of: $Re_1 = 2 \times 10^5$ and $Re_2 = 3 \times 10^5$, respectively, which correspond to a wind tunnel velocity of: 10 and 15 m/s.

Flow quality adjustments

In order to ensure a flow uniformity in the test section, patchs were used in the upper section of the wind tunnel upper section. The reported turbulence intensity in the empty tunnel with cobra probe was about 1.8% which agrees with the hot-wire recorded data. It has been decided to pursue the measurements with 1/32 inches screen to reduce this turbulence intensity. This latter shows less turbulence levels, but illustrates the existence of a sheared flow in the right hand side of the test section. This was improved by adding small sheets of screen inside to increase the flow uniformity. The results showed a good improvement in the flow quality and a reduction in the turbulence levels. An average turbulence level of about 0.5% was achieved, which corresponded to the no-grid case of this study.

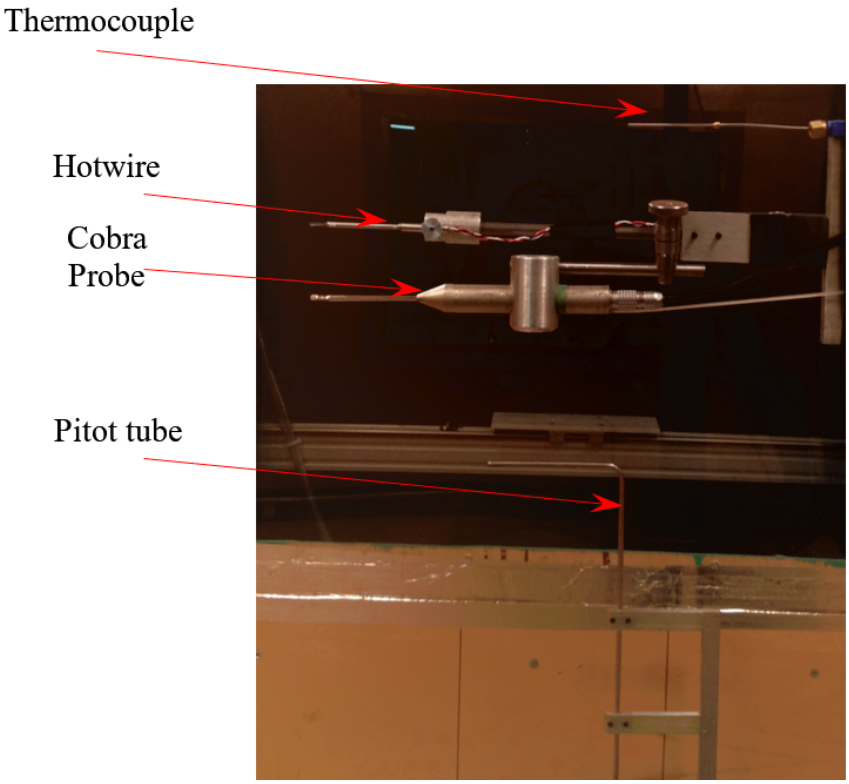

(a)

Figure A.10 Probes installed on the traversing system

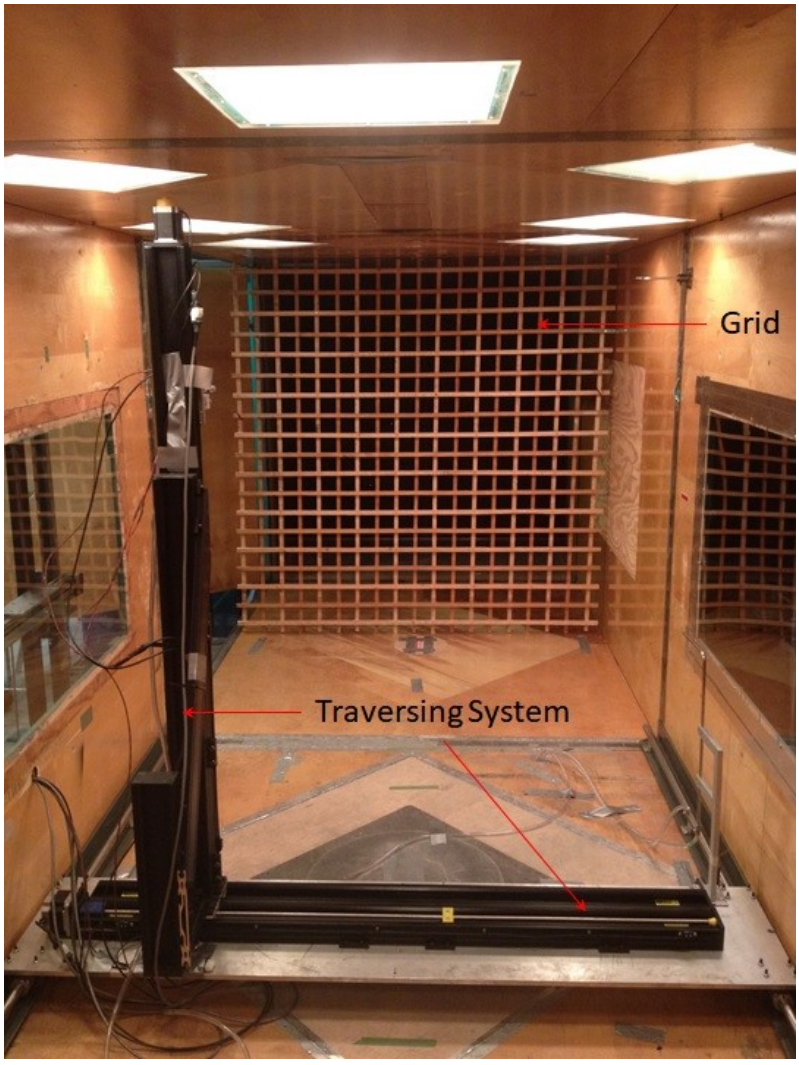

(a)

Figure A.11 Traversing system inside the wind tunnel

A.1.3 Stereoscopic Particle Image Velocimetry (SPIV) data

SCMOS Camera Specifications

General System Specifications:

- Double shutter : two images with 120 ns interframing time
- Exposure time 10 μs - 100 μ
- Digital output : 16 bits
- Camera interface : PCI-ExpressCard (4 slots)
- Lens mount : F-mount
- Number of pixels : 2560 × 2160 pixels
- Pixel Size : 6.5 μm × 6.5 μm
- Active Areal : 16.6 mm × 14.0 mm
- Spectral range : 370 - 1100 nm
- Quantum efficiency : tup.53% - 532 nm
- Full well capacity : 30.000 e^-
- Readout noise : $< 3e^-$ - 286 MHz
- Frame rate : 50 fps

Scheimpflug operations

In order to optimize the focus over the entire field of view, the use of an optical mean is required. Using a direct angle between the camera lense and the calibration plate resulted in areas with less focus causing the appearance of blurry areas. Such regions in fact illustrated false vectors which affected the quality of the measurements. The mounting of a Scheimpflug adapter between the camera interface and the lens arranged the field of view focus. The adjustment is conducted empirically [125]. The alignment is a sensitive process, focusing the camera lens in the middle of the area of interest is the first step. After that, tilting the Scheimpflug toward the direction of less focus resulted in a wider focused range Figure A.12. In certain downstream distances, the focusing using the Scheimpflug is not evident for the length of the wind tunnel.

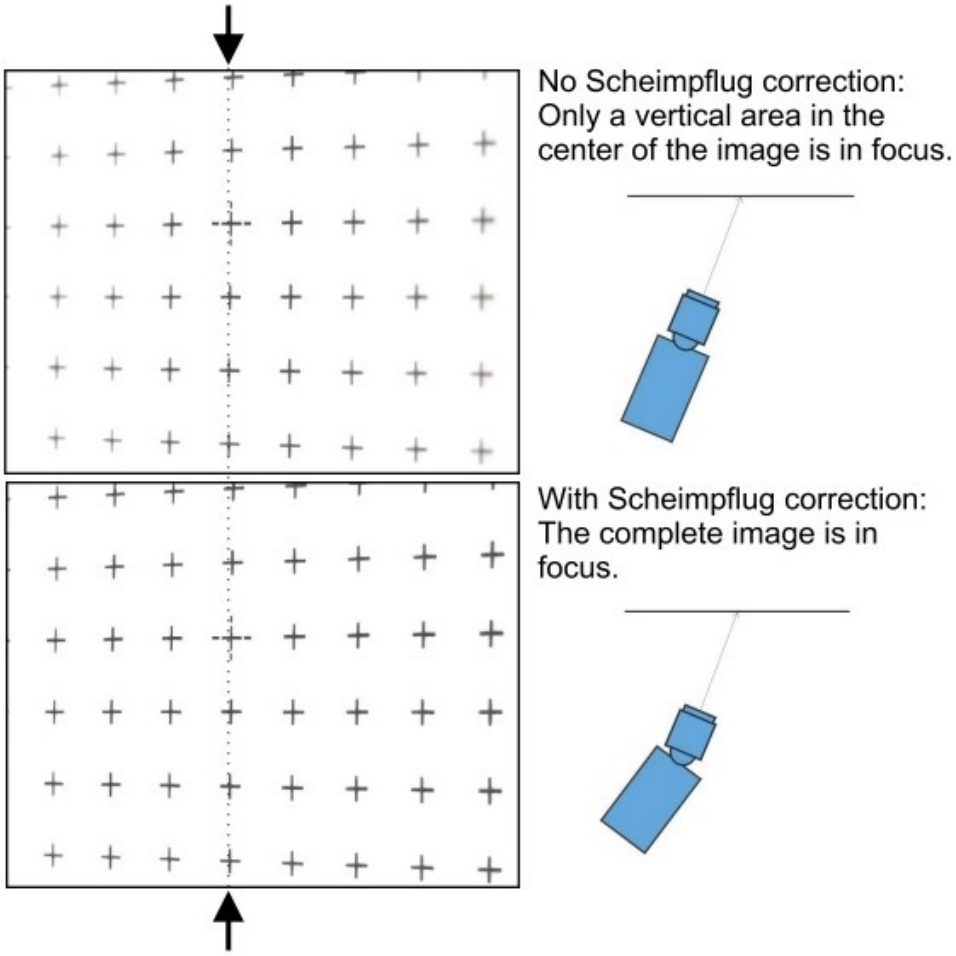

Figure A.12 Scheimpflug operation [125]

SPIV processing and post-processing

In this section, few calculations are provided for the set up of the SPIV configuration.

Data :

- NIKKON Lens focal length : 200 mm
- Resolution : 2560 × 2160 pixels
- Pixel pitch : 6.5 μm × 6.5 μm
- Sensor format : 16.64 × 14.04

Field of view dimensions : FOV = 2560 × 2160 / Calibration factor = 166.89 × 140.8

The magnification factor is given by the ratio between the sensor size and the field of view :

M=16.64 / 166.89 = 0.0997

Calculation of time pulse

For the SPIV setup, the laser sheet thickness and the in and out of plane velocity components have a major effect on the time between two frames. For an interrogation window of 32 px × 32 px:

$$\Delta t < \frac{0.3 \times dl}{max|u_{inplane}|} \tag{A.5}$$

$$\boxed{\Delta t < 74.5 \mu s}$$

$$\Delta t > \frac{0.3 \times dl}{max|u_{outofplane}|} \tag{A.6}$$

$$\boxed{\Delta t > 53.57 \mu s}$$

It is also necessary to estimate the diameter associated with the differentiation effect:

$$d_{diff} = 8.44 \times f_{\#} \times (1 + M) \times \lambda \tag{A.7}$$

$$\boxed{d_{diff} = 5.76 \mu m}$$

The seeding particle diameter is $d_p = 1 \mu m$

From which the particle image diameter could be estimated using the formula :

$$d = \sqrt{d_{diff}^2 + (M \times d_p)^2} \tag{A.8}$$

$$\boxed{d = 5.71 \mu m}$$

The depth of field is another parameter important for SPIV measurements. It is evaluated as :

$$\delta z = 4.8 \times \frac{1+M}{M} \times f_{\#}^2 \times \lambda \tag{A.9}$$

$$\boxed{\delta z = 0.46mm}$$

To achieve a valid detection probability of at least 90%, it is recommended to estimate the minimum pulse separation. This parameter depends on the image density (number of particles per interrogation window), which is > 15.

Once the SPIV frames are captured using the above parameters (these parameters change for each plane and a new calibration is performed), a set of operations are performed on Davis 8.0 to achieve a detailed post-processing. For the purpose of this thesis, only the important parameters are listed herein. Depending on the case studied (no-grid or with grid), the technique used for the post-processing is different. Commonly, a set of filters was applied which include time and field correction procedures. These two steps are very important because they affect the quality of the processing.

SPIV uncertainty calculation

The velocity vector fields were calculated at a final correlation window size of 32 px by 32 px with an overlap of 75%, resulting in a vector spacing of approximately 0.5 mm. The measurement uncertainty level for the velocity vectors was estimated to be within 2%. The method used to obtain the uncertainty estimate of 3% was based on several criteria as reported in the literature. A summary of these techniques is presented herein :

- Magnification Error

Magnification error was evaluated using the technique of Discetti and Adrian [126], it was given as :

$$\epsilon = \frac{\gamma}{1-\gamma} \times 100 \tag{A.10}$$

Where $\gamma = z_p/z_0$

The magnification error was found to be less then 0.2%

- Particle tracking error

The tracking particle error was estimated using the analysis provided by Birch and Martin [127]. Particle tracking error occurs when the seeding particle fails to follow the fluid motion [85]. Using a batchlor vortex model, Birch and Martin [127], the tracking error was estimated using the formula :

$$\frac{v}{v'} = 1 + A \times exp\left(-B\eta^2\right) \tag{A.11}$$

v' represents the tangential velocity of the seeding particle.
η is the ration of r/r_c
A is the error amplitude, the maximum of which can be evaluated using the formula [85]

$$A = 2\left(\alpha + \frac{1}{2}\right)^2 B'^2 \tag{A.12}$$

$B^{'} = \frac{v_0^{'}}{Cr_0^{'}}$

B is a constant : $14 \leq B \leq 1400$

r_0' is the location of the peak tangential velocity, v_0' of the seeding particle [85]

- Peak locking error

The peak locking error occurs when the particle image on the sensor is too small than the pixel dimension. The particle image diameter could be obtained using the formula [85] :

$$d_p = sqrt(M^2 d_p^2 + d_s^2) \tag{A.13}$$

M is the average magnification
d_s is the diffraction diameter, which is estimated using the formula :

$$d_s = 2.44\,(M+1)\,\frac{f\lambda}{D} \tag{A.14}$$

f is the focal length of the lens
D is the aperture diameter
λ is the laser wave length

If d_r is the pixel projected diameter then $\frac{d_p}{d_r} \geq 2$. For instance, our measurements are exempt of peak locking errors.

A.2 Analytical background

A.2.1 Vortex theoretical models

Several models were proposed in the literature that associate the vortex properties with theoretical quantities. A brief description of these models is presented herein. In this thesis, only the model of Phillips was applied. The models below were reported in the studies of Ghimire [31]

- **Rankine vortex model**

$$v_\theta(r) = \frac{\Gamma_0}{2\pi r_c}\frac{r}{r_c}, r \leq r_c \tag{A.15}$$

$$v_\theta(r) = \frac{\Gamma_0}{2\pi r}, r > r_c \tag{A.16}$$

- **Lamb-Oseen vortex model**

$$v_\theta(r) = \frac{\Gamma_0}{2\pi r}\left(1 - exp\left(-1.2526\left(\frac{r}{r_c}\right)^2\right)\right) \tag{A.17}$$

- **Hallock-Burnham**

$$v_\theta(r) = \frac{\Gamma_0}{2\pi r}\frac{r^2}{r^2 + r_c^2} \tag{A.18}$$

- **Smooth blending**

$$v_\theta(r) = \frac{\Gamma_0}{2\pi r}\left(1 - exp\left(-\frac{\beta_i\left(\frac{r}{b}\right)^2}{\left(1 + \left(\frac{\beta_i}{\beta_0}\left[\frac{r}{b}\right]^{5/4}\right)^p\right)^{1/p}}\right)\right), \beta_i = \beta_0 = 10,500, p = 3 \tag{A.19}$$

- **q-vortex**

$$v_\theta(r) = \frac{\Gamma_t}{2\pi r}\left(1 - exp - \left(\frac{r}{r_c}\right)^2\right) \tag{A.20}$$

- **Phillips circumferential velocity model [81]**

$$\frac{v_\theta}{v_{\theta_{max}}} = \frac{1}{0.716\left(\frac{r}{r_{\theta_{max}}}\right)}\left(1 - exp\left(-1.2526\left(\frac{r}{r_{\theta_{max}}}\right)^2\right)\right) \tag{A.21}$$

A.3 Spectra Analysis results

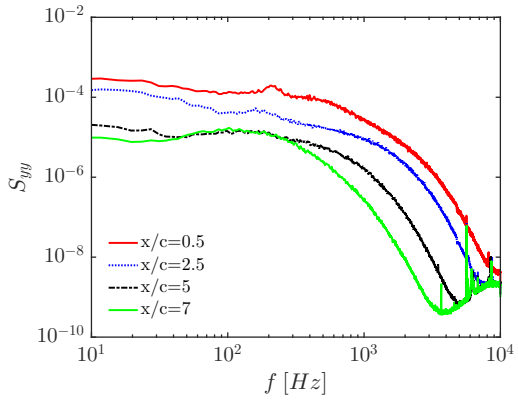

(a)

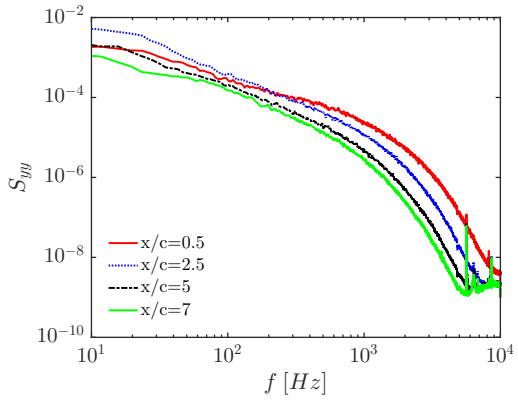

(b)

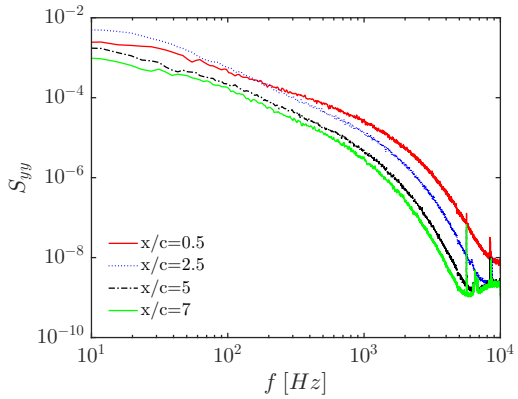

(c)

Figure A.13 High frequency spectra of $\bar{U}_y$ at the vortex averaged center position for (a)no-grid (b)GP1 and (c)GP2

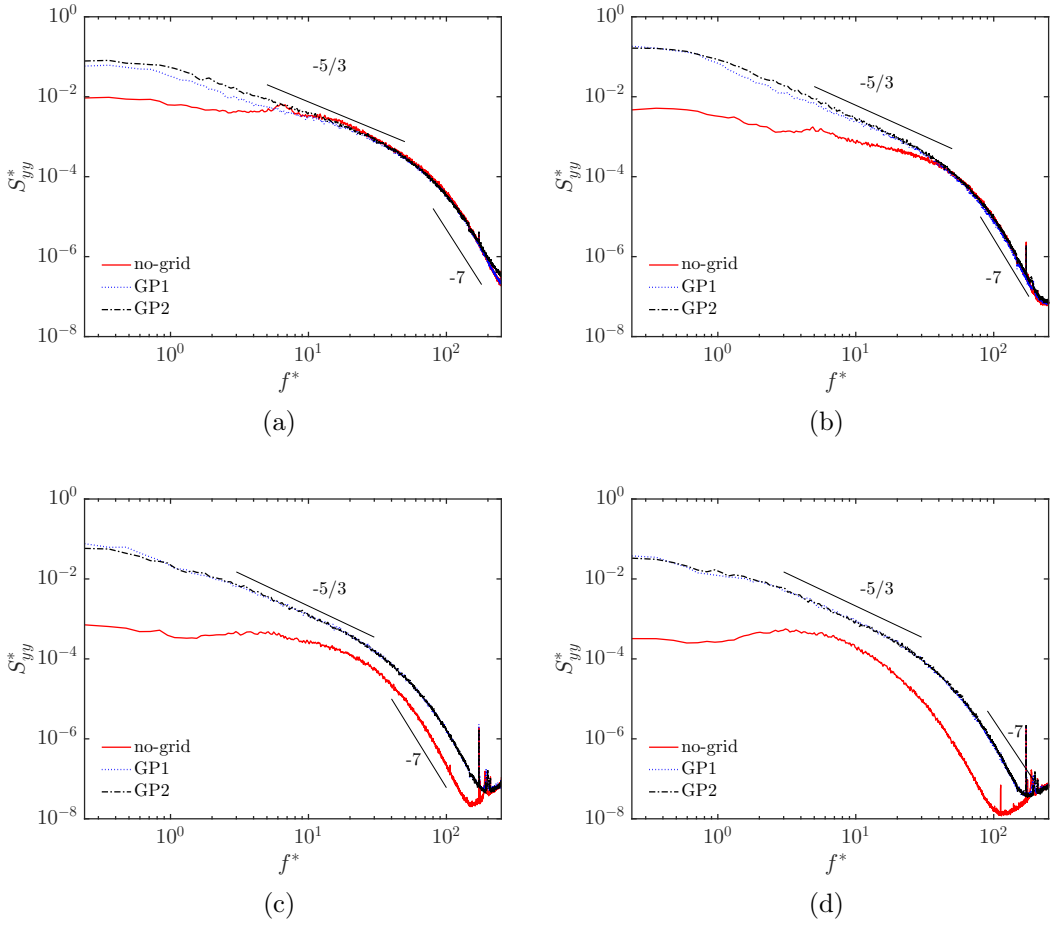

Figure A.14 Normalized high Frequency spectra of $\bar{U}_y$ in the inner core region (a)$x/c_w = 1.25$, (b)$x/c_w = 3.25$, (c)$x/c_w = 6.25$ and (c)$x/c_w = 7.75$

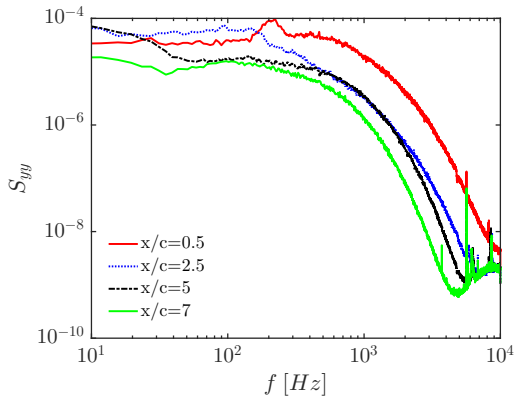

(a)

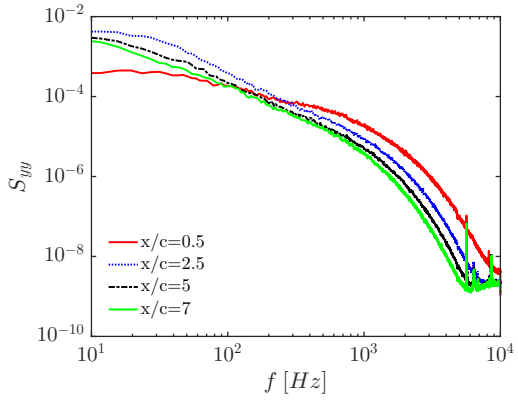

(b)

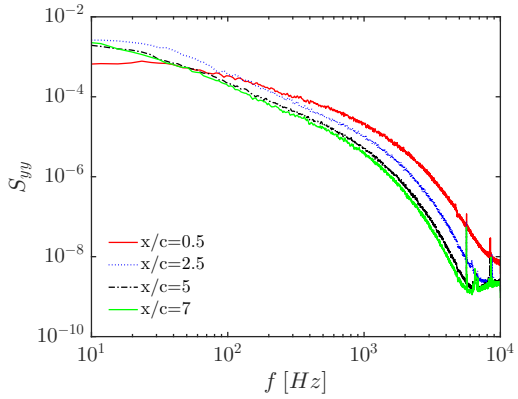

(c)

Figure A.15 High frequency spectra of $\bar{U}_y$ at the averaged position of the shear layer for (a)no-grid (b)GP1 and (c)GP2

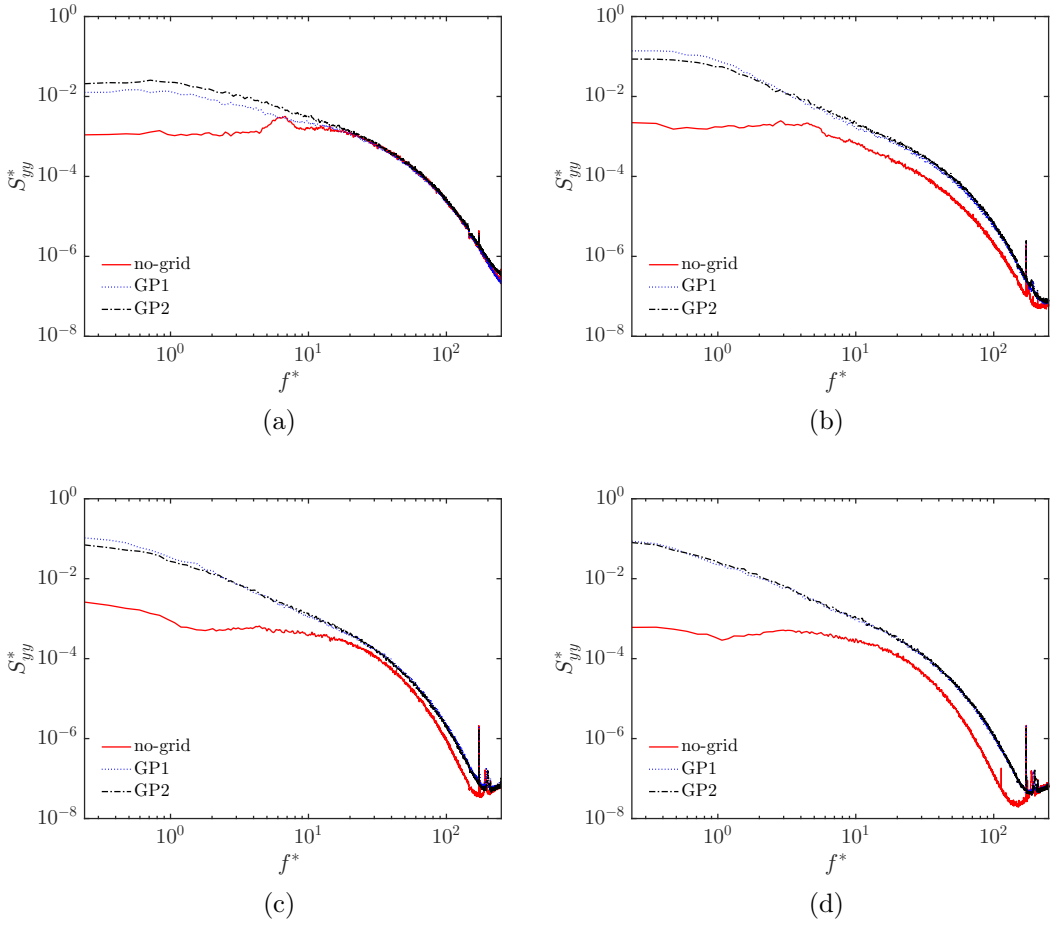

Figure A.16 Normalized high frequency spectra of $\bar{U}_y$ in the average position of the shear layer at different downstream positions $x/c_w = 1.25$, (b)$x/c_w = 3.25$, (c)$x/c_w = 6.25$ and (d)$x/c_w = 7.75$

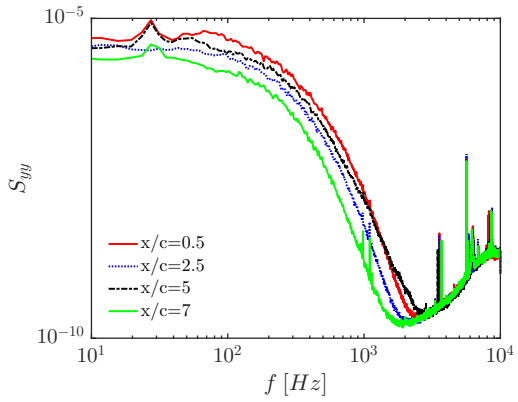

(a)

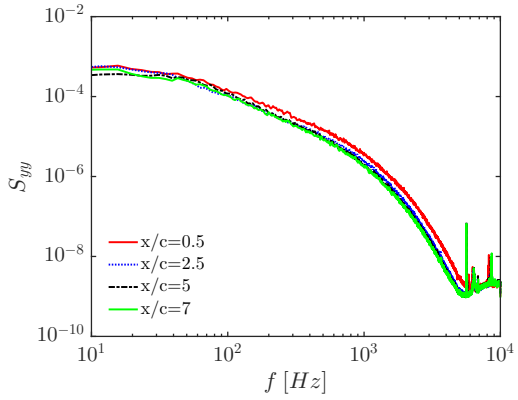

(b)

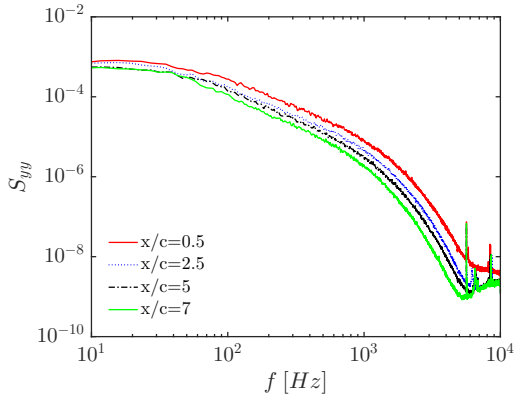

(c)

Figure A.17 High frequency spectra of $\bar{U}_y$ at the outer region for (a)no-grid (b)GP1 and (c)GP2

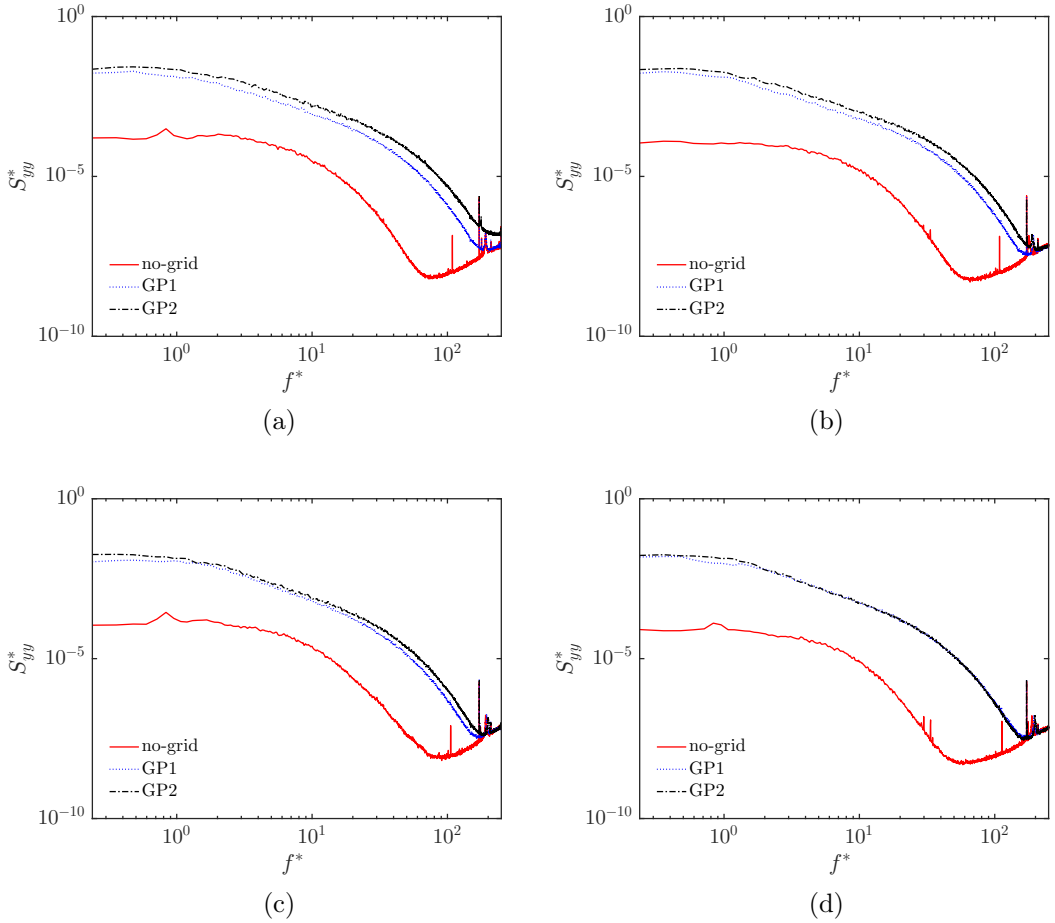

Figure A.18 Normalized high frequency spectra of $\bar{U}_y$ in the average position in the outer region at different downstream positions $x/c_w = 1.25$, (b)$x/c_w = 3.25$, (c)$x/c_w = 6.25$ and (d)$x/c_w = 7.75$

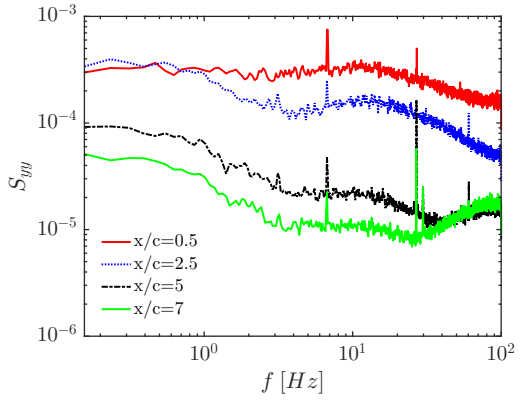

(a)

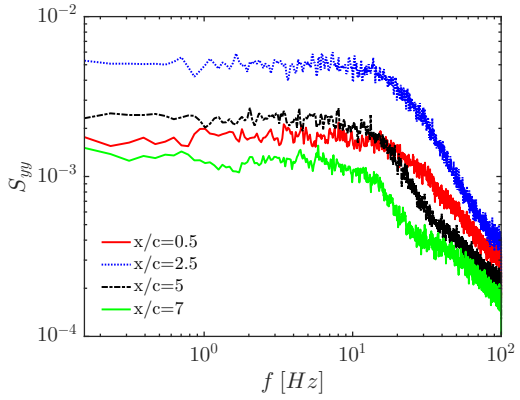

(b)

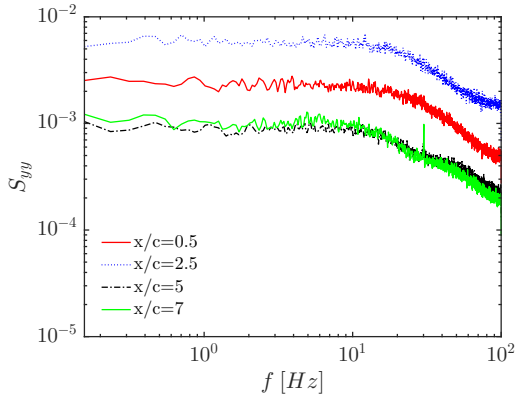

(c)

Figure A.19 Low frequency spectra of $\bar{U}_y$ at the vortex averaged center position for (a)no-grid (b)GP1 and (c)GP2

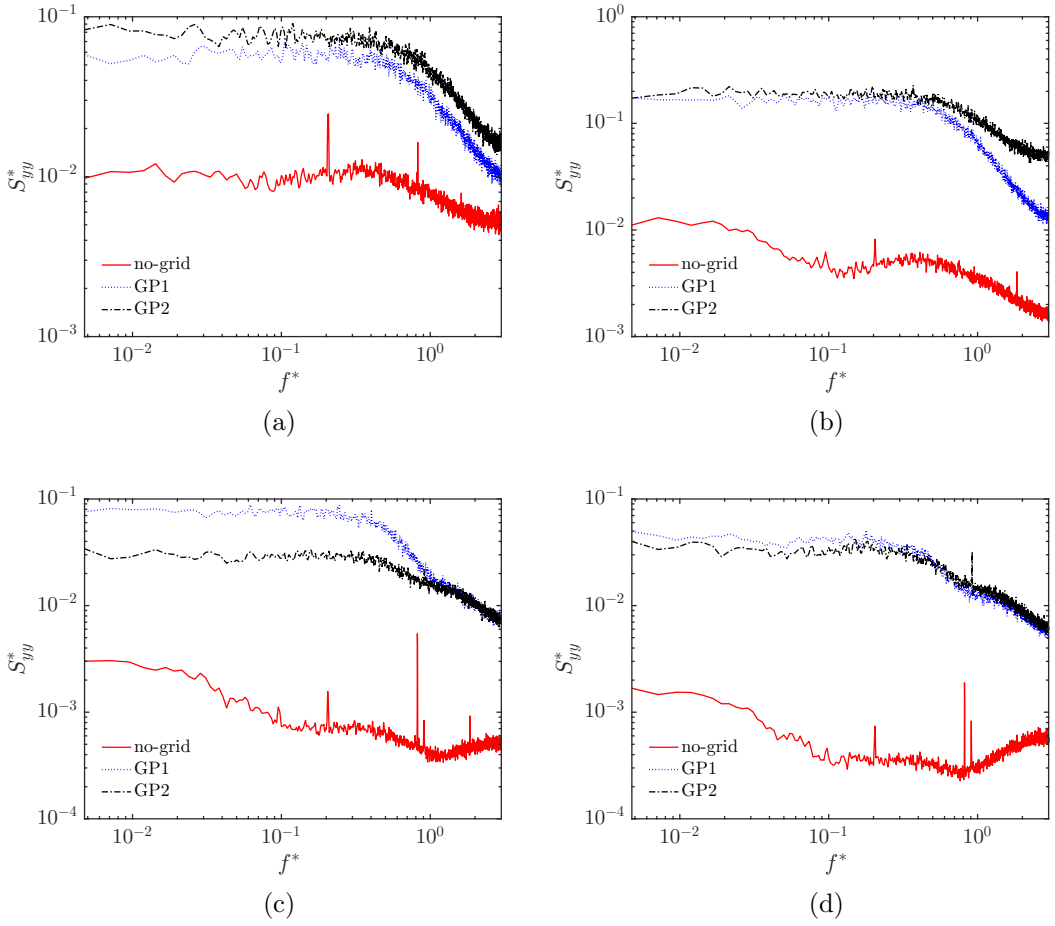

Figure A.20 Normalized Low Frequency spectra of $\bar{U}_y$ at the averaged center position (a)FST=0.5% (b)FST=3% and (c)FST=6%

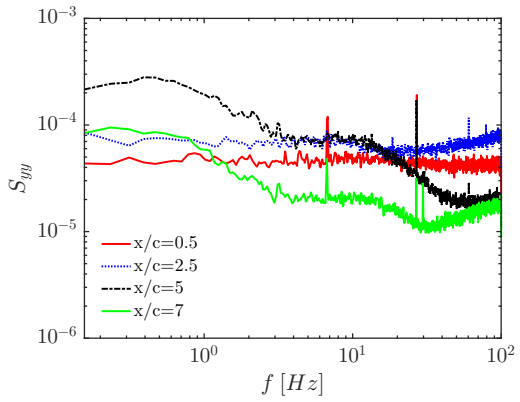

(a)

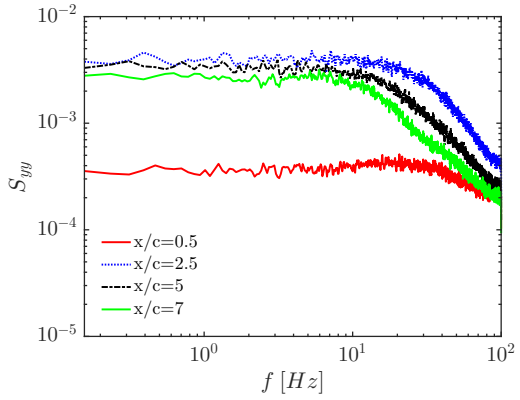

(b)

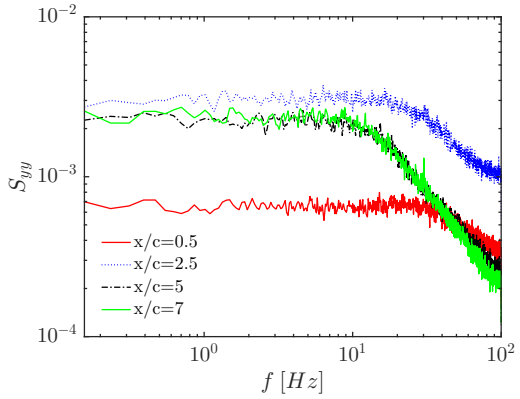

(c)

Figure A.21 Low frequency spectra of $\bar{U}_y$ at the shear layer averaged position for (a)no-grid (b)GP1 and (c)GP2

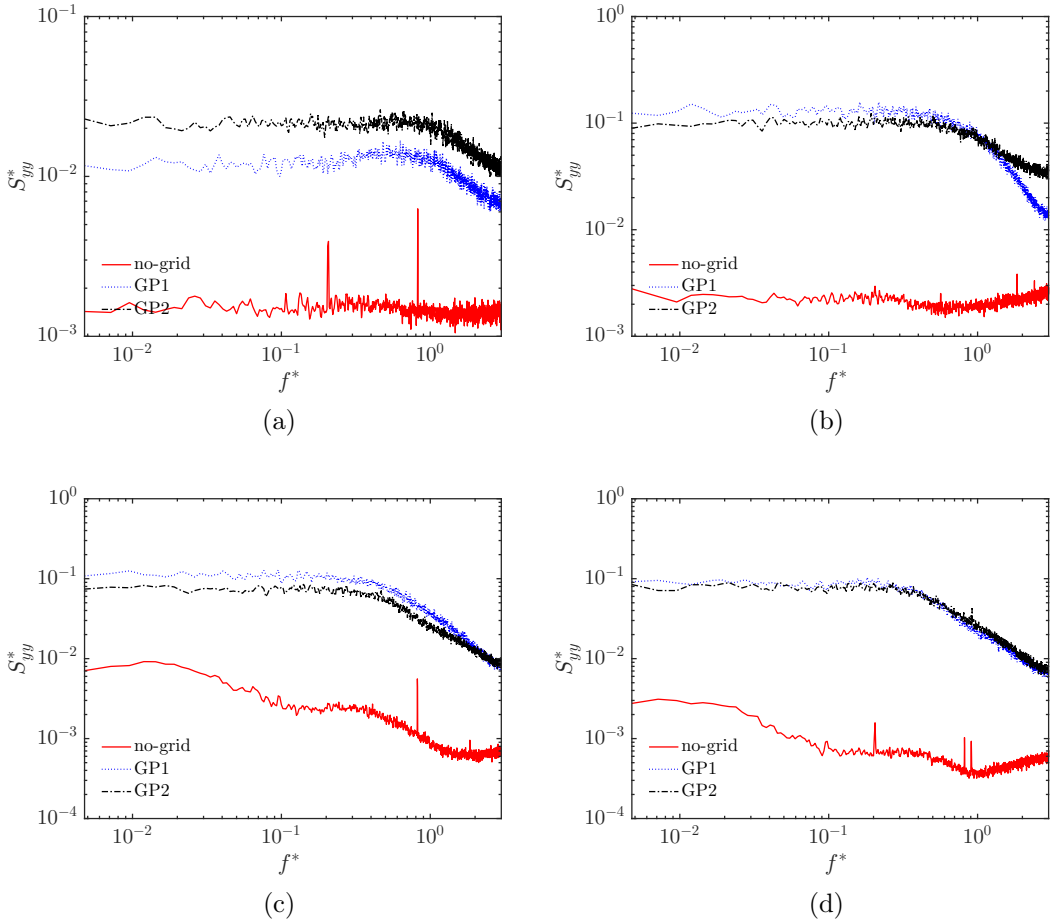

Figure A.22 Normalized Low frequency spectra of $\bar{U}_y$ at the shear layer averaged position at different downstream positions $x/c_w = 1.25$, (b)$x/c_w = 3.25$, (c)$x/c_w = 6.25$ and (d)$x/c_w = 7.75$

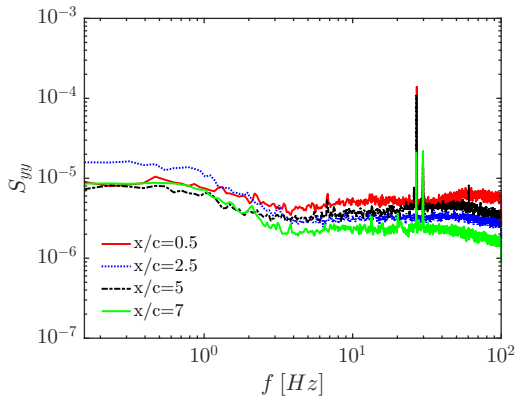

(a)

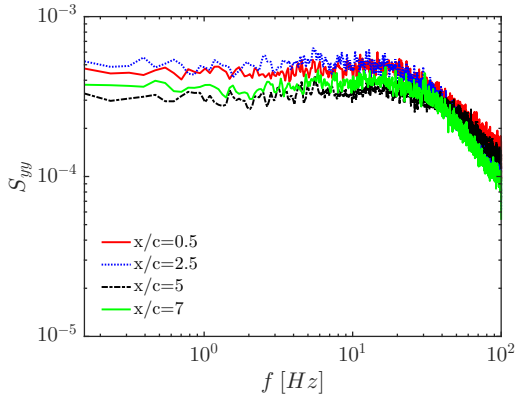

(b)

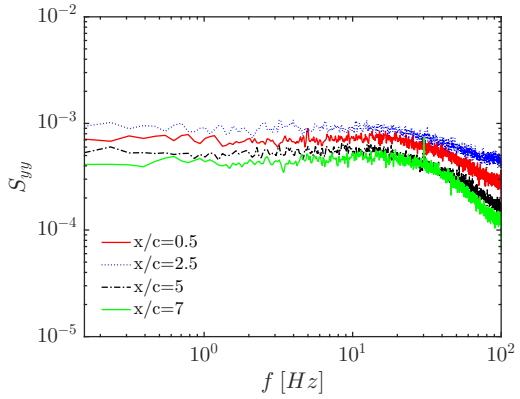

(c)

Figure A.23 Low frequency spectra of at the outer region for (a)no-grid (b)GP1 and (c)GP2

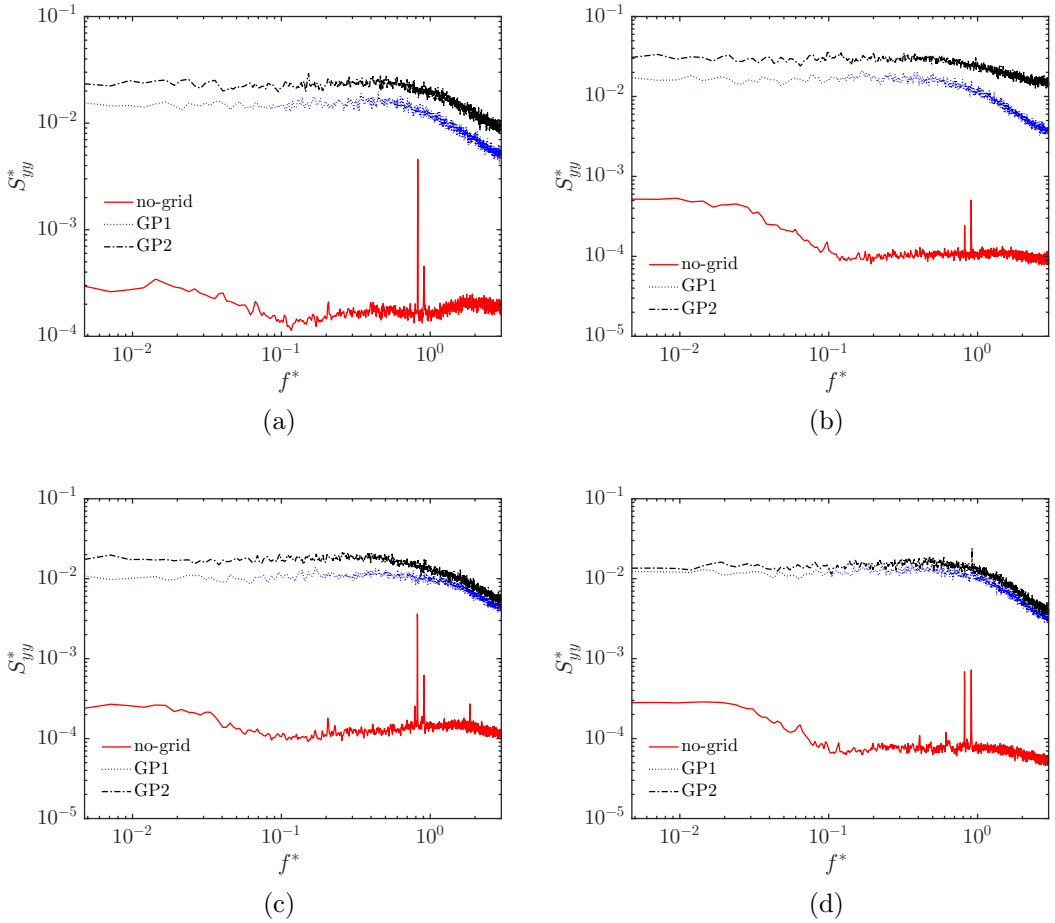

Figure A.24 Normalized Low frequency spectra in the average position at the outer region at different downstream positions $x/c_w = 1.25$, (b)$x/c_w = 3.25$, (c)$x/c_w = 6.25$ and (d)$x/c_w = 7.75$

LIST OF REFERENCES

[1] V.J Rossow. Lift-generated vortex wakes of subsonic transport aircraft. *Progress in Aerospace Sciences*, 35(6):507–660, 1999.

[2] G Fagerstrom. Wing-tip vortices. *www.flyindian.wordpress.com*, 2010.

[3] C. Breitsamter. Wake vortex characteristics of transport aircraft. *Progress in Aerospace Sciences*, 47(2):89–134, 2011.

[4] SCC. Bailey and S. Tavoularis. Measurements of the velocity field of a wing-tip vortex, wandering in grid turbulence. *Journal of Fluid Mechanics*, 601:281–315, 2008.

[5] S. Pentelow. *Wing-tip vortex structure and wandering.* PhD Thesis - Carleton University, 2014.

[6] W. Phillips. The turbulent trailing vortex during roll-up. *Journal of Fluid Mechanics*, 105:451–467, 1981.

[7] LaVision. *SPIV User Guide.* LaVision.

[8] W. Schröder. Fluid mechanics research at the institute of aerodynamics, rwth aachen university: From 1912 through 2012. *European Journal of Mechanics B Fluids*, 40:2–16, 2013.

[9] J. Dacles-Mariani, G. Zilliac, JS. Chow, and P. Bradshaw. Numerical and experimental study of a wing-tip vortex in the near field. *AIAA journal*, 33(9):1561–1568, 1995.

[10] J. Dacles-Mariani, D. Kwak, and G. Zilliac. On numerical errors and turbulence modeling in tip vortex flow prediction. *International journal for numerical methods in fluids*, 30(1):65–82, 1999.

[11] J.A. Ekaterinaris. Numerical investigation of dynamic stall of an oscillating wing. *AIAA journal*, 33(10):1803–1808, 1995.

[12] G.R. Srinivasan, W.J. McCroskey, J.D. Baeder, and T.A. Edwards. Numerical simulation of tip vortices of wings in subsonic and transonic flows. *AIAA journal*, 26(10):1153–1162, 1988.

[13] D.P. Rizzetta. Numerical investigation of supersonic wing-tip vortices. *AIAA journal*, 34(6):1203–1208, 1996.

[14] R.E. Spall. Numerical study of a wing-tip vortex using the euler equations. *Journal of Aircraft*, 38(1):22–27, 2001.

[15] E. Fares, M. Meinke, and W. Schroeder. Numerical simulation of the interaction of wing-tip vortices and engine jets in the near field. In *Fluids 2000 Conference and Exhibit*, page 2222, 2000.

[16] M.J. Churchfield and G.A. Blaisdell. Numerical simulations of a wing-tip vortex in the near field. *Journal of Aircraft*, 46(1):230–243, 2009.

[17] H. Igarashi, P. Durbin, H. Ma, and H. Hu. A stereoscopic piv study of a near-field wing-tip vortex. *AIAA Paper*, 1029(2010):2010–1029, 2010.

[18] Federal Aviation Administration Department of Transportation. Federal aviation administration aeronautical information manual. Technical report, 2017.

[19] W. Luber. Wake penetration effects on dynamic loads and structural design of military and civil aircraft. In *Structural Dynamics, Volume 3*, pages 1381–1402. Springer, 2011.

[20] R. Nelson. Trailing vortex wake encounters at altitude-a potential flight safety issue. In *AIAA Atmospheric Flight Mechanics Conference and Exhibit*, page 6268, 2006.

[21] J.U. Klar, C. Breitsamter, S. Hickel, and N. Adams. Integrated experimental-numerical analysis of high-agility aircraft wake vortex evolution. *Journal of Aircraft*, 48(6):2050–2058, 2011.

[22] H. Djojodihardjo. Review on development and recent patents on trailing vortices alleviation. *Recent Patents on Mechanical Engineering*, 4(2):83–129, 2011.

[23] RT. Whitcomb. A design approach and selected wind tunnel results at high subsonic speeds for wing-tip mounted winglets. Technical Note NASA TN D-8260., NASA, 1976.

[24] N.A. Siddiqui, M. Aldeeb, W. Asrar, and E. Sulaeman. Experimental investigation of a new spiral wing-tip. *International Journal of Aviation, Aeronautics, and Aerospace*, 5(2):6, 2018.

[25] R.J. Kelly and J.M. Davis. Required navigation performance (rnp) for precision approach and landing with gnss application. *Navigation*, 41(1), 2018.

[26] R. Cassel and A. Smith. Development of required navigation performance (rnp) requirements for airport surface mouvement guidance and control. In *Proceedigs of 14th digital avionics systems conference*, pages 57–64, 2004.

[27] M. Dghim, M. Ferchichi, and M. BenChiekh. Control of wing tip vortex structure using fluidic actuation. In *7th AIAA Flow Control Conference*, page 2792, 2014.

[28] M. Dghim, M. Ferchichi, R. Perez, and M. BenChiekh. Near wake development of a wing tip vortex under the effect of synthetic jet actuation. *Aerospace Science and Technology*, 54:88–107, 2016.

[29] M. Dghim and M. Ferchichi. The structure and development of a wing tip vortex under the effect of synthetic jet actuation. In *World Academy of Science, Engineering and Technology, International Journal of Aerospace and Mechanical Engineering*, page 3(1), 2016.

[30] M. Dghim. *On the effect of active flow control on the meandering of a wing tip vortex*. PhD Thesis, Université de Sherbrooke, 2018.

[31] T. Misaka, F. Holzäpfel, and T. Gerz. Wake evolution of wing-body configuration from roll-up to vortex decay. In *50th AIAA Aerospace Sciences Meeting including the New Horizons Forum and Aerospace Exposition*, page 428, 2012.

[32] M. Giuni and R.B. Green. Vortex formation on squared and rounded tip. *Aerospace science and technology*, 29(1):191–199, 2013.

[33] A. Stephan. *Wake vortices of landing aircraft*. PhD Thesis, Munich University, 2014.

[34] G.K. Batchelor. Axial flow in trailing line vortices. *Journal of Fluid Mechanics*, 20(4):645–658, 1964.

[35] W. Hofmann and J. Ballmann. Tip clearance vortex development and shock-vortex-interaction in a transonic axial compressor rotor. In *AIAA Aerospace Sciences Meeting & Exhibit, 40 th, Reno, NV*, 2002.

[36] H.C. Ghimire. *Wing-tip Vortex Evolution in Turbulence*. PhD Thesis - University of Kentucky, 2018.

[37] J.M.R. Graham. The lift on an aerofoil in starting flow. *Journal of Fluid Mechanics*, 133:413–425, 1983.

[38] H. Zhou. Numerical analysis of wing vortex aerodynamic characteristics. In *8th International Conference on Social Network, Communication and Education (SNCE 2018)*. Atlantis Press, 2018.

[39] J. Katz and J.B. Galdo. Effect of roughness on rollup of tip vortices on a rectangular hydrofoil. *Journal of aircraft*, 26(3):247–253, 1989.

[40] T. Lee and J. Pereira. Nature of wakelike and jetlike axial tip vortex flows. *Journal of aircraft*, 47(6):1946–1954, 2010.

[41] E.A. Anderson and T.A. Lawton. Correlation between vortex strength and axial velocity in a trailing vortex. *Journal of aircraft*, 40(4):699–704, 2003.

[42] B.R. Ramaprian and Y. Zheng. Measurements in rollup region of the tip vortex from a rectangular wing. *Aiaa Journal*, 35(12):1837–1843, 1997.

[43] M. Francis and D.A. Kennedy. Formation of a trailing vortex. *Journal of Aircraft*, 16(3):148–154, 1979.

[44] S. McInerny, W. Meecham, and P. Soderman. Pressure fluctuations in the tip region of a blunt-tipped airfoil. *AIAA Journal*, 28(1):6–13, 1990.

[45] S.I. Green and A.J. Acosta. Unsteady flow in trailing vortices. *Journal of Fluid Mechanics*, 227:107–134, 1991.

[46] D. Birch, T. Lee, F. Mokhtarian, and F. Kafyeke. Structure and induced drag of a tip vortex. *Journal of Aircraft*, 41(5):1138–1145, 2004.

[47] F. Catalano and H. Ceron-Muñoz. Experimental analysis of aerodynamics characteristics of adaptive multi-winglets. page 1231, 2005.

[48] L. Jacquin, D. Fabre, P. Geffroy, and E. Coustols. The properties of a transport aircraft wake in the extended near field-an experimental study. In *39th Aerospace Sciences Meeting and Exhibit*, page 1038, 2001.

[49] P.G. Saffman. *Vortex dynamics*. Cambridge university press, 1992.

[50] A. Shekarriz, T.C. Fu, J. Katz, and T. Huang. Near-field behavior of a tip vortex. *AIAA journal*, 31(1):112–118, 1993.

[51] SCC. Bailey, S. Pentelow, H. Ghimire, B. Estejab, M. Green, and S. Tavoularis. Experimental investigation of the scaling of vortex wandering in turbulent surroundings. *Journal of Fluid Mechanics*, 843:722–747, 2018.

[52] D. Birch, T. Lee, F. Mokhtarian, and F. Kafyeke. Rollup and near-field behavior of a tip vortex. *Journal of Aircraft*, 40(3):603–607, 2003.

[53] E. Hoffmann, R. Errol, and P.N. Joubert. Turbulent line vortices. *Journal of Fluid Mechanics*, 16(03):395–411, 1963.

[54] K.W. McAlister and R.K. Takahashi. Naca 0015 wing pressure and trailing vortex measurements. Technical Report 91-A-003, National Aeronautics and Space Administration Moffett Field Ca Ames Research Center, 1991.

[55] J.H. García-Ortiz, A. Domínguez-Vázquez, J.J. Serrano-Aguilera, L. Parras, and C. del Pino. A complementary numerical and experimental study of the influence of reynolds number on theoretical models for wing-tip vortices. *Computers & Fluids*, 180:176–189, 2019.

[56] C. Chen, Z. Wang, and I. Gursul. Experiments on tip vortices interacting with downstream wings. *Experiments in Fluids*, 59(5):82, 2018.

[57] D. Foti, X. Yang, F. Campagnolo, D. Maniaci, and F. Sotiropoulos. Wake meandering of a model wind turbine operating in two different regimes. *Physical Review Fluids*, 3(5):054607, 2018.

[58] C. Chen, Z. Wang, and I. Gursul. Vortex meandering due to interaction with a downstream wing. In *16th European Turbulence Conference (ETC16)*, 2017.

[59] Z. Cheng, S.Y. Qiu, Y. Xiang, and H. Liu. Quantitative features of wing-tip vortex wandering based on the linear stability analysis. *AIAA Journal*, pages 1–16, 2019.

[60] K. Forster, T. Barber, S. Diasinos, and G. Doig. The variation in co and counter-rotating upstream-downstream vortex interactions. In *47th AIAA Fluid Dynamics Conference*, page 3305, 2017.

[61] T. Sarpkaya and J.J. Daly. Effect of ambient turbulence on trailing vortices. *Journal of Aircraft*, 24(6):399–404, 1987.

[62] G. Capittini, D. Martin, M. Julio, and J.S. Delnero. Vortex generation, experimental characterization, and application in turbulent flows. In *Swirling Flows and Flames*. IntechOpen, 2018.

[63] J.S. Chow, Zilliac.G., and P. Bradshaw. Mean and turbulence measurements in the near field of a wing-tip vortex. *AIAA Journal*, 35(10):1561–1567, 1997.

[64] Javier. Jiménez. Turbulence and vortex dynamics. *Notes for the Polytecnique course on turbulence*, 2004.

[65] R. Ashton, M. Refan, G.V. Iungo, and H. Hangan. Wandering corrections from piv measurements of tornado-like vortices. *Journal of Wind Engineering and Industrial Aerodynamics*, 189:163–172, 2019.

[66] R. Waldman and K.S. Breuer. Accurate measurement of streamwise vortices using dual-plane piv. *Experiments in fluids*, 53(5):1487–1500, 2012.

[67] J. Duncan, D. Dabiri, J. Hove, and M. Gharib. Universal outlier detection for particle image velocimetry (piv) and particle tracking velocimetry (ptv) data. *Measurement Science and Technology*, 21(5):057002, 2010.

[68] S.E. Widnall. The structure and dynamics of vortex filaments. *Annual Review of Fluid Mechanics*, 7(1):141–165, 1975.

[69] J. Boudet, A. Cahuzac, P. Kausche, and M.C. Jacob. Zonal large-eddy simulation of a fan tip-clearance flow, with evidence of vortex wandering. *Journal of Turbomachinery*, 137(6):061001, 2015.

[70] N. Hoang and B.V. Bui. Experimental and numerical studies of wing-tip and downwash effects on horizontal tail. *Journal of Mechanical Science and Technology*, 33(2):649–659, 2019.

[71] B. Ashworth, F. Alexander, D. Alan, B. Jonathan, and R. Jonathan. Tracking the vortex core from a surface-piercing flat plate by particle image velocimetry and numerical simulation. *Proceedings of the Institution of Mechanical Engineers, Part M: Journal of Engineering for the Maritime Environment*, page 1475090218776202, 2018.

[72] X. Mao and J.N. Sørensen. Far-wake meandering induced by atmospheric eddies in flow past a wind turbine. *Journal of Fluid Mechanics*, 846:190–209, 2018.

[73] M. Gupta. *Investigation of active control of aircraft wing tip vortices and wake turbulence*. 2011.

[74] Holmén.V. Methods for vortex identification. *Master's Theses in Mathematical Sciences - Lund University*, 2012.

[75] L. Graftieaux, M. Michard, and N. Grosjean. Combining piv, pod and vortex identification algorithms for the study of unsteady turbulent swirling flows. *Measurement Science and technology*, 12(9):1422, 2001.

[76] P.R. Spalart. Airplane trailing vortices. *Annual Review of Fluid Mechanics*, 30(1):107–138, 1998.

[77] W. Devenport, M.C. Rife, S. Liapis, and G.J. Follin. The structure and development of a wing-tip vortex. *Journal of Fluid Mechanics*, 312:67–106, 1996.

[78] S.C. Crow. Stability theory for a pair of trailing vortices. *AIAA Journal*, 8(12):2172–2179, 1970.

[79] V.R. Corsiglia, R.G. Schwind, and N.A. Chigier. Rapid scanning, three-dimensional hot-wire anemometersurveys of wing-tip vortices. *Journal of Aircraft*, 10(12):752–757, 1973.

[80] S. Ragab and M. Sreedhar. Numerical simulation of vortices with axial velocity deficits. *Physics of fluids*, 7(3):549–558, 1995.

[81] A. Heyes, R.F. Jones, and D. Smith. Wandering of wing-tip vortices. In *Proceedings of the 12th International Symposium on Applications of Laser Techniques to Fluid Mechanics*, pages 35–3, 2004.

[82] M. Ahmadi-Baloutaki, R. Carriveau, and D.S.K. Ting. Effect of free stream turbulence on flow characteristics over a transversely-grooved surface. *Experimental Thermal and Fluid Science*, 51:56–70, 2013.

[83] J. Van-Jaarsveld, A. Holten, A. Elsenaar, R. Trieling, and G. Van-Heijst. An experimental study of the effect of external turbulence on the decay of a single vortex and a vortex pair. *Journal of Fluid Mechanics*, 670:214–239, 2011.

[84] H. Ghimire and SCC. Bailey. An experimental investigation of wing-tip vortex decay in turbulence. *Physics of Fluids*, 29(3):037108, 2017.

[85] H. Ghimire and SCC. Bailey. Experimental examination of vorticity stripping from a wing-tip vortex in free-stream turbulence. *Physical Review Fluids*, 3(3):034702, 2018.

[86] M Mula, S. *Stability and turbulence characteristics of a spiraling vortex filament using proper orthogonal decomposition*. PhD disretation, The University of Texas at Austin, 2015.

[87] M. Mohamed and J.C. Larue. The decay power law in grid-generated turbulence. *Journal of Fluid Mechanics*, 219:195–214, 1990.

[88] G. Comte-Bellot and S. Corrsin. Simple eulerian time correlation of full-and narrow-band velocity signals in grid-generated,'isotropic'turbulence. *Journal of Fluid Mechanics*, 48(2):273–337, 1971.

[89] H. Tennekes and J.L. Lumley. *A first course in turbulence.* MIT press ISBN9780262200196, 1972.

[90] K.R. Sreenivasan, S. Tavoularis, R. Henry, and S. Corrsin. Temperature fluctuations and scales in grid-generated turbulence. *Journal of Fluid Mechanics*, 100(3):597–621, 1980.

[91] Giulio Vita, Hassan Hemida, Thomas Andrianne, and Charalampos C Baniotopoulos. Generating atmospheric turbulence using passive grids in an expansion test section of a wind tunnel. *Journal of Wind Engineering and Industrial Aerodynamics*, 178:91–104, 2018.

[92] SCC. Bailey, T. Tavoularis, and B. Lee. Effects of freestream turbulence on wing-tip vortex formation and near field. *Journal of aircraft*, 43(5):1282–1291, 2006.

[93] R. Cucitore, M. Quadrio, and A. Baron. On the effectiveness and limitations of local criteria for the identification of a vortex. *European Journal of Mechanics/B Fluids*, 18(2):261–282, 1999.

[94] S. Beresh, J.F. Henfling, and R.W. Spillers. Meander of a fin trailing vortex and the origin of its turbulence. *Experiments in fluids*, 49(3):599–611, 2010.

[95] M.L. Beninati and J.S. Marshall. An experimental study of the effect of free-stream turbulence on a trailing vortex. *Experiments in Fluids*, 38(2):244–257, 2005.

[96] S. Beresh, J.F. Henfling, and R.W. Spillers. Turbulence of a fin trailing vortex in subsonic compressible flow. *AIAA journal*, 50(11):2609–2622, 2012.

[97] P.R. Bandyopadhyay, R.L. Ash, and D.J. Stead. The organized nature of a turbulent trailing vortex. *AIAA Paper*, 10:1627–1633, 1991.

[98] A.J. Cotel and R.E. Breidenthal. Turbulence inside a vortex. *Physics of Fluids*, 11(10):3026–3029, 1999.

[99] L. Jacquin and C. Pantano. On the persistence of trailing vortices. *Journal of Fluid Mechanics*, 471:159–168, 2002.

[100] JMM Sousa and JCF Pereira. Rollup region of a turbulent trailing vortex issued from a blade with flow separation. *Experimental thermal and fluid science*, 20(3):150–161, 2000.

[101] C. Del-Pino, J.M. Lopez-Alonso, L. Parras, and R. Fernandez-Feria. Dynamics of the wing-tip vortex in the near field of a naca 0 012 airfoil. *The Aeronautical Journal*, 115(1166):229–239, 2011.

[102] A. Laneville. *Effects of turbulence on wind induced vibrations of bluff cylinders*. PhD Thesis - University of British Columbia, 1973.

[103] B.J. Vickery. Fluctuating lift and drag on a long cylinder of square cross-section in a smooth and in a turbulent stream. *Journal of Fluid Mechanics*, 25(3):481–494, 1966.

[104] W.D. Baines and E.G. Peterson. An investigation of flow through screens. *Trans. Am. Soc. Mech. Engrs.*, 73, 1951.

[105] P.W. Bearman and T. Morel. Effect of free stream turbulence on the flow around bluff bodies. *Progress in aerospace sciences*, 20(2-3):97–123, 1983.

[106] Y. Nakamura, Y. Ohya, and S. Ozono. The effects of turbulence on bluff-body mean flow. *Journal of Wind Engineering and Industrial Aerodynamics*, 28(1-3):251–259, 1988.

[107] P.E. Roach. The generation of nearly isotropic turbulence by means of grids. *International Journal of Heat and Fluid Flow*, 8(2):82–92, 1987.

[108] A Allaf-Akbari, A.G Holloway, L Gordon, and J Hall. The effect of longitudinal core flow on trailing vortex stability. In *ASME 2014 International Mechanical Engineering Congress and Exposition*. American Society of Mechanical Engineers Digital Collection, 2014.

[109] K. Rokhsaz and L.K. Kliment. Experimental investigation of corotating vortex filaments in a water tunnel. *Journal of aircraft*, 40(6):1115–1122, 2003.

[110] A.M. Edstrand, B. DavisT, P.J. Schmid, K. Taira, and Louis. Cattafesta. On the mechanism of trailing vortex wandering. *Journal of Fluid Mechanics*, 801, 2016.

[111] A. Hussain and W.C. Reynolds. The mechanics of an organized wave in turbulent shear flow. *Journal of Fluid Mechanics*, 41(2):241–258, 1970.

[112] G. Berkooz, P. Holmes, and J. Lumley. The proper orthogonal decomposition in the analysis of turbulent flows. *Annual review of fluid mechanics*, 25(1):539–575, 1993.

[113] L. Sirovich. Turbulence and the dynamics of coherent structures. i. coherent structures. *Quarterly of applied mathematics*, 45(3):561–571, 1987.

[114] J. Jeong and F. Hussain. On the identification of a vortex. *Journal of fluid mechanics*, 285:69–94, 1995.

[115] D.S. Bulathsinghala, R. Jackson, Z. Wang, and I. Gursul. Afterbody vortices of axisymmetric cylinders with a slanted base. *Experiments in Fluids*, 58(5):60, 2017.

[116] P.N. Shah, P. Atsavapranee, T. Hsu, T. Wei, and J. McHugh. Turbulent transport in the core of a trailing half-delta-wing vortex. *Journal of Fluid Mechanics*, 387:151–175, 1999.

[117] D. Fabre, D. Sipp, and L. Jacquin. Kelvin waves and the singular modes of the lamb–oseen vortex. *Journal of Fluid Mechanics*, 551:235–274, 2006.

[118] J.L. Balint, P. Vukoslavcevic, and J.M. Wallace. The transport of enstrophy in a turbulent boundary layer. *Near-Wall Turbulence*, pages 932–950, 1990.

[119] S.B. Pope. *Turbulent Flows, 771 pp.* Cambridge Univ. Press, Cambridge, UK, 2000.

[120] R.D. Mehta and P. Bradshaw. Design rules for small low speed wind tunnels. *The Aeronautical Journal*, 83(827):443–453, 1979.

[121] L. Cattafesta, C. Bahr, and J. Mathew. Fundamentals of wind-tunnel design. *Encyclopedia of Aerospace Engineering*, 2010.

[122] J. Barlow, W. Rae Jr, and A. Pope. Low speed wind tunnel testing. *INCAS Bulletin*, 7(1):133, 2015.

[123] W. Rae and A. Pope. *Low-speed wind tunnel testing.* Number BOOK. John Wiley, 1984.

[124] G.B. Schubauer and W.C. Spangenberg. Aerodynamic characteristics of damping screens.

[125] TFI. *TFI Cobra probe Catalogue.* 2000.

[126] S Discetti and R Adrian. High accuracy measurement of magnification for monocular piv. *Measurement Science and Technology*, 23(11):117001, 2012.

[127] D Birch and N Martin. Tracer particle momentum effects in vortex flows. *Journal of Fluid Mechanics*, 723:665–691, 2013.